INSIGHTS INTO THE HETEROGENEITY OF COAL FLY ASH WASTE

Brinthan Kanesalingam

228057N

Master of Science (Major Component Research)

Department of Earth Resources Engineering
Faculty of Engineering

University of Moratuwa
Sri Lanka

May 2024

INSIGHTS INTO THE HETEROGENEITY OF COAL FLY ASH WASTE

Brinthan Kanesalingam

228057N

Thesis submitted in partial fulfillment of the requirements for the degree
Master of Science (Major Component Research)

Department of Earth Resources Engineering
Faculty of Engineering

University of Moratuwa
Sri Lanka

May 2024

DECLARATION

I declare that this is my own work and this Thesis does not incorporate without acknowledgement any material previously submitted for a Degree or Diploma in any other University or Institute of higher learning and to the best of my knowledge and belief it does not contain any material previously published or written by another person except where the acknowledgement is made in the text. I retain the right to use this content in whole or part in future works (such as articles or books).

Signature: Date: 03 May 2024

The supervisors should certify the Thesis with the following declaration.

The above candidate has carried out research for the Master of Science (Major Component Research) Thesis under our supervision. We confirm that the declaration made above by the student is true and correct.

Name of Supervisor: Dr C. L. Jayawardena

Signature of the Supervisor: Date: 2024 - 05 - 03

Name of Supervisor: Dr Ashane Fernando

Signature of the Supervisor: Date: 2024.05.04

Name of Supervisor: Dr D. A. S. Amarasinghe

Signature of the Supervisor: Date: 2024.05.04

Name of Supervisor: Dr D. Attygalle

Signature of the Supervisor: Date: 2024.05.04

i

ACKNOWLEDGEMENT

ABSTRACT

Coal is a well-known workhorse for power generation, particularly in developing countries, due to its favourable economic benefits such as low cost, wide availability, and minimal infrastructure. However, coal-fired power plants yield a substantial by-product, known as coal fly ash (CFA), with a global annual output of 1 billion tons during combustion. Only 60% of this CFA is presently used, whereas the rest is disposed of in the environment, contributing to severe environmental pollution. In contrast, CFA is a versatile material that can serve as an adsorbent, fertiliser, and in advanced material applications, offering a promising dimension for its use. This study addressed the multifaceted potential of CFA components, by probing its seldom-explored heterogeneity through advanced characterisation techniques. While existing research has predominantly focused on isolated extractions, neglecting broader applications, this study proposes a comprehensive strategy centred on the strategic implementation of washing cycles. Integral to this approach is an extensive characterisation campaign employing multi-modal imaging techniques, such as scanning electron microscopy and energy-dispersive X-ray spectroscopy combined with state-of-the-art deep learning algorithms and digital image processing techniques. Through these methods, this study uncovered and extracted various valuable constituents from CFA, notably cenospheres and materials conducive to zeolite synthesis, demonstrating their potential as effective adsorption agents. Furthermore, this study pioneered a novel methodology that combined X-ray microanalysis with deep learning to precisely classify and characterise cenospheres. This breakthrough facilitated a comprehensive understanding of these hollow structures and allowed quantification of their imperceptible physical structures to modify them as efficient adsorbents. The results of this study significantly contribute to elucidating the capabilities of CFA as a source of high-performance adsorption agents. By leveraging innovative techniques and holistic approaches, this study advances our understanding of CFA, and offers a pioneering methodology for sustainable waste management and resource recovery.

Keywords: Coal fly ash, Cenosphere, X-ray microanalysis, Deep learning

TABLE OF CONTENTS

LIST OF FIGURES

LIST OF TABLES

LIST OF ABBREVIATIONS

Abbreviation	Description
BSE	back-scattered electron
CFA	coal fly ash
CPU	central processing unit
CT	computed tomography
DB	disperse blue
DIP	digital image processing
DO	disperse orange
EC	electrical conductivity
EDS	energy-dispersive X-ray spectroscopy
ENC	entering cell wall
EPMA	Electron probe X-ray microanalysis
EXC	exiting cell wall
GPU	graphics processing unit
IOU	intersection over union
LCA	life cycle assessment
MB	methylene blue
MC	Monte Carlo
MSE	mean squared error
PSD	particle size distribution
REEs	rare earth elements
RMSE	root mean square error
SAM	Segment Anything Model
SD	standard deviation
SE	secondary electron
SEM	Scanning Electron Microscope
SSRs	secondary solid residues
XRD	X-ray diffraction

CHAPTER 1

INTRODUCTION

1.1 Motivation

The accelerated phase of urbanisation and industrialisation demands high energy production, which is not adequately met by many renewable energy sources that are available, such as wind, solar, and geothermal energy. On the contrary, abundant coal reserves, existing compatible infrastructure, and direct usability with almost no transformation make coal an affordable power source, especially conducive to the economies of developing nations. In 2022, there was a 1.2% increment in coal demand compared to 2021, attributed mainly to the global energy crisis and the rise in fossil fuel prices (IEA, 2022). This increase propelled coal production to reach an all-time high in 2022. Global coal demand is expected to plateau at 8 billion tons per year, along with increasing utilisation in India (117 Mt), China (87 Mt), and other Asian countries (37 Mt). However, no downfall in coal demand is expected, considering the increase in nuclear power generation (e.g., infrastructure, consultancy, regulations, waste disposal and reutilisation routes, and research and development) and high gas prices. The International Energy Agency (IEA, 2022) forecasted an ambitious objective of fulfilling 90% of the future energy demand through the utilisation of renewable energy resources by the year 2025.

Coal combustion for electricity generation in thermal power plants accounts for 30% of the anthropogenic CO_2 (Kanniche et al., 2017). Global CO_2 emissions are at their peak and are projected to increase until 2100, with an alarming concentration of 940 ppm by the end of this century, significantly contributing to global warming (Smith and Myers, 2018; Hua et al., 2023; Zheng et al., 2022). Despite this, numerous studies (e.g., Skjervold et al. (2023); Cao et al. (2021); Martins et al. (2022)) have explored the reutilisation of CO_2 generated by thermal power plants, offering potential solutions for mitigating its impact. In addition to CO_2, the release of harmful pollutants such as SO_x and NO_x from thermal power plants contributes to acid rain. This phenomenon can have far-reaching consequences, including the exacerbation of global issues such as photochemical pollution and depletion of the ozone layer (Wang et al., 2021a). On the other hand, coal combustion generates coal fly ash (CFA) as a significant solid waste among others (e.g., bottom ash, boiler slag, fluidised bed combustion ash, and other solid fine particles), accounting for 65% to 90% of the total ash volume (Mushtaq et al., 2019; Asokan et al., 2005). The annual generation of CFA is over one billion metric tons, of which 40% is not utilised and openly stored in landfills and ponds

or disposed of by simple stacks (Valeev et al., 2019; Yao et al., 2015; Wang et al., 2021c).

Prolonged exposure to open storage of CFA poses environmental and health hazards due to its chemical properties, including high leachability, radioactivity, and toxicity, as well as physical properties, including low specific gravity (ranging from 2.1–3) and a wide range of particle sizes, ranging from a few nanometres to hundreds of micrometres (Wang et al., 2020; Ahmaruzzaman, 2010). In contrast to other byproducts originating from coal combustion, CFA has demonstrated the potential to cause high plasma malondialdehyde (a marker for oxidative stress in the human body) and DNA damage in exposed workers (Hagemeyer et al., 2019; Park et al., 2021). Moreover, the installation of air pollution control devices causes the majority of mercury (57.6 - 64.3%) to be discharged into CFA, making it one of the primary sources of mercury pollution in the environment (Kim et al., 2010; Chen et al., 2022c; Wang et al., 2020). Thus, it is essential to maintain proper CFA storage facilities and comprehensively use fresh and existing CFA produced by thermal power plants.

On the other hand, the growing population worldwide has led to the expansion of many industries and water consumption. Further, there is an increase in chemical usage in agriculture to meet the rising food demands. The amount of contaminants entering the water supply has increased dramatically in the last decade due to these factors (Khan et al., 2022). Consequently, the lack of access to clean water and proper sanitation has become a global threat regardless of whether the country is developing or developed. Several effective methods to treat wastewater have been introduced and applied on an industrial scale. Conventional methods of treating wastewater are ion exchange, chemical precipitation, membrane filtration, coagulation/flocculation, solvent extraction, biological methods, and adsorption. Among these, adsorption is favoured as a highly effective process with fast kinetics and flexible operation and design processes (Chai et al., 2021).

Heavy metal treatment can be considered an example of wastewater treatment through adsorption. Heavy metals (i.e., Cd, Zn, Pb, Fe, Cu, Hg, Ni, Mn, and Co), found naturally in trace amounts, are abundantly found in wastewater effluent (Chai et al., 2021). They are persistent pollutants with no bio-degradation, thus increasing bio-accumulation threats to the life of humans, animals, and plants (Visa, 2016). Besides heavy metals, pesticides, organic components, fluorides, nitrates, phosphates, dyes, and pathogens are found in wastewater from different sources (Singh et al., 2022b). Hence, a robust scientific method for treating used and contaminated water is essential to counterbalance excessive usage and pollution. The increasing demand for commercial adsorbents (i.e., activated carbon, polymeric resin, and zeolites) enables the development of economically viable alternatives, such as modified cenospheres and zeolites, from secondary resources. (Hong et al., 2017) suggests that using CFA

for zeolites is more beneficial than dumping and maintaining in ponds with appropriate environmental management systems. An interested reader is directed towards other sources, e.g., (Mushtaq et al., 2019; Wang et al., 2021b; Yao et al., 2015) for a comprehensive review on utilising zeolites from CFA for wastewater treatment. Further, the utilisation of modified cenospheres derived from CFA demonstrates substantial promise as an adsorbent, primarily attributed to the presence of active surface components, including Al, Si, Mg, and Fe (Ye et al., 2019). Further, several studies, such as (Markandeya et al., 2017, 2021; Ye et al., 2019; Xu et al., 2011), have consistently demonstrated the potential of cenosphere modification and their effective use as adsorbents in various wastewater treatment applications.

1.2 Significance of the study

The existing understanding of CFA heterogeneity is insufficient, primarily focusing on single-component and first generation applications such as construction industry. This narrow perspective leads to a lack of insights for optimising them for advanced applications, such as wastewater treatment, adsorption agent, and time-dependent drug delivery. Moreover, existing studies on CFA often neglect advanced characterisation techniques and image processing methods to understand its heterogeneity. This critical aspect remains unexplored, promoting this study to bridge the research gap and focus on this over-sighted facet of CFA.

Therefore, this research undertakes an in-depth analysis of the characteristics, capabilities, and possible enhancements of CFA derivatives, aiming to reveal the heterogeneity within CFA. Consequently, this study aims to fill this niche research gap by employing advanced techniques (imaging and image processing) to characterise CFA and quantifying the properties of its derivatives through non-invasive methods, such as electron microscopy and diffraction. This approach holds the potential to provide valuable insights into the modification of CFA components for advanced applications.

1.3 Aim & objectives

1.3.1 Aim

To comprehensively analyse the heterogeneity within CFA and its derivatives, utilising advanced imaging and image processing techniques.

1.3.2 Objectives

1. Investigating the efficiency of washing cycles as a pre-processing technique for segregating the components of CFA based on physical and chemical properties.

2. Utilising scanning electron microscopy, electron dispersive X-ray spectroscopy, and X-ray diffraction techniques to characterise the segregated components of CFA and applying advanced image processing and deep learning techniques to enhance the analysis of CFA components and their properties.

3. Developing computational models to simulate the behaviour of CFA derivatives, providing insights beyond the limitations of experimental characterisation techniques.

1.4   Research contributions

This study advances our comprehension of CFA and its derivatives, previously recognised as complex materials to characterise. Additionally, it investigates various characterisation techniques to analyse the properties of these derivatives, leading to a broader understanding of their complexity. By generalising methodologies and properties, this study contributes to a deeper comprehension of their intricate nature. Consequently, these insights facilitate the modification and enhancement of CFA derivatives for novel applications, including but not limited to time-dependent fertilisers, drug delivery agents, and adsorption materials. The research contributions are as follows:

1.4.1   Published journal article

1. Kanesalingam B., Fernando W.A.M., Panda S., Jayawardena C., Attygalle D., Amarasinghe D.A.S., (2023). "Harnessing the Capabilities of Microorganisms for the Valorisation of Coal Fly Ash Waste through Biometallurgy". *Minerals*, 13(6), 724.

1.4.2   Manuscripts

1. Kanesalingam B., Fernando W.A.M., Panda S., Jayawardena C., Attygalle D., Amarasinghe D.A.S., "Strategic routes in valorising coal fly ash waste to promote circular economy" (in preparation).

2. Kanesalingam B., Fernando W.A.M., Jayawardena C., Attygalle D., Amarasinghe D.A.S., Panda S., Rabbani, A., "Leveraging advanced characterisation of the derivatives of pre-processed coal fly ash using deep learning and digital image processing techniques" (in preparation).

3. Kanesalingam B., Fernando W.A.M., Jayawardena C., Attygalle D., Amarasinghe D.A.S., Panda S., Rabbani, A.,"Shedding electrons on cenospheres: Advancing characterisation through X-ray micro-analysis" *ChemistrySelect* (under review, submitted on January 30, 2024).

1.4.3 Magazine articles

1. "Coal, Calm, and Collected", *Materials World*, Institute of Materials, Minerals & Mining (IOM3), United Kingdom.

2. "Are we going to let coal fly ash to just fly? Transforming pollution into innovation", *Bolgoda Plains*, University of Moratuwa *(in preparation)*

1.4.4 Python package

1. **pyDeepP2SA**- Advanced particle characterisation package developed using deep learning, digital image processing, and numerical computing.

1.5 Thesis outline

The overarching theme of this thesis is the characterisation of CFA, with a primary emphasis on different components derived after applying a pre-processing strategy (i.e., washing cycles), through advanced characterisation and simulation methodologies. Electron and X-ray imaging served as the primary tools for capturing morphological details and imperceptible structures of these derivatives. Further, state-of-the-art deep learning techniques and image processing were employed to thoroughly evaluate them. The structure of the thesis is organised in a systematic manner to first assess the potential of proposed washing cycles and then individually assess the derivatives and their characterisation for broader applications.

Chapter 1: Introduction

Chapter 1 introduces the research's motivation, providing a comprehensive overview of CFA, the significance of wastewater treatment, and the utilisation of zeolites and cenospheres as adsorption agents.

Chapter 2: Literature review

Chapter 2 delves into an extensive exploration of existing literature related to CFA. The focus spans across its origin, composition, management strategies, applications, and its multi-component utilisation, notably encompassing zeolites and cenospheres.

Chapter 3: Methodology

Chapter 3 offers a detailed description of the research methodology. It primarily focuses on characterising raw CFA, the process of washing cycles, and the separation and multi-modal characterisation of components (i.e., floating layer, solution, and bottom layer) resulting from the washing cycles.

Chapter 4: Washing cycles as a pre-processing technique

Chapter 4 extensively explores the washing cycle technique with a strong discussion of its process and the recovered components from the process.

Chapter 5: Characterisation of the recovered components

Chapter 5 begins with the characterisation of the floating layer using advanced techniques and supplements this with digital image processing (DIP) and machine learning. Additionally, Chapter 5 provides detailed insights into X-ray microanalysis of particles from the floating layer, elucidating the intricate properties of cenospheres for potential uses. The chapter further explores the synthesis and characterisation of zeolites post-washing cycles and presents their utility as adsorption agents. It also assesses alternative applications of CFA, such as element extraction and the recovery of fertiliser components.

Chapter 6: Simulation, modelling, and automation

Chapter 6 extensively covers the simulation intricacies and the utilisation of X-ray microanalysis within this study. Additionally, it explores into the newly developed *pyDeepP2SA* Python package, elucidating its versatility, performance, and limitations in various characterisation endeavours.

Chapter 7: Conclusion and recommendations

Chapter 7 offers concluding remarks, effectively summarising the key findings of the thesis. It also includes recommendations for future research endeavours.

CHAPTER 2

LITERATURE REVIEW

2.1 Introduction to coal fly ash

2.1.1 Coal fly ash and its reusability potential

Coal is an attractive energy source, particularly for developing countries, due to its undeniable economic benefits, such as relatively low maintenance and abundant coal reserves to reinforce the supply chain (Rasheed et al., 2021). The dominance of coal for power production is now gradually shifting to Asia, which was previously occupied by the European Union (EU) and the United States of America (USA) (Wilson and Staffell, 2018). Although coal consumption in the EU and the USA is declining due to the Sustainable Development Goals by United Nations and the Paris Agreement in 2015, developing countries show tendency towards more economic means of generating electricity, resulting in a staggering 8033 Mt consumption of coal by 2023 (IEA, 2022). Over 60 countries are actively planning, permitting, and commissioning coal power plants and the majority of them are developing countries. Nearly 600 GW of added capacity is scheduled to be implemented by 2030 globally, whereas 223 GW is already under construction and 377 GW is in the early development stage (Cui et al., 2019). The electricity demand is expected to grow with the increase in population where implementation of new and upgraded coal infrastructures may be unavoidable.

The amount of by-product from coal-fired power plants is considerably high and expected to increase further as power plants continue to operate across the globe (Marinina et al., 2021; Petrus et al., 2022). Production of waste from power plants influence the society and the environment associated to coal infrastructures. Additionally, the by-products of coal combustion from power plants cause severe threats and unrecoverable pollution. Among these by-products, fly ash dominates 90% of the total ash volume. The annual generation of CFA is over one billion metric tonnes and become the world's largest solid waste pollutant (Yuan et al., 2021). It is expected to have an economic value of 4.5 billion USD in 2024 compared to 3.8 billion USD in 2018, with a growth rate of 6% (Sultana et al., 2021).

CFA has been utilised in several industries due to its versatility of mineral components and economic profitability. Presently, CFA is widely used in the construction industry as an additive to Ordinary Portland Cement (Teixeira et al., 2019; Kula et al., 2002). Also, these are being used as geo-polymers, Fenton-like catalysts, organic adsorbents,

CO$_2$ sequestration, cenospheres, and alternative sources of rare earth elements (REEs) (Petrus et al., 2022; Deng et al., 2022). In addition, there is ongoing extensive research being conducted to explore the potential of CO$_2$ sequestration via the CFA (Rahmah et al., 2022; Mazzella et al., 2016). However, approximately 40% of CFA worldwide is not utilised and eventually piled up in dumps requiring constant monitoring of their surrounding land, water, and crops (Yao et al., 2015). Current monitoring strategies involve various methods: piezometer monitoring observes water levels and pore water pressure in ash ponds, settlement monitors track the displacement of dyke walls in all directions, aerial surveys monitor water accumulation and freeboard in ash ponds, Finite Element Analysis assesses the phreatic line and Factor of Safety (FoS), and dam break analysis identifies potential failure zones while creating inundation maps (Mohanty et al., 2021).

2.1.2 Origins and composition of coal fly ash

CFA is a fine powder collected in electrostatic precipitators to prevent it from spreading through smokestacks. CFA comprises approximately 316 individual minerals and 188 mineral groups (Vassilev and Vassileva, 2007). Among them SiO$_2$, Al$_2$O$_3$, Fe$_2$O$_3$, CaO, K$_2$O, TiO$_2$, MgO, Na$_2$O, P$_2$O$_5$, and SO$_3$ occupy the majority (Nagao et al., 2023). Figure 2.1 illustrates a Scanning Electron Microscope (SEM) image of components of a CFA sample. These various components stem predominantly from coal geology and the combustion process within thermal power plants. Organic materials could have been amassed within coal-forming swamps through alluvial processes or might have originated from marine sediments. Additionally, minerals might have originated from the flora present in those swamps. Some minerals could have formed due to post-depositional influences, such as groundwater or compaction effects altering the coal deposits. While carbon and certain other elements within coal can be entirely oxidised or vaporised during combustion, a significant portion of the mineral content in parent coal transfers into CFA in different forms (Roy et al., 1981). CFA is generally mixed with water and transported to the ash dump. Dumping the CFA is hazardous due to its inherent leachability, radioactivity, and toxicity characteristics (Wang et al., 2020). It could ultimately result in the lands being withdrawn from productive use. When ash ponds left open without lack soil or vegetation cover, they dry up and release fugitive dust. This dust contaminates the nearby air, raising the overall concentration of particulate matter (Ghosh and Kumar, 2020). Particles from CFA (typically in the range of 0.5 to 100 μm) can reach the pulmonic lungs, penetrate the alveolar wall, and finally dissolve into plasma. Therefore, the exposure of humans to dry CFA disposal is a serious concern to health (Nihalani et al., 2020; Mishra et al., 2023). The substantial water demand for maintaining a CFA slurry negatively impacts both the economy and

the efficient use of natural resources. Additionally, various salts and metals in the CFA slurry percolate into the groundwater/soil and pollute it when maintaining CFA slurry. This contamination deteriorates the nearby ecosystem and contributes to the massive pollution of long-term usable underground water storage (Curpen et al., 2022). Thus, installing liner systems is mandatory for water quality monitoring (Vilakazi et al., 2022).
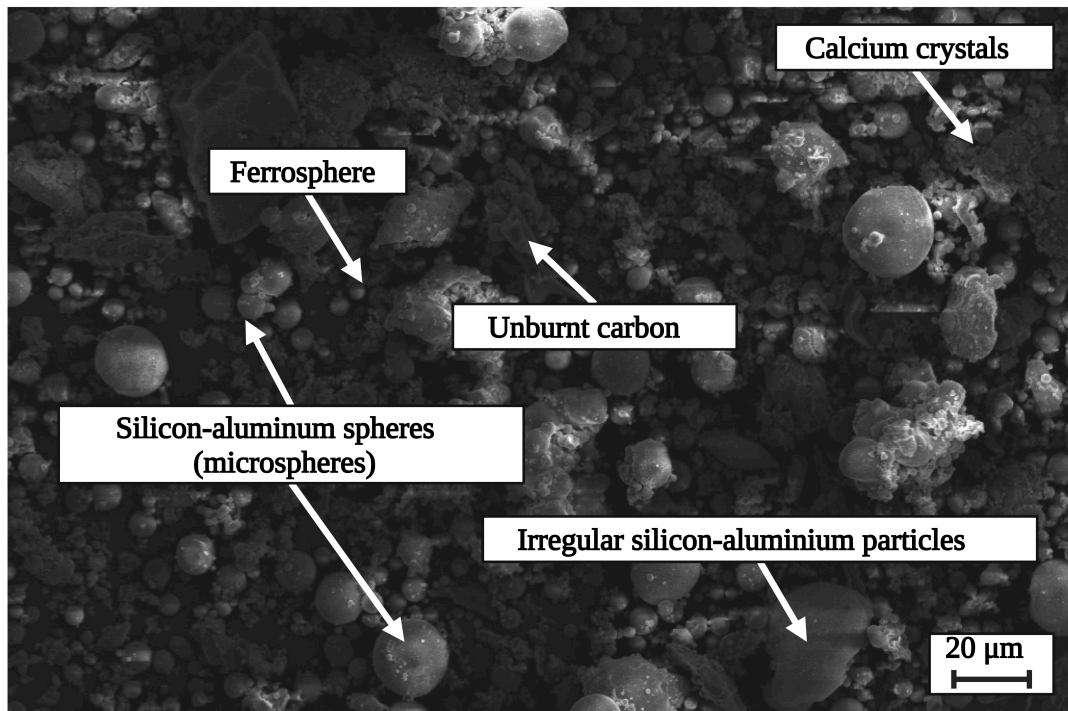
Figure 2.1: *Scanning electron microscopic image showing different components present in the raw coal fly ash sample (at 1000 X magnification and 10 keV)*

2.1.3 Coal fly ash management

The effort to promote efficient waste management is gaining momentum with the transition away from traditional economic approaches. The latest research from (Schöggl et al., 2020) reveals that waste management and recycling have been the second most prevalent topics discussed between 2000-2019 inside the circular economy theme. Circular economy is one of many economic principles that emphasise reducing, alternatively reusing, recycling, and recovering materials in the process cycle which includes production, distribution, and consumption (Kirchherr et al., 2017). In the context of CFA, it can be translated into creating a closed-loop economy by transforming waste products into revenue streams (i.e., waste to wealth) instead of sending them to landfills, thus maximising material utilisation (Geisendorf and Pietrulla, 2018; Romero-Hernández and Romero, 2018; Dos Santos et al., 2023).

9

The circular economy emphasises social, economic, and environmentally sustainable development, while life cycle assessment (LCA) focuses primarily on the environmental aspects (Pradhan, 2021). LCA of CFA predominantly focuses the environmental sustainability of its end products, such as zeolites, fertilisers, and advanced materials and their reusability. Hence, understanding LCA in conjunction with the circular economic aspects of CFA and its derivatives becomes crucial.

2.1.4 Coal fly ash applications

CFA is considered as a highly heterogeneous material which poses complexities in extracting its benefits. In recent years, various researchers performed extensive studies on the characterisation and up-cycling technologies of CFA which show promise in developing various value-added products (Xu and Shi, 2018). The low cost and high benefits of CFA make it a popular soil amelioration method (Babla et al., 2022; Zhou et al., 2020). Furthermore, CFA can buffer soil pH and provide many essential nutrients, except organic C and N. Additionally, CFA can improve the soil's physio-chemical properties and, as a result, its microbial activity increases. Moreover, the role of CFA as bricks, cement, and distemper in the ceramic industry is significant, as it replaces natural resources such as kaolinite, feldspar, and quartz (Zimmer and Bergmann, 2007; Zeng et al., 2020). Additionally, CFAs are used as catalysts, ameliorating agent for mine reclamation, adsorbent for wastewater treatment, and source of valuable metal recovery (Yao et al., 2015; Su et al., 2021). Presently, CFA is considered a raw material to produce carbon sorbents and serves as a hydrogen and carbon dioxide storage material (Czarna-Juszkiewicz et al., 2020; Ho et al., 2022).

The building and construction industry contributes significantly to recycling CFA as a resource or additive material in cement, concrete, bricks, and blocks (Qin et al., 2019; Menéndez et al., 2014). About 80% of produced CFA is consumed as cement or cement-based materials. Nonetheless, only a small fraction of those CFA which meet the specification requirements is converted into products, and the rest ends up in landfills (Du et al., 2022). On the other hand, synthesising geo-polymers and zeolites from CFA increases its usefulness. A comprehensive review on the geo-polymers synthesised from CFA is extensively reviewed by Li et al. (2022). Zeolites are cheap alternatives to commercially available activated carbon for wastewater treatment (Grela et al., 2021). However, the usage of CFA in the production of zeolites is in low quantities compared to the usage in building materials. Despite the utilisation of CFA in building materials, it is a promising value-added product that contributes to solving two fundamental problems: water quality and waste management (Visa and Chelaru, 2014).

2.1.5 Multi-component utilisation of coal fly ash

The full potential of CFA remains underestimated when only single component is utilised, leaving the rest of the wealth as ash dumps. This approach fails to provide an effective solution for addressing environmental concerns or cutting down maintenance costs (Yao et al., 2015). As a result, the multi-component utilisation of CFA has become a popular research topic because of its potential to provide economic and environmental benefits. Blissett and Rowson (2012) discussed the sequential separation of CFA using techniques such as heating, size classification, sink and float, magnetic separation, and flotation to extract value-added components. These techniques primarily focus on reducing the complexity of CFA by separating components with similar chemical and physical behaviours such as unburnt carbon, magnetic components, soluble cations, and microspheres. These extracted components can be utilised directly or through other techniques such as synthesis or sintering to produce value-added products, such as porous materials, fertilisers, and drug-delivery agents.

The major challenge in extracting and utilising multiple components from CFA stems from its heterogeneity. The presence of unburnt carbon in CFA detrimentally impacts the cation exchange capacity of zeolite by promoting condensed structures and reducing pore volumes (Wang et al., 2009). There are several strategies for pre-processing CFA, such as froth flotation, oil agglomeration, density separation, electrostatic separation, bioleaching, hydro-leaching, and magnetic separation, to separate unburnt carbon and remove soluble and magnetic components. However, these strategies pertain to single-component separation, and there is a lack of attention on preparing raw CFA for multi-component utilisation.

2.2 Washing cycles as a promising pre-processing technique

Water washing neutralises the basicity of CFA, promotes subsequent acid leaching, and enables the recovery of multiple value-added products. This approach ensures maximum utilisation of CFA while enhancing the synthesis of zeolites and recovery of cenospheres. Figure 2.2 illustrates a prospective washing cycle using deionised water.

2.2.1 Process of performing a washing cycles operation

Extracting maximum components from CFA while using minimal resources such as water, acid, alkaline, and heat energy is imperative in designing a sustainable pre-processing workflow for CFA. Addressing this, Pannilarathne et al. (2021) adopted a technical approach involving deionised water washing, monitoring ion dissolution in CFA through pH and conductivity assessment of the dissolved solution.

Figure 2.2: *Prospective washing cycle using deionised water.*

They noted a decrease in ion concentration of CFA after washing, yet the process lacked clear elucidation. Subsequently, Brinthan et al. (2022) conducted an in-depth exploration, employing surface response methodology to model and optimise the laboratory-scale process. Figure 2.2 illustrates the simple premise of "washing cycles". During this process, the mixture of raw CFA and deionised water was stirred using an external magnetic field. Then, the CFA solution was allowed to settle before the top layer is skimmed and transferred to a separate container. The solution was decanted into another container. After that, the bottom layer was rewashed with deionised water, and the process was repeated. The collected top, solution, and bottom layers are potential sources of value-added components after washing cycles. The washing cycle process is influenced by numerous dependent and independent parameters, outlined in Table 2.1. Brinthan et al. (2022) noted a nonlinear relationship among these factors, warranting further investigation through statistical modelling and machine learning techniques. This approach further enhances the suggested pre-processing model, and thereby, optimal parameters for the washing cycles can be derived.

Table 2.1: *Independent and dependent variables in a washing cycle process*

Independent variables	Dependant variables
Heating temperature	pH
CFA-to-water ratio	Conductivity of the solution
Stirring speed	Chemical composition of solution
Stirring time	Physical properties of bottom layer
Settling time	
Number of washing cycles	

2.2.2 Floating particles from the washing cycles operation

Figure 2.3 shows floating particles accumulate during the settling period of washing cycle as islands attached to the beaker's wall. Interparticle forces, such as Van Der Waal forces, cause the accumulation and attachment of these sub-micron particles. By virtue of this behaviour, particles can be recovered with simple techniques such as pond skimming or electrostatic separation (Petrus et al., 2020). SEM images of samples of floating particles indicate the presence of spherical hollow spheres, generally called "cenospheres", along with Ca and Mg crystals. Further, the element distribution maps of those individual spheres verify the presence of Si and Al in abundance. These results further confirm the presence of the cenosphere. Due to the varying density of the cenosphere (i.e., 0.2 - 2.6 g/cm^3), the low-density cenospheres float on the top of the solution while the rest submerged in the water (Yoriya et al., 2019).

The employed washing cycle is reminiscent of the well-known separation technique of removing cenospheres from CFA, i.e., sink and float. Buoyancy is primarily responsible for this process. Further, continuous stirring would enhance the lateral separation of the cenosphere from the rest of the components and facilitate the convenient flotation of particles. In large ponds of CFA, pond skimming is used to wipe the floating cenospheres (Danish and Mosaberpanah, 2020). The concentration of cenospheres varies from 0.01 to 4.80 wt%, whereas the low-density cenospheres are distributed from 0.3 to 1.5 wt% of the CFA (Ranjbar and Kuenzel, 2017). Inverted reflux classifiers, centrifuge, and air classifiers can improve the recovery of dense cenospheres and are being used in the industry (Yoriya and Tepsri, 2021; Wrona et al., 2020). On the other hand, washing the CFA with differing dense solutions (i.e., greater than the density of deionised water such as alcohol or mixture with acetone) may also facilitate the recovery of dense cenospheres.

The separated and purified cenospheres from washing cycles can be used in multiple industrial applications. Cenosphere can be used in electromagnetic shielding, lightweight metal alloy, immobilisation of radionuclides, emulsion explosive sanitisers, functionally gradient materials, less water absorption, insulation and thermal resistance, workability and durability matrix, low dielectric constant
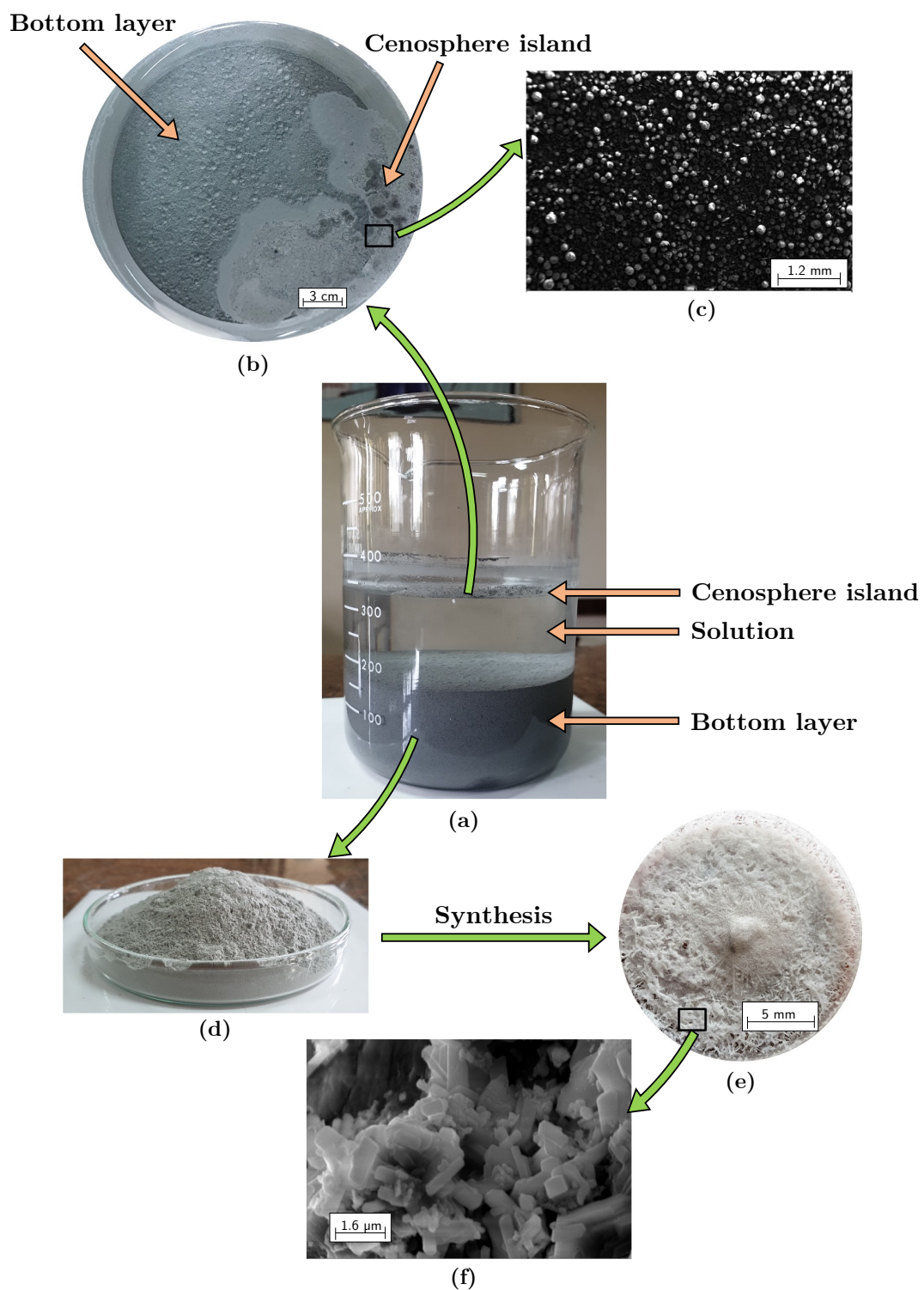
Figure 2.3: *(a) Different layers of CFA solution after the washing cycles. (b) Cenosphere island on the top (c) SEM image of floating particles (d) Ground oven-dried bottom sample (e) Synthesised zeolite (f) SEM image of zeolite-L.*

substrate, polymer and resin filter, lightweight ceramic, internal curing agent in cement concrete or inert mortar filler with good rheological properties, lightweight cement, and concrete, supper hydrophobic surface, transporting agent for drugs and photocatalysis. An interested reader is directed towards other comprehensive review of the usage of cenospheres such as Blissett and Rowson (2012),Ranjbar and Kuenzel (2017) and, Danish and Mosaberpanah (2020).

2.2.2.1 Cenospheres as an adsorption agent

Cenospheres, once separated from CFA, exhibit substantial potential as a promising surface adsorbent, owing to their active surface components like Al, Si, Mg, and Fe, as well as their unique surface properties and easily dispersible structure in solution, along with high water resistance (Ye et al., 2019; Xi et al., 2020; Brooks et al., 2020). However, these active components are in the form of mineral and glassy siliceous spherical particles. To uncover their full potential, surface modification of CFA is necessary (He et al., 2013; Song et al., 2017; Xu et al., 2011). Thus, modifying cenospheres after functionalisation is required to increase the availability of free surface binding sites and enhance porosity for effective removal of organic and inorganic pollutants from wastewater (Tiwari et al., 2015; Gadore and Ahmaruzzaman, 2021). The process of separating cenospheres may escalate costs and is generally less preferred (Yadav et al., 2021). Consequently, CFA and cenospheres are sometimes used together as adsorbents for air pollutants (Ge et al., 2018). Therefore, the washing cycle introduced recently offers an economical means of separating cenospheres from CFA.

On another note, cenospheres prove effective in the removal of disperse blue (DB) and disperse orange (DO) dyes through batch adsorption, achieving a 78% and 81% dye removal rate, respectively, from concentrated 40 g/L aqueous solutions (Tiwari et al., 2015). Further surface modification of cenospheres also shows promising outcomes. For example, cenospheres loaded with magnesia, produced through a wet impregnation process with $MgCl_2$, demonstrate promising potential (Xu et al., 2011). Cenospheres can also be applied in the solidification and removal of liquid and hazardous wastes, as well as in the production of porous crystalline molded glass (Anshits et al., 2005). When used in conjunction with other coagulants, cenospheres exhibit a promising effect on the removal of colours and dyes from wastewater. The degradation efficiencies of ferric chloride, ferrous sulphate, and alum, in combination with fly ash cenospheres, reach 57%, 20%, 63%, and 58%, respectively. However, the degradation limits of hybrid combinations, such as ferric chloride-cenosphere, ferrous sulphate-cenosphere, and alum-cenosphere, show significant improvements, eliminating toxins up to 73%, 60%, and 68%, respectively (Tiwari et al., 2015). Furthermore, mesoporous Al-MCM-41 produced using cenospheres adsorbs 277.78
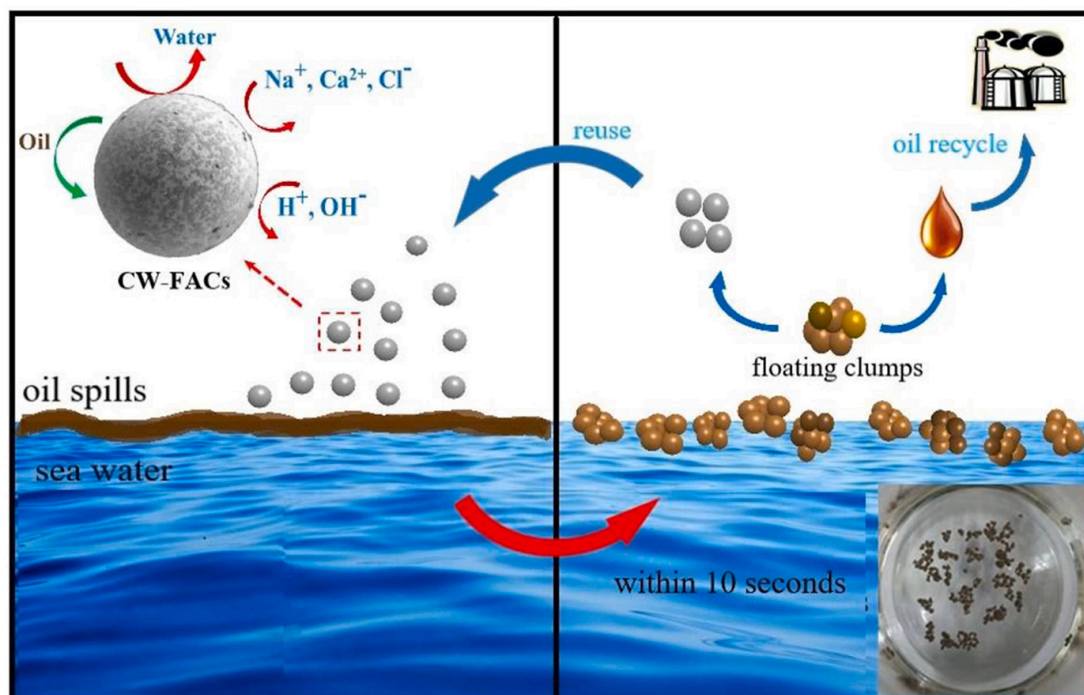
Figure 2.4: *Utility of hydrophobically-treated coal fly ash cenospheres (FACs) in combination with biodegradable candelilla wax (CW) to achieve a rapid oil adsorption rate and facilitate easy agglomeration (Sun et al., 2023).*

mg/g of methylene blue (MB) from aqueous solutions within 2 hours at pH 10 (Lu et al., 2013). Another study involving the adsorption of MB using different cenosphere-based nano-zeolite photocatalyst (Fe_2O_3-Na-X) demonstrates a remarkable 90.53% degradation efficiency for MB at pH 6.9 within 3 hours. Finally, an impressive 98% photocatalytic degradation of MB is achieved using a stable Ag-doped ZnO/CFA nanocomposite (Shende et al., 2021). In addition to these studies, various other literature, including (Song et al., 2017; Mushtaq et al., 2019; Vereshchagina et al., 2013b,a; Fomenko et al., 2016; Markandeya et al., 2021), strongly emphasise the potential and promising prospects of employing cenospheres as adsorbents in wastewater treatment.

2.2.3 Separated solution from the washing cycles operation

During washing cycles, the action of stirring and settling facilitates the extraction of readily soluble cations from the CFA through dissolution. Continuous stirring using the magnetic field enhances the particle interactions with the water molecules. Other methods of extracting the elements are sintering, ion exchange, electrolysis, and carbothermal reduction techniques (Ju et al., 2021). Comparing these methods, the dissolution process using water has numerous advantages, such as low-cost operation, high degree of universality, and simplicity of the process. On the other hand, there is a

limited selectivity of ions that can be easily leached by using water as the medium. This limitation in selectivity can result in the low extraction efficiency of elements.

Currently available solutions are rich in readily soluble elements such as Ca, Mg, Na, and K, which have significant potential for use in agriculture. The solution extraction from CFA rectifies most concerns addressed while applying raw CFA to agriculture. Problems such as radioactivity and heavy metal content of CFA are minimal in the CFA solution that remains after washing with deionised water. Further, macro-nutrients including P, K, Ca, Mg, and S and micro-nutrients such as Fe, Mn, Zn, Cu, Co, B, and Mo are present in the extracted solution. As a result, the characteristics of the extracted solution make it a crucial fertiliser precursor. Moreover, the same solution can be used as a pesticide to make plant composites (Basu et al., 2009). In addition, the high Ca in the solution replaces the Na in clay exchange sites to enhance the flocculation of soil clay particles. This replacement increases water penetration and allows roots to penetrate the soil (Jala and Goyal, 2006). Leaching of soluble components during washing with water are crucial in determining the effectiveness of using the extracted solution for agricultural applications.

Further, washing with alkaline is not recommended during the pre-processing phase due to the dissolution of Si and Al from the CFA. Subsequently, it decreases the amount of Si and Al that needs to be utilised during the synthesis of zeolites. On the other hand, acid leaching effectively eliminates impurities, except for Al and Si. Reducing the pH assists in liberating of trace elements that are locked within the core of the CFA (Eze et al., 2013). However, employing acid leaching as the primary pre-processing technique affects the recovery of cenospheres from the CFA. Salt residues formed due to interactions with acids may interfere with the separation of cenospheres. Therefore, acid leaching is recommended as a secondary treatment method for extracting elements, such as Fe, Ti, Ni, Co, Mn, Ga, Ge, and REEs (Pan et al., 2023; Jiang et al., 2022).

2.2.4 Oven dried bottom layer from the washing cycles operation

Residual bottom layers are the primary output after continuous washing cycles. Prolonged interaction with the water, further intensified by continuous stirring, would enhance the Si-Al composition in the bottom layer. Moreover, a decrease in particle size due to the dissolution of the surface rim indicates potential high particle interactions in further treatments (Meer and Nazir, 2018). The oven-dried bottom layer can be used directly in the synthesis of zeolites. Alternatively, secondary pre-processing (such as grinding, acid leaching, and sieving) on the bottom layer could enhance synthesis of zeolites. In addition, the leachate from the acid leaching

(i.e., secondary treatment) could extract critical elements such as REEs residing in the bottom layer (Gaustad et al., 2021; Chen et al., 2022a). The wet grinding of oven-dried bottom samples increases the Sauter mean diameter (i.e., surface-area-weighted mean diameter $D_{[3,2]}$) of particles, enhancing the synthesis of zeolites by exposing large surface areas to the alkaline solute (Yuan et al., 2021). The systematic approach to pre-processing could produce a simplified bottom layer (i.e., the precursor for the zeolite) that is at least reproducible for the taken CFA. Moreover, after the first synthesis, processing the residual with a concentrated alkaline solution extracts maximum Si and Al. Nevertheless, acid leaching of the bottom samples after washing is beneficial, since the extraction of elements, except Si and Al, allows for the better synthesis of zeolites. In most cases, it is not feasible to re-synthesise residual from the first synthesis since most Si, and Al components may already have been used. However, there are possibilities of producing zeolites with low CEC from the re-synthesis of bottom residuals (Teng et al., 2022). The residual from re-synthesis can be used as a soil stabiliser once tested for environmental compliance.

2.2.4.1 Zeolites from coal fly ash

Zeolites are three-dimensional tetrahedral aluminosilicate ((SiO_4)$^{4-}$ and (AlO_4)$^{5-}$ combination adjoined by oxygen atoms) crystalline minerals with a micro-porous infrastructure (Koshy and Singh, 2016; Szerement et al., 2021). These are generally represented in the following form of,

$$A_{y/m}^{m+}[(SiO_2)_x \cdot (AlO_2^{2-})_y] \cdot zH_2O$$
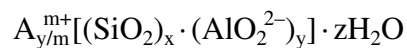
A $\rightarrow$ Cation with charge m
(x + y) $\rightarrow$ Number of tetrahedron per crystallographic unit cell
(x : y) $\rightarrow$ Si : Al ratio, where (x : y) < 1 (Lowensterin's rule)

The presence of silica (approximately 20 to 60%) and alumina (approximately 5 to 30%) in considerable quantities makes CFA a promising raw material for synthesising zeolites (Iqbal et al., 2019; Lin et al., 2023). Additionally, the high surface area of the CFA accelerates the synthesis of zeolites by exposing more surface area during the reaction (Ahmaruzzaman, 2010). CFA's low cost and bulk availability have driven more focus on utilising it as a precursor (Gao et al., 2022).

Properties of zeolites such as excellent ion-exchange capacity, high surface area, unique pore characteristics, catalytic properties, high degree of hydration and presence of zeolite water, and high chemical and thermal stability establish it as suitable materials for adsorption applications (Król, 2020). In addition, several studies have revealed that synthesised zeolites from CFA possess higher surface area, small crystalline sites, and high thermal stability compared to commercially available

zeolites (Iqbal et al., 2019). The void and internal channel infrastructure of zeolites allow uncomplicated access to molecules, leading to a fast diffusion rate. These unique characteristics of zeolites make them ideal adsorbents. The overall negative charge of the zeolite structure exhibits high cation exchange capacity; hence used as a molecular sieve (Blissett and Rowson, 2012).

The extensive uses of zeolites include gas purification, ion exchange in building materials, catalysis in oil refining, petrochemistry, adsorbent in the wastewater treatment, time-dependent fertlisers, and biotechnology (Amoni et al., 2022; Fan et al., 2023). Use of synthesised zeolites as adsorbents efficiently removes heavy metals and ionic species such as ammonium, chloride, fluoride, nitrate, phosphate, and sulphate from multiple polluted sources of industrial and domestic usage (Koshy and Singh, 2016).

2.2.4.2 Synthesis of zeolites

Table 2.2: *Zeolites and other neomorphic phases synthesised from CFA (Querol et al. (2002))*

Zeolitic product	Formula
NaP1 zeolite	$Na_6Al_6Si_{10}O_{32}.12H_2O$
Phillipsite	$K_2Al_2Si_3O_{10}.H_2O$
K-chabazite	$K_2Al_2SiO_6.H_2O$
Zeolite F linde	$KAlSiO_4.1.5H_2O$
Herschelite	$Na_{1.08}Al_2Si_{1.68}O_{7.44}.1.8H_2O$
Faujasite	$Na_2Al_2Si_{3.3}O_{8.8}.6.7H_2O$
Zeolite A	$NaAlSi_{1.1}O_{4.2}.2.25H_2O$
Zeolite X	$NaAlSi_{1.23}O_{4.46}.3.07H_2O$
Zeolite Y	$NaAlSi_{2.43}O_{6.86}.4.46H_2O$
Perlialite	$K_9NaCaAl_{12}Si_{24}O_{72}.15H_2O$
Analcime	$NaAlSi_2O_6.H_2O$
Hydroxy-sodalite (HS)	$Na_{1.08}Al_2Si_{1.68}O_{7.44}.1.8H_2O$
Hydroxy-cancrinite	$Na_{14}Al_{12}Si_{13}O_{51}.6H_2O$
Kalsilite	$KAlSiO_4$
Tobermorite	$Ca_5(OH)_2Si_6O_{16}.4H_2O$

Höller et al. (1974) pioneered modifying CFA into zeolites by applying the hydrothermal synthesis method. Since then, researchers have attempted to develop novel methods of synthesising zeolite that are both inexpensive and environmentally friendly. Well known zeolite synthesis techniques include alkali fusion-assisted hydrothermal treatment, microwave-assisted hydrothermal treatment, ultrasonication-assisted hydrothermal treatment, and the molten salt method (Koshy and Singh, 2016; Sivalingam and Sen, 2019). The synthetic zeolites resulting from different techniques exhibit promising results compared to natural zeolites. The

possibilities of altering the synthesis materials (such as Al, Si, and NaOH), doping with other elements (such as Ag), and the environmental factors (such as temperature, pressure, solid to liquid ratio, and seeders) allow to curate the zeolite synthesis for specific purposes (Tauanov et al., 2018; Joseph et al., 2020). Synthetic zeolites are more effective in adsorbing radioactive and heavy metals than natural zeolites due to the presence of large pores (Król, 2020). Moreover, synthetic zeolites have 3 to 5 times the adsorption capacity compared to natural zeolites and 6 to 7 times more than raw CFA (Itskos et al., 2010b; Yi et al., 2012). The various zeolite types achievable through CFA as precursors are tabulated in Table 2.2.

2.2.5 Circular economy of the washing cycles operation

The primary goal of the washing cycle was to produce a concentrated precursor for the synthesis of zeolites. Additionally, critical elements, fertiliser ions and cenospheres are noteworthy value-added products, which can be potentially recovered from the CFA derivatives. Critical elements, including Al, Mg, Ge, Ga, V, Se, REEs, Sc, and Nb (to name a few), show unprecedented demand for emerging technologies, such as solar photovoltaic, electric vehicles, and hydro-electrics. The scarcity of high-grade concentrated ore deposits prompts the requirement to seek secondary resources and one such opportunity is presented with the circular economy of CFA waste (Alberich et al., 2022). Furthermore, the fertiliser ions remaining in the leachate (or in the contaminated solution) are nutrients for plant growth (Ram and Masto, 2010). Direct application of leachate may depend on the composition of the parent coal, however, it should be noted that, if favourable, this approach may reduce the pressure on water and specialised fertiliser resources.

The bottom residues are zeolite-worthy and the synthesised zeolite materials could be useful in wastewater treatment applications. Upon adsorption of the contaminant ions on zeolites an additional conundrum rises, namely, the spent-zeolites disposal. Evidently, these are hazardous secondary solid residues (SSRs) , with the potential to be re-utilised by modifying the Si/Al ratio in the re-synthesis process. The addition of more wastes (e.g., mine tailings and steel slags) into such SSRs renders the surface chemistry to revert to almost a similar original condition, thereby promoting the re-usability of produced zeolites. Interestingly, Hidayat et al. (2021) demonstrated that the adsorption capacities of zeolites decrease only by 5 to 7% with each adsorption cycle.

Thus, creating avenues to promote a circular economy through CFA requires the consideration of value addition, resource utilisation, energy management and sustainability. Figure 2.5 illustrates an approach to promote circular economy in CFA with a focus on the washing cycles, and the post-processing and value addition.
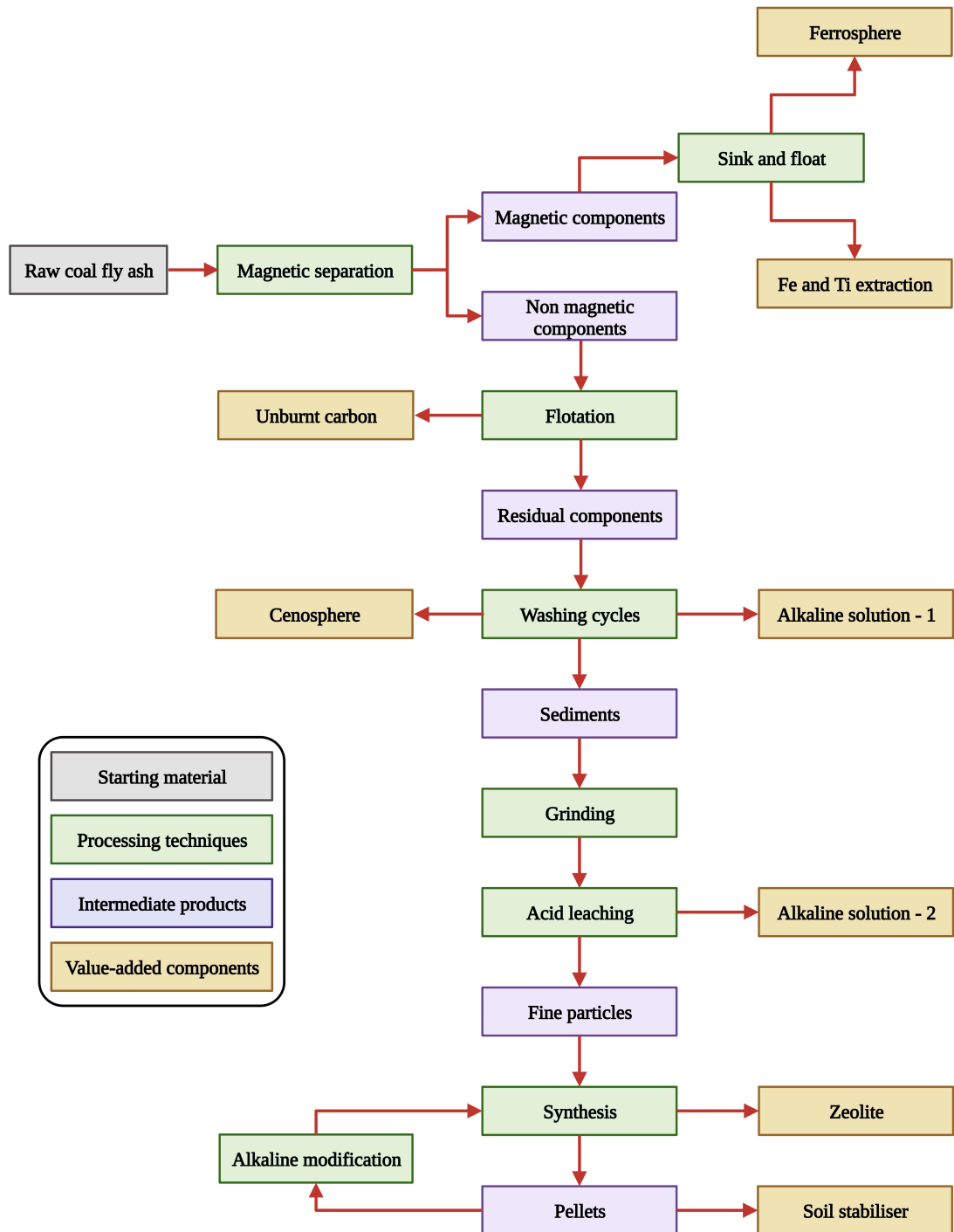
Figure 2.5: *A prospective flow sheet for valorising coal fly ash using the washing cycle as a primary pre-processing technique.*

CHAPTER 3

METHODOLOGY

3.1 Collection of raw CFA samples

The CFA samples used in this study were obtained from the Lakvijaya coal power plant in Norochcholai, Puttalam District, Sri Lanka. The parent coal of the collected CFA was bituminous and was imported from Indonesia (Gimhan et al., 2018). A SEM image of the collected CFA is shown in Figure 3.1 A, revealing a diverse range of particle sizes and shapes. Figure 3.1 B displays the X-ray diffraction (XRD) pattern of a gathered sample, primarily composed of quartz, mullite, magnetite, and calcite. Furthermore, energy-dispersive X-ray spectroscopy (EDS) was employed to determine the elemental composition of the samples (refer to Figure 3.1 C, D, and E).
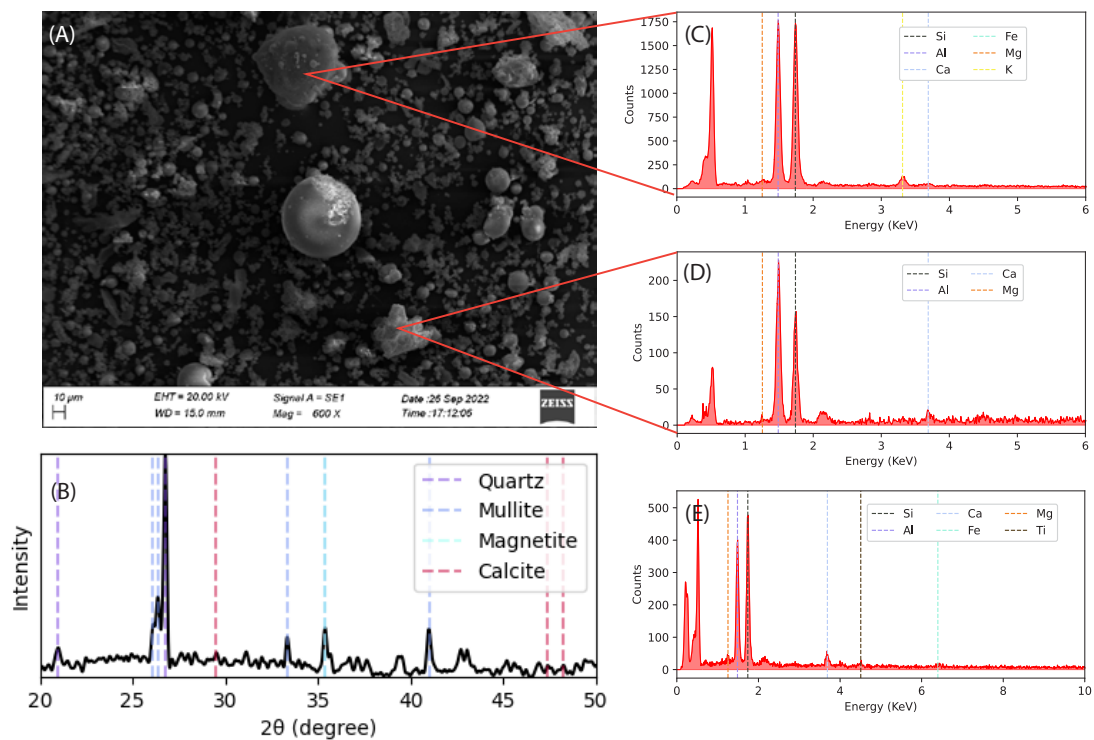
Figure 3.1: *(A) SEM-SE image of raw CFA (B) XRD of collected CFA (C - D) EDS of specific points on the CFA sample (E) EDS of scanned area of the CFA sample.*

3.2 Washing cycles

Washing cycles involve repetitively washing the raw CFA with deionised water to easily eliminate soluble ions adhering to the surface of the CFA particles. The deionised water used for washing the CFA was sourced from the AUTOSTILL^{TM} Freshman-4 system.

The collected raw CFA was washed with deionised water at different temperatures (29, 45, 65, and 90°C) while maintaining a constant solid-to-liquid ratio, stirring speed, and stirring and settling times. Initially, precisely measured 100 g of the raw CFA sample and 500 ml of deionised water were mixed in a transparent 1 L beaker. The same procedure was followed to prepare CFA solutions for experiments at 29, 45, 65, and 90°C, aimed at investigating the dissolution behaviour of CFA under different thermal conditions. The upper temperature limit was determined based on the boiling point of water, while the other experimental temperatures were chosen for the even distribution of assessment conditions.
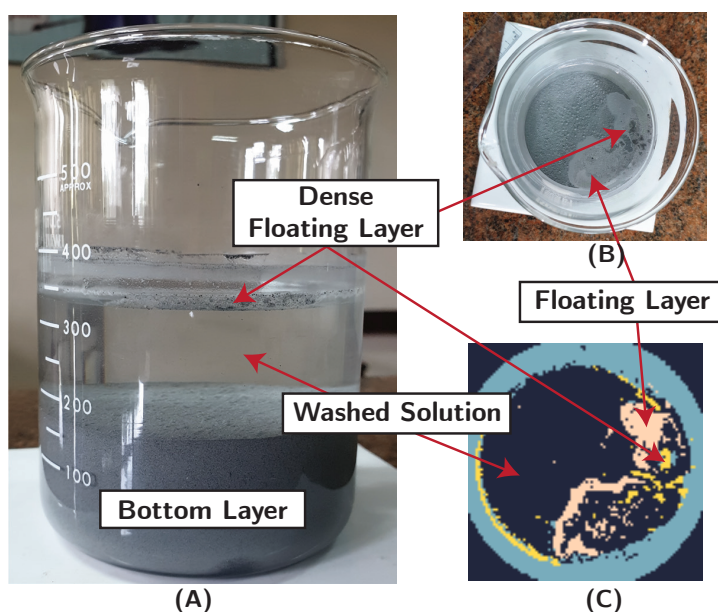
Figure 3.2: *(A) Side and (B) top views of the beaker with CFA after settling (C) Segmented top-view image of beaker following washing cycles.*

The beakers containing the CFA solutions were placed on a magnetic stirrer (AM4, VELP) equipped with an built-in heating mechanism. The solutions were stirred at 900 rpm for 15 minutes at 29°C and the solution temperature was continuously monitored using a mercury thermometer in case of sudden fluctuations. Subsequently, the stirred CFA solution was allowed to settle undisturbed for 15 minutes at the same temperature to maintain the provided thermal condition throughout the experiment. The appearance of a clear solution (compared to the cloudy solution immediately

23

after stop stirring) indicated the absence of particle movement toward the upper or lower portion of the beaker. During this settling period, the CFA solution was separated into three distinct layers, as illustrated in Figure 3.2 A. After settling, the top layer comprising the floating particles (refer to Figure 3.2 B) was carefully collected using a small Petri dish and stored in a sealed container. Figure 3.2 C depict the segmented top-view image of a settled beaker, featuring several distinct regions, characterised by a densely populated floating layer (yellow in colour), and another with a sparsely populated floating layer (peach in colour). The residual solution remaining in the beaker, hereafter referred to as the "washed solution", was transferred to a separate container, labelled, and kept out of direct sunlight. Finally, the bottom layer was collected and stored in an airtight container. This process of treating raw CFA with deionised water and segregating the different layers is referred to as the **"washing cycle"**, and the above-mentioned procedure refers to one washing cycle at 29°C. Figure 2.2 illustrates a schematic of the washing cycle at a constant temperature.

To ensure consistency in the solid-to-liquid ratio across multiple washing cycles, the layer obtained after removing the particles and solution from the first cycle was replenished with deionised water to the previous water level. As such, the desired ratio was carefully maintained, while the loss of particles from the floating layer remained negligible. The subsequent steps of the washing cycle were identical to the standard washing cycle process.

An experimental campaign consisting of 16 experiments was conducted to assess the performance of the washing cycles for removing readily soluble ions. This design of experiment is adapted from the Pannilarathne et al. (2021). The experiments encompassed four distinct numbers of washing cycles (1, 3, 5, and 7), conducted at four different temperature settings. Following each experiment, the separated components, floating particles, washed solution, and bottom layer were carefully stored in the container to facilitate subsequent analyses.

3.3 Characterisation and quantification of segregated layers

3.3.1 Floating particles from the washing cycles operation

The oven-dried (at 105°C for 24 hours) top layer samples were probed using SEM to obtain secondary electron (SE) and back-scattered electron (BSE) images. SE images are generated due to the release of SE resulting from inelastic collisions between the primary electron beam and the sample surface. In contrast, BSE images are produced by the backscattering of primary electrons after elastic interactions with the atomic structure of the sample. Therefore, SE offer a topographic view of the probed objects, while BSE images unveil details about their internal structure.

For a comprehensive analysis of the particle size distribution (PSD) within the collected floating particles, a ZEISS EVO 18 instrument was employed, allowing the acquisition of images at various magnifications and accelerating voltages. EDS was utilised for elemental mapping. To overcome the limitations of laser light-scattering techniques, a cutting-edge deep learning technique, i.e., Segment Anything Model (SAM) was employed to precisely determine the PSD of the floating particles (Calzolai et al., 2012). The currently employed method utilises a state-of-the-art instant segmentation model called SAM. DIP techniques, which are purely inferential, offer several advantages over traditional methods, such as sieve analysis and laser particle size analysis. These advantages include quick and less labour-intensive processes, independence from magnetic-field interference, and reduced intervention requirements (Shanthi et al., 2014; Meng et al., 2018).

Additionally, traditional laser particle size analysis introduces measurement errors for smaller particle sizes owing to the influence of hydraulic diameter. In contrast, DIP techniques provide accurate measurements for particles (depending on the technique and algorithm employed) and offer additional particle statistics, such as circularity, solidity, and minimum and maximum diameters (i.e., Feret diameter), which are not readily available via traditional methods.

When compared to currently available DIP techniques, deep learning-based models demonstrate tremendous potential because of their ability to learn complex image features and provide accurate segmentation (Ma and Wang, 2023). Among them, the zero-shot generalisation of SAM offers additional advantages, as it is already pre-trained on a dataset consisting of 1 billion masks from 11 million images (Kirillov et al., 2023). This pretrained model exhibits the potential to segment almost automatically and interactively with all inputs with varying accuracy. The application of SAM has gained considerable attention for general-purpose datasets (Ji et al., 2023) and medical images (He et al., 2023; Ma and Wang, 2023), highlighting its suitability for particle segmentation. By utilising a pretrained deep learning model, such as SAM, for instant particle segmentation, the time required for particle size analysis through DIP techniques is further reduced, along with improved accuracy.

3.3.1.1 Preparation for X-ray microanalysis

After the washing cycles, the floating layer was carefully skimmed and oven-dried for 24 h at 105°C. The oven-dried particles resulting from the floating layer were then sputtered with a thin Gold Palladium coating to prevent surface charging and to provide a homogeneous surface for analysis (Leslie and Mitchell, 2007). The Gold Palladium coated particles were analysed using a Zeiss EVO 18 scanning electron

microscope (SEM), which is capable of producing electron beams from 0.2 to 30 keV. The SEM was equipped with an Energy Dispersive X-ray Spectrometer (EDS) from EDAX, which includes a retractable "Octane" detector. EDS was used to measure the X-ray emission signals from the particles during the analysis.

3.3.1.2 Characterisation study

In this study, particles representing solid spheres and cenospheres were chosen based on visual interpretation of a 20 keV BSE image. Both solid spheres and cenospheres exhibit similar behaviour under SE conditions. However, cenospheres, characterised by a void surrounded by cell wall, display a contrast drop in the region associated with the void when probed for SEM-BSE images.

To investigate the influence of accelerating voltage on the characterisation of the selected cenospheres, line scans perpendicular to the detector were performed at three different accelerating voltages: 15, 20, and 25 keV, using the EDAX. The rationale for choosing these specific voltages lies on the limitation of the SEM used in this study. Throughout the characterisation process, a fixed step size of 100 nm and a working distance of 10 cm were maintained. The emission of Si Kα (1.740 keV) was selected as the proxy for this analysis since Si is the dominant component of the CFA spheres and is homogeneously distributed throughout the matrix. The distribution characteristics of Si in the spheres provide sufficient representation the study. Eight line scans of Si Kα emission were acquired and averaged to obtain a representative profile. In order to provide a comprehensive comparison, solid sphere was examined under the same conditions as the previous characterisation process to highlight any differences in Si Kα emission intensity. To gain further insights into the observed behaviour, geometric models representing the selected solid spheres and cenospheres were created and simulated under similar working conditions. This comprehensive approach facilitated a thorough analysis of the characteristics of the spherical CFA particles and their behaviour under different experimental conditions.

3.3.1.3 Simulations

Monte Carlo (MC) simulations provide a highly accurate description of the coupled transport of electrons and photons due to their ability to model arbitrary interaction processes and track particles in complex geometries. Moreover, their stochastic nature allows for straightforward evaluation of statistical uncertainties. However, MC simulations are also subject to simplifications and approximations in the materials and their distributions (Salvat and Llovet, 2018). To conduct preliminary and validation studies, well-established programs that have been cited in numerous scientific studies (e.g., (Kaboli et al., 2020; Peng et al., 2023; Kubota et al., 2018; Hoskins et al.,

2017)), such as CASINO V2.64, CASINO V3, and Monte Carlo X-ray simulation software (MC X-ray) (Drouin et al., 2007; Demers et al., 2011; Gauvin and Michaud, 2009) were utilised. These programs offer robust capabilities for accurate simulations, ensuring the reliability of results. In this study, the X-ray model employed comprises Bote (2009) for characteristic X-rays and the Kirkpatrick and Wiedman cross-section for bremsstrahlung radiation. Additionally, the energy loss is calculated using the modified Bethe equation (Joy and Luo, 1989).

3.3.2 Separated solution from the washing cycles operation

The pH and EC of the collected solutions were measured using a Hach SensION-1 pH meter and Hach HQ40D digital conductivity meter, respectively.

3.3.3 Bottom layer from the washing cycles operation

The collected bottom layers were oven-dried for 24 h at 120°C to remove any moisture. Direct exposure to heat or airflow circulation during the oven-drying process was restricted to the samples because their lightweight nature could lead to easy dispersion. Rigaku MiniFlex 600 and Bruker D8 advanced diffractometers were used to analyse the raw CFA, oven-dried floating, and bottom samples for mineralogical phases. Furthermore, the PSD of the bottom samples was measured using a wet method employing an ANALYSETTE 22 NanoTec Plus instrument (0.01 – 2000 μm range). The Sauter mean diameter was then calculated for the oven-dried bottom samples (Kowalczuk and Drzymala, 2016).

After five washing cycles at 65°C, the bottom sample was selected for the zeolite synthesis. A two-step alkaline fusion method was employed to synthesise laboratory-scale zeolites. NaOH served as a solvent to dissolve silica and alumina from raw CFA. Initially, 20 g of pre-processed CFA was added to a flask, and distilled water was poured to reach a volume of 100 ml. Subsequently, 5M NaOH was introduced into the solution, which was then thoroughly agitated until homogeneity was achieved. The resulting solution was heated and stirred simultaneously to enhance the interaction between NaOH and CFA, facilitating the removal of Si and Al. To separate the solid slurry from the clear extract, centrifugation was performed using a Z 206 A HERMLE compact centrifuge. The liquid solution was then oven-dried for 24 hours at 105°C. The recovered crystallised materials underwent SEM imaging and XRD analysis to confirm the successful synthesis of zeolites. Additionally, elemental mapping using EDS was conducted on the bottom layer.

CHAPTER 4

WASHING CYCLES AS A PRE-PROCESSING TECHNIQUE

4.1 Assessment of floating layer

A thin layer of particles accumulated at the top of the solution and attached to the wall of the beaker during the settling period of the washing cycles, as depicted in Figure 3.2 A and B. This behaviour can be attributed to inter-particle forces between the particles, particularly the van der Waals force, and the accumulation of particles near the walls enables convenient recovery using simple techniques such as pond skimming or electrostatic separation. Traditionally, this particle flotation phenomenon has been explained by the density differences between the deionised water used in the washing cycles and CFA particles. Examination of the SEM-SE images of the oven-dried particles from the floating layer revealed the presence of hollow spherical structures known as "cenospheres", identified by the presence of broken spherical particles (see Figure 5.7 A).

The cenospheres collected during the washing cycle are highly valuable materials derived from the CFA (Ranjbar and Kuenzel, 2017). They are primarily composed of oxides of both silicon and aluminium, forming aluminosilicate structures (Singh et al., 2022a). These floating cenospheres predominantly exhibit low density (less than $1\,\mathrm{g\,cm^{-3}}$) and are found to constitute a distribution ranging from 0.3 to 1.5 wt% of the CFA (Yoriya et al., 2019; Ranjbar and Kuenzel, 2017). In addition to the hollow spheres, the floating particles also contained solid spheres, unburnt carbon, and calcium crystals. Intriguingly, dense solid spheres, which were expected to sink, were attached to the cenospheres and ended up in the floating layer. The flotation of dense cenospheres and solid spheres can be explained by their particle size and porosity characteristics. In contrast, the presence of calcium crystals originates from the dissolution of the surface rim of the CFA particles, which subsequently crystallise during the oven-drying process. The XRD plot of the representative floating particles indicates the prevalence of calcite resulting from the dissolved calcium in the collected floating layer. Moreover, a series of complex reactions occurred during the stirring and settling periods of the washing cycles, influencing the growth of calcium carbonate on the surface of the cenospheres (Yoriya and Tepsri, 2021). This increase in calcium content leads to a decrease in viscosity, which is unfavourable for glass formation (Itskos et al., 2010a; Żyrkowski et al., 2016). Consequently, the presence of high calcium oxide hints at an environment that is not conducive to the creation of silica-alumina rich CFA, which is predominantly composed of silica and alumina. In

light of this, the presence of calcium crystals highlights the need for further processing of floating particles to obtain high-purity cenospheres. Controlling the attachment of calcium during combustion is a significant challenge. In contrast, calcium regrowth can be effectively regulated by conducting experiments in closed environments. This approach helps control the dissolution of CO_2 into the solution during the washing cycle (Yoriya and Tepsri, 2021). Additional processes, such as leaching with water or acids including HNO_3, are highly recommended to remove the attached calcium crystals from the cenosphere walls.

4.2 Assessment of washed solution

The deionised water used in the experiments exhibited an average pH of 6.89 ($\pm$0.12) and an electrical conductivity (EC) of 4.72 ($\pm$0.56) μS/cm, respectively. The EC of the solution measured the dissolution of cations from the CFA samples. Figure 4.1 illustrates the EC of the solution over multiple washing cycles (1, 3, 5, and 7) at different temperatures (29, 45, 65, and 90°C). The EC of the solution decreased with increasing number of washing cycles. Moreover, all investigated temperature ranges indicated similar phenomena. This trend demonstrates a reduction in readily soluble ions in CFA samples after each washing cycle. An identical phenomenon was observed by Ugurlu (2004) previously. The process of stirring and settling during washing cycles promotes the extraction of readily soluble cations, such as Ca, Na, and Mg, from CFA. Continuous stirring using a magnetic field enhances the particle interactions with water molecules. Most of the soluble components of CFA, such as, B, Ca, Cr, Mg and Sr, are concentrated on the CFA surface (i.e., the surface rim). These inorganic salts make CFA surfaces more reactive than glassy matrices (Zandi and Russell, 2007). During the washing cycles, the components on the surface of the CFA interacted with deionised water and dissolved, making the washed solution (i.e., leachate), a recovery sink for many ions. Apart from the CFA surface, these trace elements exist as fine dense particles.

The EC of the solution decreases with increasing temperature during the first washing cycle. This trend continued to appear during the subsequent washing cycles. This phenomenon was attributed to the dissolution behaviour of Ca cations in the CFA sample. Ca is the primary cation in leachate as it is the dominant soluble component in raw CFA (Kim et al., 2003). Therefore, the degree of dissolution of the Ca cations determines the EC and pH of the solution. As the temperature increased, a consequential shift occurred; the initially dissolved Ca cations tended to precipitate, forming calcium sulphate ($CaSO_4$) and calcium carbonate ($CaCO_3$). The precipitation of Ca cations leads to a marked reduction in Ca concentration within the solution (Ugurlu, 2004). The underlying principles of this precipitation phenomenon align
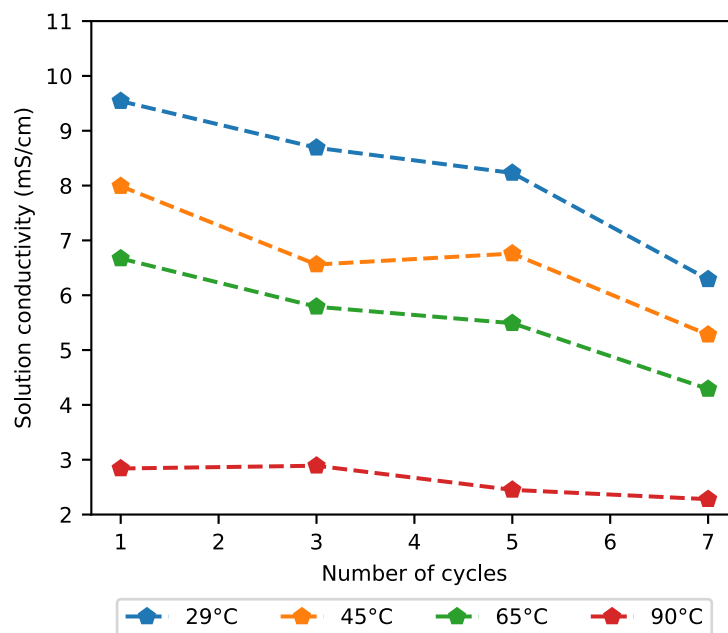
Figure 4.1: *Temperature dependency of solution conductivity with different washing cycles.*

with the concept of the solubility product constant (K_{sp}), wherein the relative solubility of calcium compounds at varying temperatures governs their tendency to precipitate out of solution. The K_{sp} values for $CaSO_4$ and $CaCO_3$ were relatively low, indicating that these compounds were less soluble and more likely to precipitate as the temperature increased.

The observed pH trends with increasing temperature and number of washing cycles further support the argument regarding the EC (refer to Figure 4.2). The pH of the solution decreased with an increasing number of washing cycles. This drop in pH indicates decreasing dissolution of readily soluble alkaline cations from the CFA sample. Furthermore, the decrease in pH with increasing temperature in each washing cycle indicated the precipitation of Ca cations from the solution. Na and K dissolution increased with increasing temperature, but their quantities were insignificant compared to those of the Ca cations. These observations suggest that Ca cations play a significant role in the behaviour and processing of CFA. Furthermore, the dissolution of Si forms weak silicic acid (H_4SiO_4) which also plays a role in determining solution pH (Iyer, 2002). Washing CFA with deionised water leached water-soluble elements in the order B > Mo > Se > Li > Sr > Cr > As $\sim$ Ba $\sim$ Cd $\sim$ V > Sn > Rb $\sim$ Zn > Cu $\sim$ Ni $\sim$ Pb > U > Co > Mn (Meer and Nazir, 2018). Additionally, the application of heat during the washing cycles enhanced the solubility of these elements. The introduction of thermal energy into the system aids the disruption of chemical bonds within the CFA matrix.
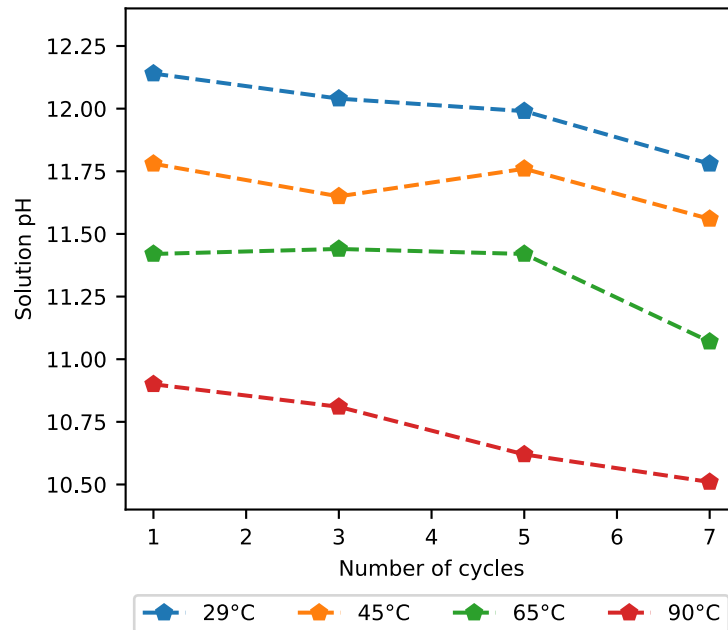
Figure 4.2: *Temperature dependency of solution pH with different washing cycles.*

4.3 Assessment of bottom layer
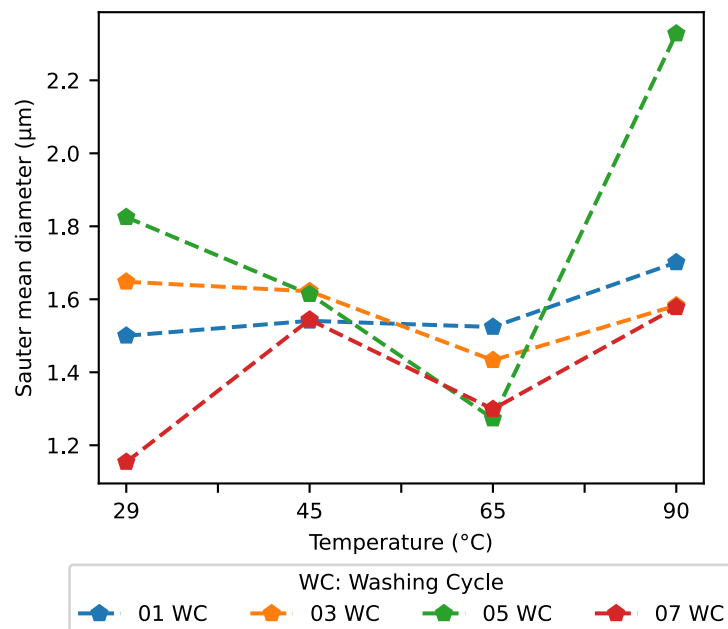
Figure 4.3: *Temperature dependency of Sauter mean diameter with different washing cycles.*

During the settling phase of the washing cycle, washed CFA gradually settled at the bottom of the beaker. Stirring was employed to facilitate the dissolution of readily

soluble ions from the surface rims of the CFA particles, resulting in a more homogeneous chemical composition for subsequent processing. Moreover, the dissolution of cations, such as Ca, Mg, Na, and K, from the particle surface enhances the interaction between Si and Al (residing within the core) along with reagents, such as sodium hydroxide (NaOH) (during the zeolite synthesis process), by exposing the CFA core to improve particle interactions (Meer and Nazir, 2018). Figure 4.3 illustrates the Sauter mean diameter of representative samples taken from the bottom layer throughout the experimental runs. The increasing trend observed in the Sauter mean diameter as the number of washing cycles increases, along with the fluctuation in this trend over seven washing cycles, possibly attributed to the pozzolanic properties of CFA particles resulting from prolonged exposure to moisture, i.e., the presence of H^+ and OH^- ions in deionised water (Lu et al., 2023). Furthermore, the PSD of the CFA samples remained constant after washing, with a marginal reduction in thickness (on the scale of a few micrometres). This dependable PSD uniformity plays a crucial role in generating CFA samples with similar PSDs, thereby greatly assisting in ensuring consistent and reliable research outcomes (Iyer, 2002). The primary elements found in CFA after washing cycles are Si and Al, with reduced impurities (Meer and Nazir, 2018).

CHAPTER 5

CHARACTERISATION OF RECOVERED COMPONENTS

5.1 Particle size distribution of floating particles
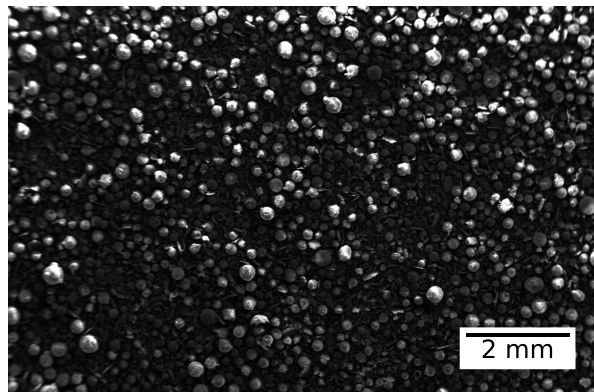
(A)
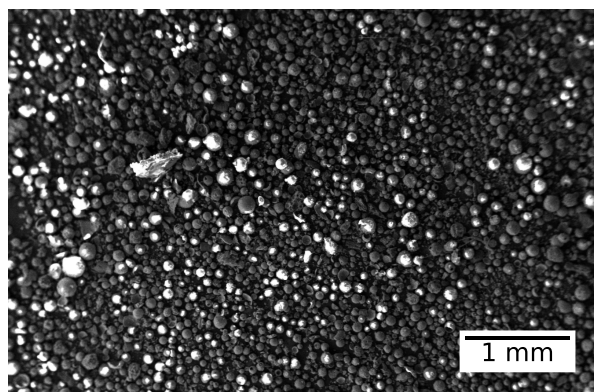
(B)
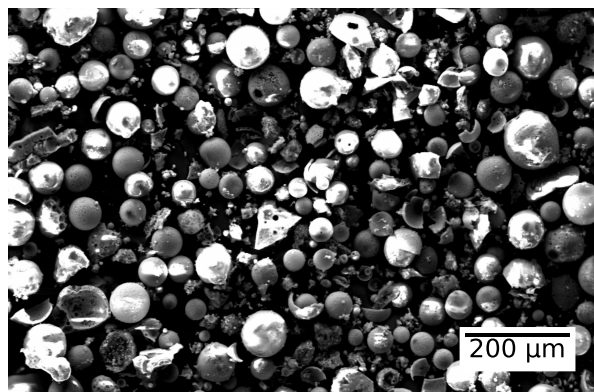
(C)

Figure 5.1: *SEM-SE images of floating layer at (A) 250x (B) 50x, and (C) 48x.*

Three different SEM-SE images taken at high (250x), medium (50x), and low (48x) magnification levels, as shown in Figure 5.1 A, B, and C, respectively, were used to assess the PSD of the recovered floating layer. Figure 5.2 B illustrates the particle segments created after employing SAM (Kirillov et al., 2023). The segments were sorted with a threshold of 0.8 for the circularity and the rest of the particles were considered for further analysis. Figure 5.2 A shows the PSD of the floating layer of segmented floating particles. All three distributions (i.e., high, medium, and low magnifications) corresponded to different particle size ranges in the floating layer. The high-magnification image shows a log-normal distribution of particles with a mean diameter of 100.69 μm and a standard deviation (SD) of 46.52 μm, whereas the medium- and low-magnification images follow a normal distribution with mean diameters of 488 and 246 μm, and SDs of 116.19 and 69.34 μm, respectively. The high-magnification image highlights the presence of smaller spherical particles in the floating layer, which were not captured in the medium- and low-magnification images. However, the low-magnification image captured the presence of larger spherical particles but failed to capture smaller particles below the 100 μm range. Comparing both images, the medium-magnification image captured a larger distribution of spherical particles, as shown in the box plots (Figure 5.2 C). However, each magnification level shows the distribution of the spherical particles in segments of different sizes. Therefore, the weighted average approach was employed to obtain the overall distribution of spherical particles. These weights were determined by considering the inverse of the squared SD (i.e., inverse of variance) of each distribution. The rationale behind this approach is that distributions characterised by smaller SD values are indicative of higher precision and thus warrant greater influence in the combined distribution. The weights were then normalised to maintain the proportion of each distribution. By multiplying each distribution by its corresponding normalised weight and summing them, obtained a representation of the combined particle size distribution. The mean diameter of this combined statistical distribution was 176.66 μm, accompanied by a SD of 36.35 μm. These statistics adhere to the particle size interval widely established in prior research, specifically within the range of 50–250 μm (Ranjbar and Kuenzel, 2017; Fomenko et al., 2013).

The problem with the image acquisition technique using SEM-SE is that it is surface sensitive (Zhu et al., 2009). This implies that the emitted SE originates from the atoms on the surface, resulting in an image contrast that is determined by the morphology of the sample (Saghiri et al., 2012). Consequently, this limitation hampers the differentiation between solid spheres and cenospheres, because both exhibit similar surface morphologies. The SEM-BSE imaging technique on the other hand overcomes this limitation by providing a higher depth of electron penetration (Zarraoa et al., 2019). This translates to a larger interaction volume within the
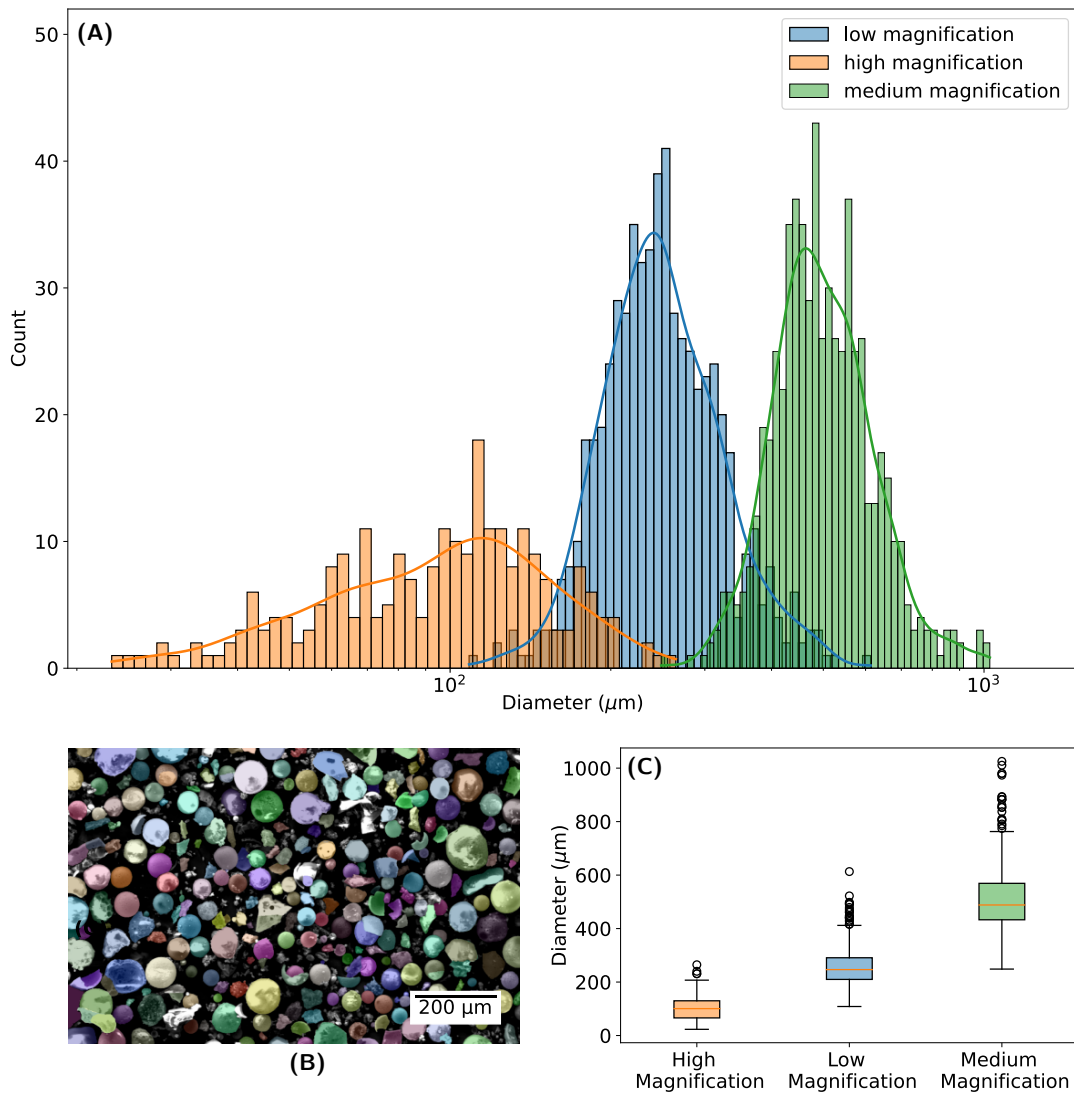
Figure 5.2: *(A) PSD obtained from images at different magnifications. (B) Output segments derived from the segment anything model. (C) Statistical distribution of particle sizes obtained from images at different magnifications.*

material. Compared to SEM-SE, SEM-BSE imaging allows for visualisation of the hollow interior of cenospheres through image contrast owing to the lack of electron generation at the penetration depths of void regions. Figure 5.1 C and Figure 5.3 B show the disparity between the SEM-SE and SEM-BSE images of the same segment of the floating layer. Notably, the SEM-BSE image demonstrates a clear distinction between solid spheres and cenospheres, which appear almost identical in a simple visual interpretation of SEM-SE images.
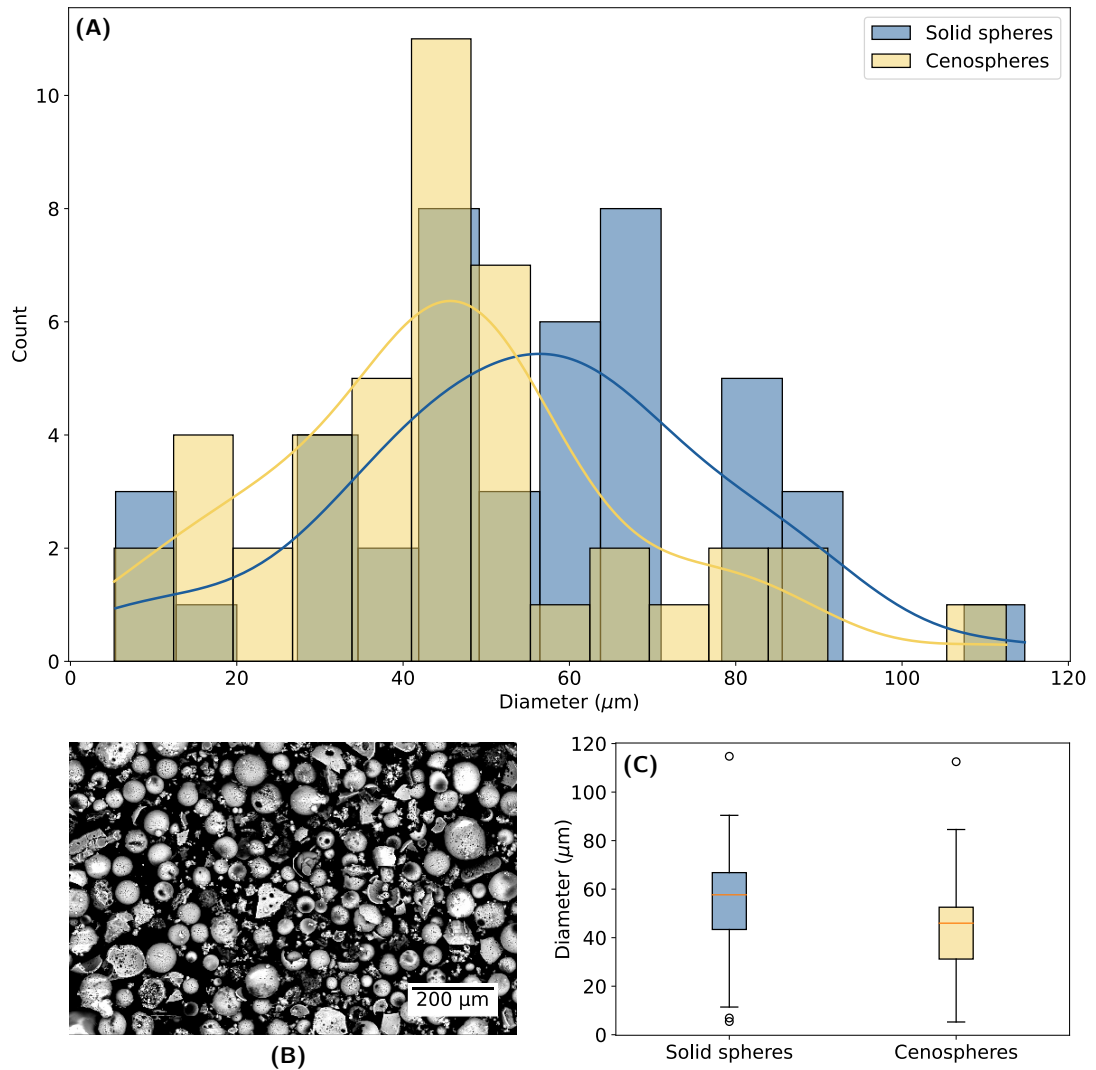
Figure 5.3: *(A) Comparison of PSDs between the cenospheres and solid spheres. (B) BSE image of the high magnification SEM-SE image, and (C) Distribution of particle sizes for both cenospheres and solid spheres.*

Figure 5.3 A illustrates the PSD of the selected solid spheres and cenospheres from a high-magnification image. Both the solid spheres and cenospheres exhibited nearly identical PSDs. The cenospheres had a mean diameter of 45.40 μm, with a SD of 21.98 μm, while the solid spheres had a diameter of 55.71 μm, with an SD of 23.10 μm. Figure 5.3 C illustrates the similarities between both distributions. This observation challenges the previously discussed findings on CFA particles and cenospheres, which suggest that cenospheres generally have larger diameters than CFA particles (i.e., solid spheres), as determined through the density separation technique (Yadav et al., 2021). However, the application of density separation technique encountered practical challenges, as there is a significant risk of identifying solid particles floated in the separation medium as cenospheres. In contrast, the

method employed in this study, i.e., using SEM-BSE images, is more reliable, as it accurately validates each sphere as solid or hollow. However, this method also has limitations and one such considerable limitation of SEM-BSE imaging is the limited depth of electron penetration, leading to potential misinterpretation of cenospheres as solid spheres, in case the BSE fails to penetrate the void region. Furthermore, the resolution of SEM-BSE images is lower than that of SEM-SE images, which may introduce errors when applying image-processing techniques to measure the particle sizes or circularity (Saghiri et al., 2012).

5.2   Assessment of cenosphere through SEM-BSE images

To evaluate the impact of the accelerating voltage (i.e., the incident beam energy) on the image acquisition, a selected cenosphere was exposed to incident beams at energies of 10, 15, 20, and 25 keV. Figure 5.4 A illustrates the images obtained at different incident beams, revealing a progressive increase in the contrast differences between the void and cell wall due to the increment in the number of electrons and thereby the increase in the contrast difference. Multiple thresholding techniques, such as Li, IsoData, Intermodes, Huang, Huang2, Yen, Triangle, Shanbhang, RenyiEntrophy, Percentile, Otsu, Moments, Minimum, MinError, Mean, and MaxExtropy, have been employed to differentiate pixels representing the void from the rest of the pixels (i.e., pixels associated with the cell wall) of SEM-BSE images (Sahoo et al., 1988). Figure 5.5 A-D present the distribution of the thresholding values obtained by multiple thresholding techniques for the images taken at different beam energies. Furthermore, the coefficient of determination values (compared to manually thresholded values) for the 16 thresholding techniques were calculated for all four BSE images. The variations in the thresholding values among the different methods underline the importance of a single thresholding method that offers higher accuracy in identifying voids. Among the tested techniques, the Otsu method showed a strong correlation with a high R-squared value of 0.986, indicating that its predictions closely matched the manually assessed threshold values (refer to Figure 5.5 F). Following Otsu, the IsoData method had a value of 0.980, whereas the moments, mean, and yen methods showed moderate correlations with the manually assessed threshold values. However, the MaxEntropy and MinError methods had negative values, indicating poor fit. The performance of a thresholding method can be influenced by the complexity and flexibility of the specific methods. More sophisticated methods, such as IsoData and Otsu, employ advanced techniques (such as identifying maximum inter-class variance and iterative thresholding) to adaptively determine the threshold based on the statistical properties of the image, thereby yielding a strong correlation with the manually assessed threshold values. On the other hand, the MaxEntropy method is less effective when there is a low contrast
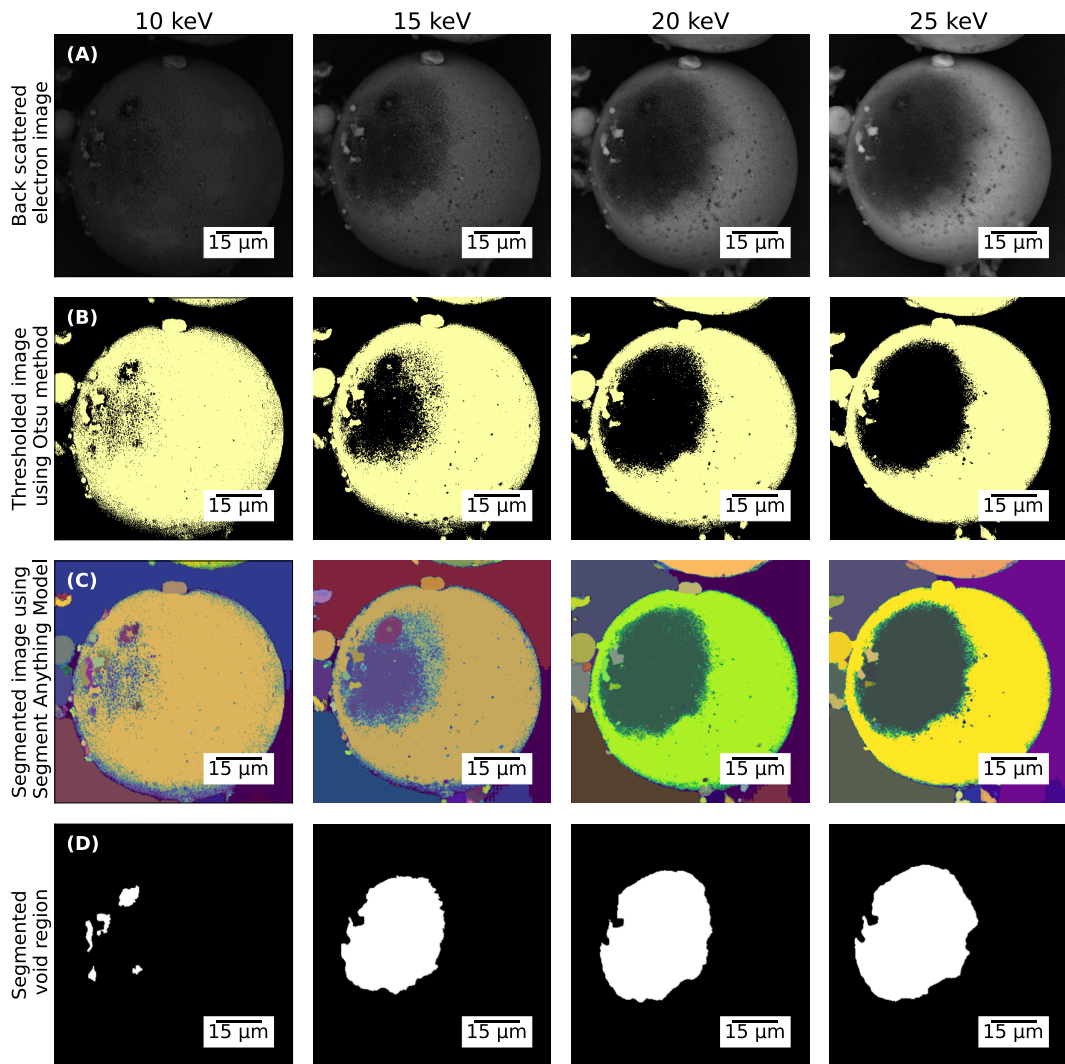
Figure 5.4: *(A) SEM-BSE images at various accelerating voltages. (B) Thresholded images obtained using Otsu's method. (C) Segmented images of thresholded images after applying segment anything model, (D) Isolated segments representing regions corresponding to voids.*

between the void and solid regions or when intricate textures are present. In light of this, thresholding methods such as Otsu, IsoData, moments, mean, and Yen can be suitable for differentiating voids from surrounding regions. In this study, Otsu's method was recommended, which closely predicts the manually assessed threshold values and is widely used in image processing, for example, (Liu et al., 2021; Ma and Yue, 2022). Figure 5.4 B illustrates the SEM-BSE images after applying Otsu's thresholding method.

Figure 5.4 C displays the segmented components from the thresholded images obtained using the previously utilised SAM and 5.4 D illustrates the isolated segments
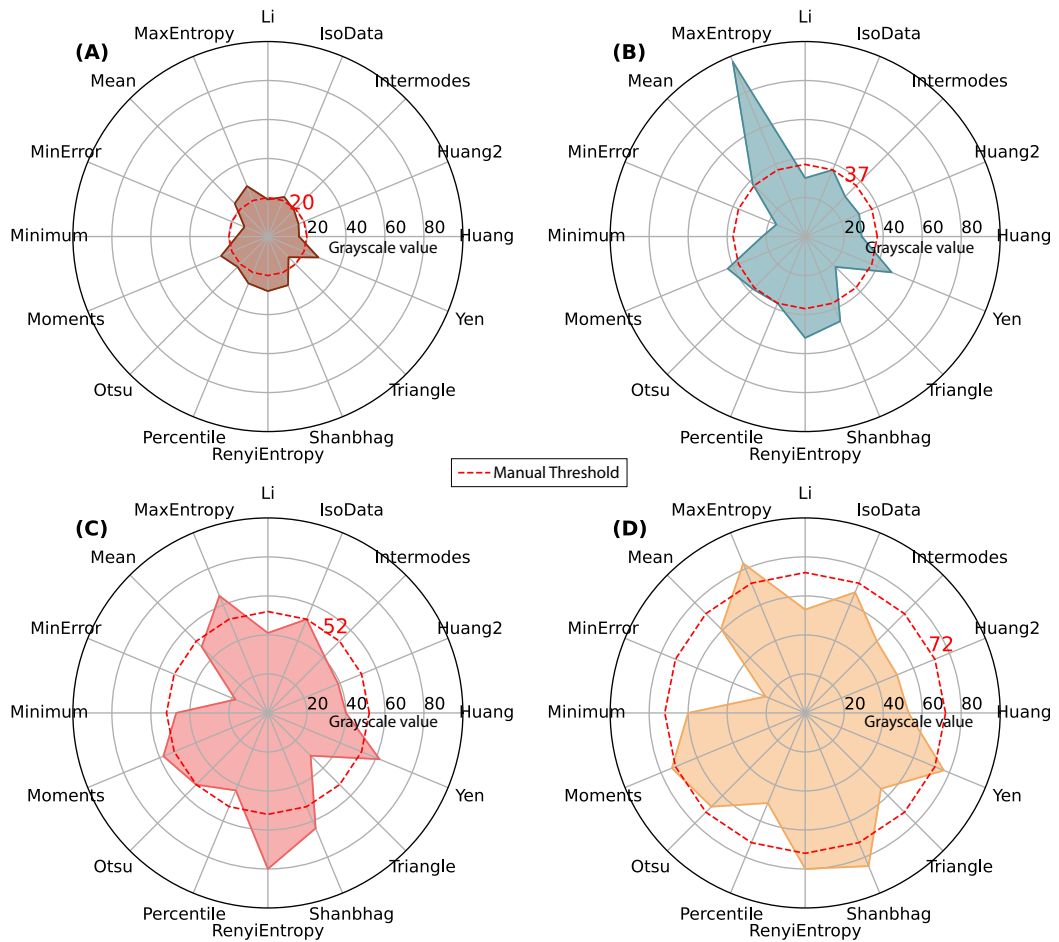
Figure 5.5: *Thresholded values for BSE images at (A) 10 keV (B) 15 keV (C) 20keV, and (D) 25 keV. The red dotted lines indicate the threshold values assessed manually.*

associated with the voids of the cenospheres. Figure 5.6 A illustrates the plotted area and perimeter changes that represent the void regions in the acquired SEM-BSE images. The general trend in the gradient values for the area curve decreases with increasing incident beam energy, whereas the perimeter curve exhibits slight fluctuations, particularly in segment F. This fluctuation is attributed to the increased number of segmented pixels at the void edges caused by higher voltages, leading to an increase in the perimeter of the void. Consequently, this fluctuation in the perimeter gradient does not effectively represent the behaviour of voids when exposed to high-energy incident beams (e.g., 25 keV). A pronounced gradient is observed at the lower incident beam energies (10 - 15 keV), which suggests that voids are more sensitive to changes in the incident beam energies. As the incident beam energies increase, the gradient values decrease and stabilise with respect to changes in the beam energies. This observation indicates the existence of a minimum energy threshold that is required to exhibit the void region and accurately characterise

particles as cenospheres or solid spheres using the SEM-BSE technique. Furthermore, assessing voids at lower energy levels introduces higher vulnerability in the characterisation process. The overall behaviour of SEM-BSE imaging on cenospheres can be attributed to the increasing depth of electron penetration (resulting in an increase in the ionisation volume) with increasing incident beam energy. At lower incident energies, the depth of penetration is reduced, making it impossible to identify voids beyond the ionisation volume. Conversely, at higher incident beam energies, there was only a slight difference in the volume of the void because nearly the entire void volume was exposed within the interaction volume. In this study, an incident beam energy of approximately 12–15 keV was sufficient for classification. However, quantifying the cell wall thickness using this method is challenging because it may vary depending on the applied incident beam energy (refer to Figure 5.6). Nonetheless, this non-destructive approach to classify cenospheres and solid spheres is highly effective compared to the assumption that all floating particles are cenospheres.
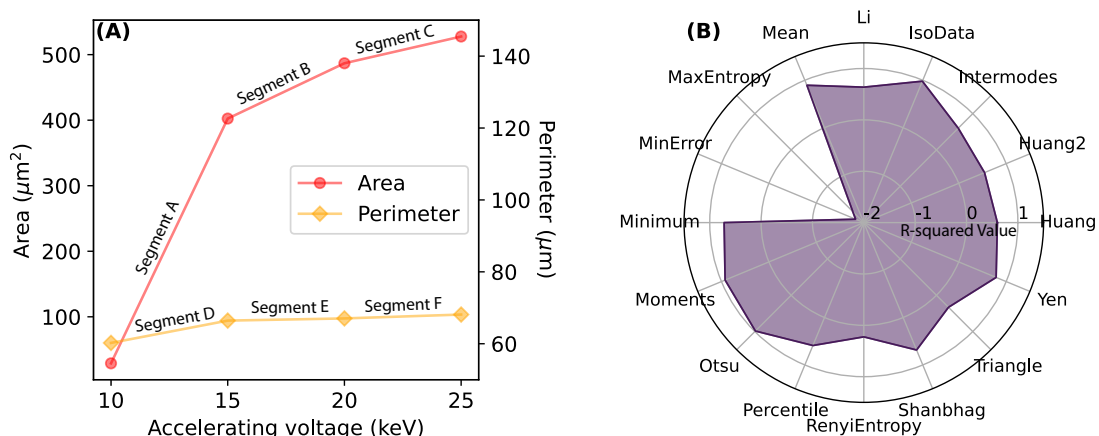
Figure 5.6: *(A) Area and perimeter of void regions for the SEM-BSE images (B) Coefficient of determination for the employed thresholding methods.*

5.3   Cell wall thickness of cenospheres

The thickness of the cell wall in cenospheres significantly influences their modification for use as an adsorbent. However, quantifying the imperceptible structures within cenospheres poses challenges. Hence, the most effective method for assessing the thickness of cell walls in cenospheres involves measuring the cell walls of broken cenospheres. Multiple measurements were taken from the exposed cell wall segments of a broken cenosphere (from SEM-SE images), and the arithmetic mean was calculated to determine cell wall thickness. Figure 5.7 A illustrates a broken cenosphere and annotates the measurements obtained from cell wall segments. In this
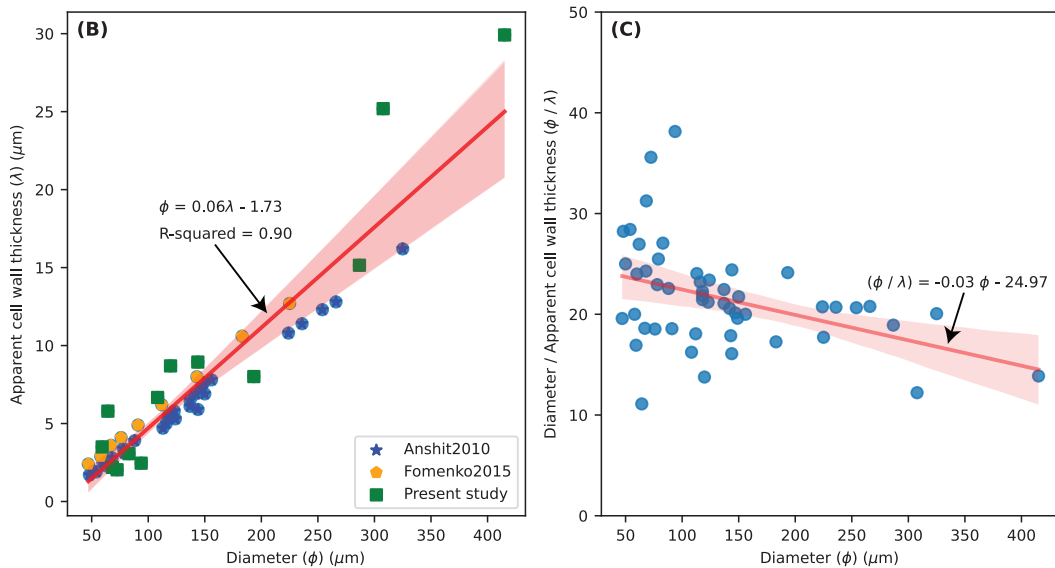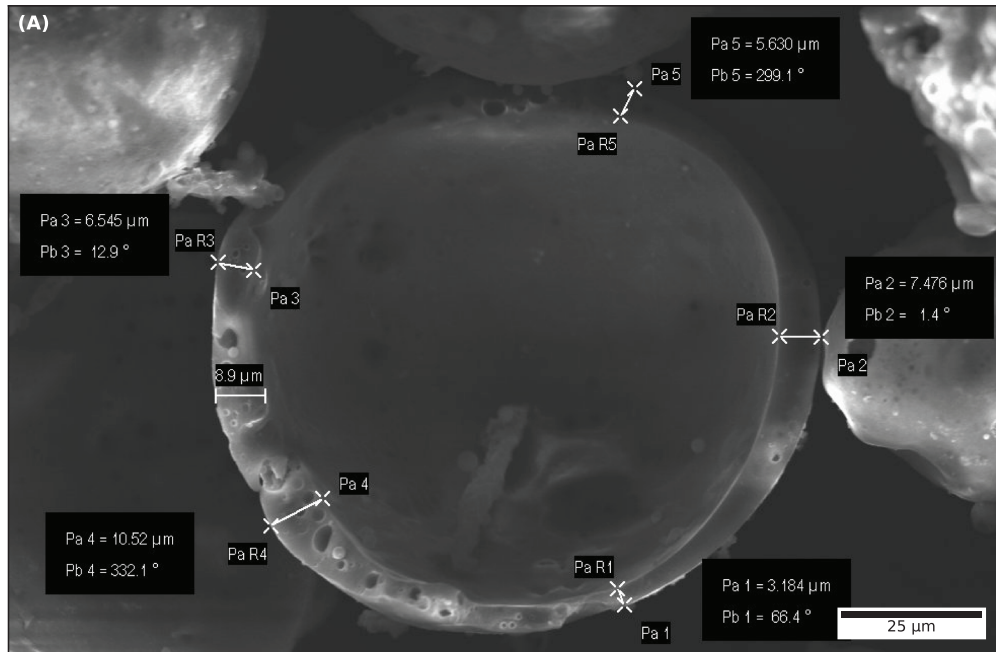
Figure 5.7: *(A) Broken cenosphere (B) Distribution of apparent cell wall thickness with respect to cenosphere diameter. (C) Distribution of the ratio between the diameter of the cenosphere and the cell wall thickness in relation to the diameter. The light red band in (B) and (C) depicts the 95% confidence interval of regression lines.*

cenosphere, the cell wall thicknesses of the six different segments were found to be 3.184, 5.630, 6.545, 7.476, 8.900, and 10.520 μm. The heterogeneity in cell wall thickness among cenospheres introduced a variance of 5.509 μm, making the determination of a precise value for cell wall thickness quite challenging. Figure 5.7

41

B presents the distribution of the cell wall thicknesses in relation to the corresponding cenosphere diameters. In addition, the plot includes the cell wall thickness distribution obtained from previous studies, such as Anshits et al. (2010) and Fomenko et al. (2015). The variation in cell wall thickness among segments of small cenospheres was relatively minimal compared to cenospheres with larger diameters. This observation is further supported by the non-scattered distribution of the cell wall thickness in the smaller diameter range. In the present study, a linear relationship was observed between cell wall thickness and diameter, with a coefficient of 0.08, intercept of -2.34, R-squared value of 0.92, and mean squared error (MSE) of 6.13. These results also support the findings of Ranjbar and Kuenzel (2017). Furthermore, when combining the results of previous studies with those of the present study, a general linear relationship emerged between cell wall thickness and diameter. The general equation describing this relationship is as follows:

$$\phi = 0.06\lambda - 1.73 \tag{5.1}$$

where ϕ and λ denote the cell wall thickness and cenosphere diameter, respectively. This relationship can be applied to cenospheres with diameters greater than 30 μm, owing to the inherent limitations of the equation.

Furthermore, the ratio between the diameter of the cenosphere and the measured cell wall thickness varied significantly. For smaller spheres, this ratio ranged from 10 to 40 times, whereas for larger spheres above 150 μm, it settled approximately 20 times, as depicted in Figure 5.7 C. These findings align with those of a previous study by Ngu et al. (2007), who reported a ratio ranging from 20 to 30 for smaller particles (i.e., smaller diameter) and a relatively constant ratio of 20 for larger particles (Ngu et al., 2007; Ranjbar and Kuenzel, 2017).

5.4 Characterisation of solid spheres and cenospheres through X-ray microanalysis

The foundation for characterisation relied on Si Kα intensity profiles obtained from cenospheres (hollow spheres) and solid spheres recovered from the floating layer of the washing cycles. Specifically, the chosen characterisation profile is based on Si Kα line scans (referred to as ψ_{Si}), which traverse each individual spherical particle. Notably, the influence of the electron beam spot dimension in SEM was not considered in this study because its impact on larger electron interaction volumes was deemed negligible (Fournelle et al., 2016).

Figure 5.9 A displays a SEM-BSE image acquired at an accelerating voltage of 20 keV, showcasing a randomly selected sphere that exhibits an unexpected contrast
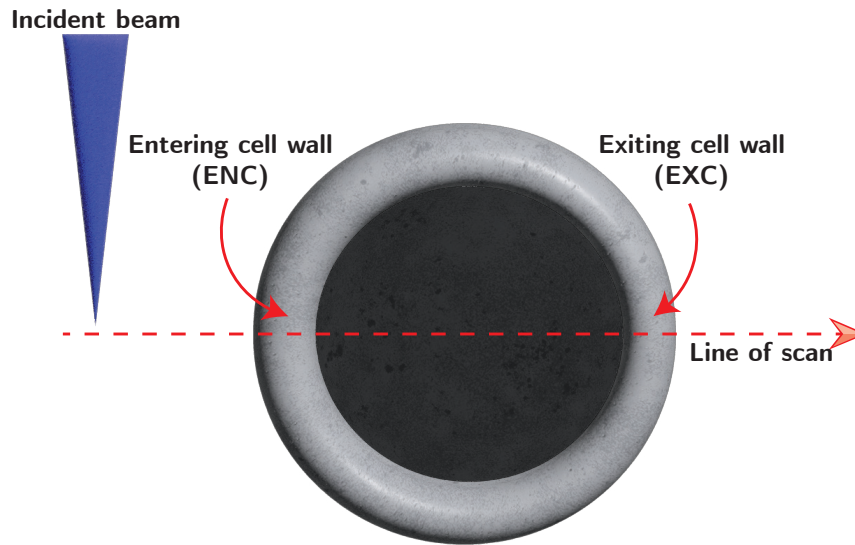
Figure 5.8: *Schematic illustrating a cenosphere with scanning line of incident beam, and its entering and exiting cell wall.*

trend. Within the sphere, a noticeably darker region is observable at the centre, featuring a contrast ratio of approximately 1.5 times in greyscale compared with the peripheral areas. This darker region suggests a reduction in the electron emission intensities compared with the solid spheres (Figure 5.9 D), implying the potential presence of a void within the probed object at the characteristic depth of the incident beam. Nevertheless, although SEM-BSE imaging provides valuable insights into the existence of distinct regions with varying physical characteristics, the intrinsic limitations of SEM-BSE imaging (in contrast to X-ray microanalysis), including low chemical sensitivity, limited depth of penetration, and lack of contrast between elements, pose significant challenges in differentiating and characterising this potential void from peripheral areas (i.e., the cell wall of cenospheres).

Figure 5.9 B shows the ψ_{Si} obtained at different accelerating voltages (15, 20, and 25 keV) for the selected sphere. Remarkably, two distinct regions with high-intensity Si Kα signals were detected at the edges of the scanned sphere, indicating their corresponding cell walls. In contrast, the central region exhibited a gradual decline in Si Kα intensity, followed by an increase towards the other peak, corresponding to the second cell wall located diametrically opposite. This characteristic trend provides compelling evidence of reduced Si Kα attenuation within the characteristic X-ray formation region compared with the cell walls of the sphere, thus supporting the potential existence of a region without Si. Moreover, the detected Si Kα intensity in the central region results from the cell wall positioned above the void, thereby confirming the presence of a void in the scanned sphere.

The relationship between the accelerating voltage and ψ_{Si} was further investigated to
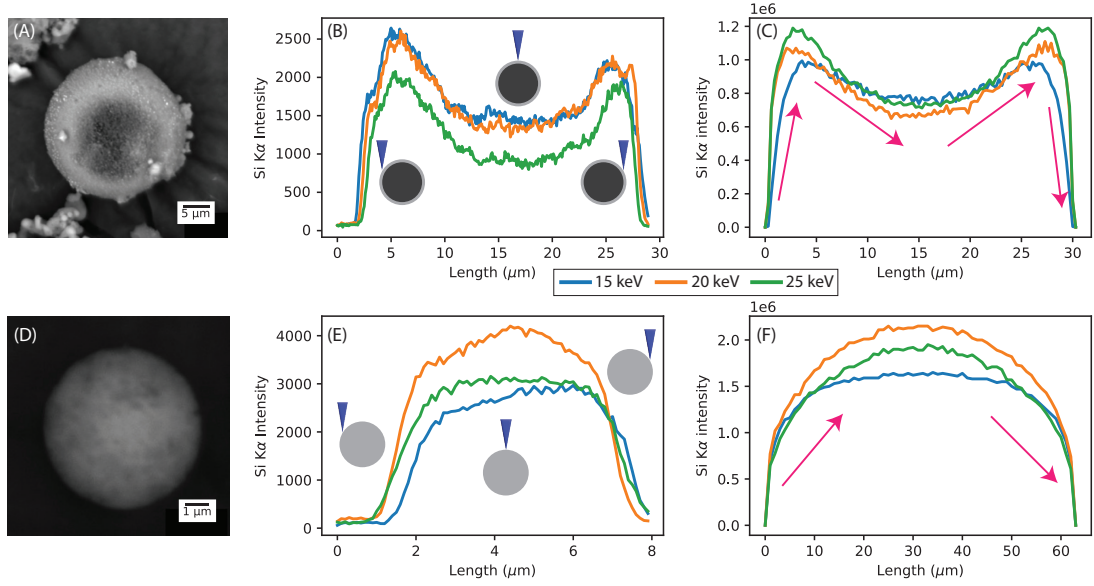
Figure 5.9: *(A) BSE image of a selected sphere. (B) ψ_{Si} of the sphere at 15, 20, and 25 keV. (C) Simulated ψ_{Si} under conditions identical to those in (B). (D) SEM-BSE image of the selected solid sphere. (E) ψ_{Si} obtained at 15, 20, and 25 keV. (F) Simulated ψ_{Si} corresponding to the acquisition conditions in (E).*

gain insight into electron interactions within the scanned sphere. As shown in Figure 5.9 B, the ψ_{Si} gradually increased with increasing accelerating voltage, reaching a peak at 20 keV before declining at 25 keV. The observed trend can be attributed to the extension of the ionisation volume beyond the confines of the scanning sphere at higher accelerating voltages (25 keV), resulting in a comparatively reduced ionisation volume compared with lower accelerating voltages (15 and 20 keV). Based on these observations, the total ionisation cross-sections (σ_{ion}) during electron interactions at the aforementioned accelerating voltages can be ranked as follows: $\sigma_{ion(15)} > \sigma_{ion(20)} > \sigma_{ion(25)}$.

Upon the examination of ψ_{Si}, Figure 5.9 B, it becomes evident that the Si Kα peak intensity values for the entering cell wall (ENC) surpass those of the exiting cell wall (EXC) at 15 and 20 keV (refer Figure 5.8). This disparity suggests a difference in σ_{ion} between these two regions (i.e., $\sigma_{ion(ENC)} > \sigma_{ion(EXC)}$). These variations could be attributed to differences in the individual cell wall thicknesses, as observed in various broken cenospheres. However, at 25 keV, both cell walls exhibit equal Si Kα peak intensities because of the penetration depth of the high-energy beam (i.e., high accelerating voltage) that effectively traverses through the cell wall, resulting in similar σ_{ion} at ENC and EXC (lower than those at 15 and 20 keV). This behaviour of high-energy beams is critical for resolving structural features such as cell wall thickness within cenospheres. The potential merits associated with this phenomenon are discussed extensively in Section 5.7.

44

Parallel to the investigation of cenospheres, we conducted a comparative study of a solid sphere with a diameter of 6.5 μm. The selection of a sphere with a small diameter was based on the current limitations in distinguishing between solid and hollow spheres solely through SEM imaging. To address this, we chose a sphere size that would enable electrons to permeate the entire depth of the sphere during sequential scans, thereby validating its solid composition. Fig. 5.9 D shows the SEM-BSE image of the solid sphere, while Fig. 5.9 E presents the ψ_{Si} obtained at accelerating voltages of 15, 20, and 25 keV. The decreasing trend of ψ_{Si} intensities with increasing accelerating voltage aligns with the previously discussed concept of high-energy beam ionisation volume and affirms the solid nature of the scanned sphere. Notably, the identical ψ_{Si} to the experimental data (Fig. 5.9 E) with no reduction in the Si Kα intensity in the central region of the sphere provides compelling evidence for the existence of two distinct ψ_{Si} for the solid spheres and cenospheres.

5.5 Computational modelling and simulations of electron interactions

To substantiate previous experimental results, computational simulations using MC X-ray software were performed to analyse the behaviour of a hollow silica sphere (Ranjbar and Kuenzel, 2017) with a diameter of 30 μm and a cell wall thickness of 2 μm (approximately derived from ψ_{Si}) when subjected to varying accelerating voltages ranging from 15 to 25 keV. In addition, a solid silica sphere with a diameter of 6.5 μm under similar accelerating voltages was simulated for comparative purposes. The computed results for both hollow and solid spheres are shown in Figure 5.9 C and Figure 5.9 F respectively, closely resemble the experimental outcomes. These findings underscore the utility of the simple line scan method (i.e., ψ_{Si}) for reliably classifying spherical CFA particles as solid or hollow.
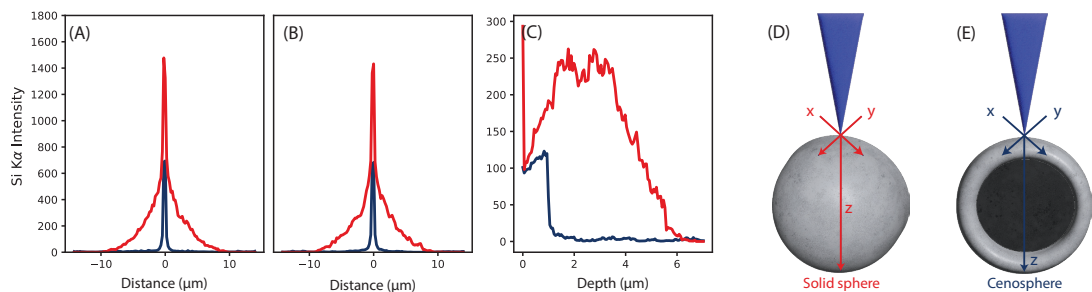
Figure 5.10: *The energy loss profiles of electrons along the (A) x-axis, (B) y-axis, and (C) z-axis at 20 keV. Axis of the energy loss profiles for (D) solid sphere and (E) cenosphere.*

The energy loss of electrons along the x-, y-, and z-axes when a 20 keV beam is directed through the centres of both a solid sphere (with a diameter of 10 μm) and

a hollow sphere (with the same diameter and 1 μm cell wall thickness) are shown in Figure 5.10 A - C. The profiles of the solid and hollow spheres exhibit a striking contrast. This discrepancy arises from the divergent interaction patterns experienced by electrons passing through these structures. In the case of a solid sphere, electrons interact with atoms within the potential ionisation volume of the sphere. However, in a hollow sphere, electrons solely interact with atoms in the cell wall. This fundamental distinction is reflected in the total energy loss profiles of the spheres. Notably, an abrupt decrease in energy loss is observed near the periphery of the inner cell wall of the hollow sphere (i.e., at 1 μm), as electrons traverse regions without Si atoms (i.e., the void region), resulting in a reduced ionisation volume within the hollow sphere compared with its solid counterparts under a given accelerating voltage.

5.6 Characterisation threshold for cenospheres
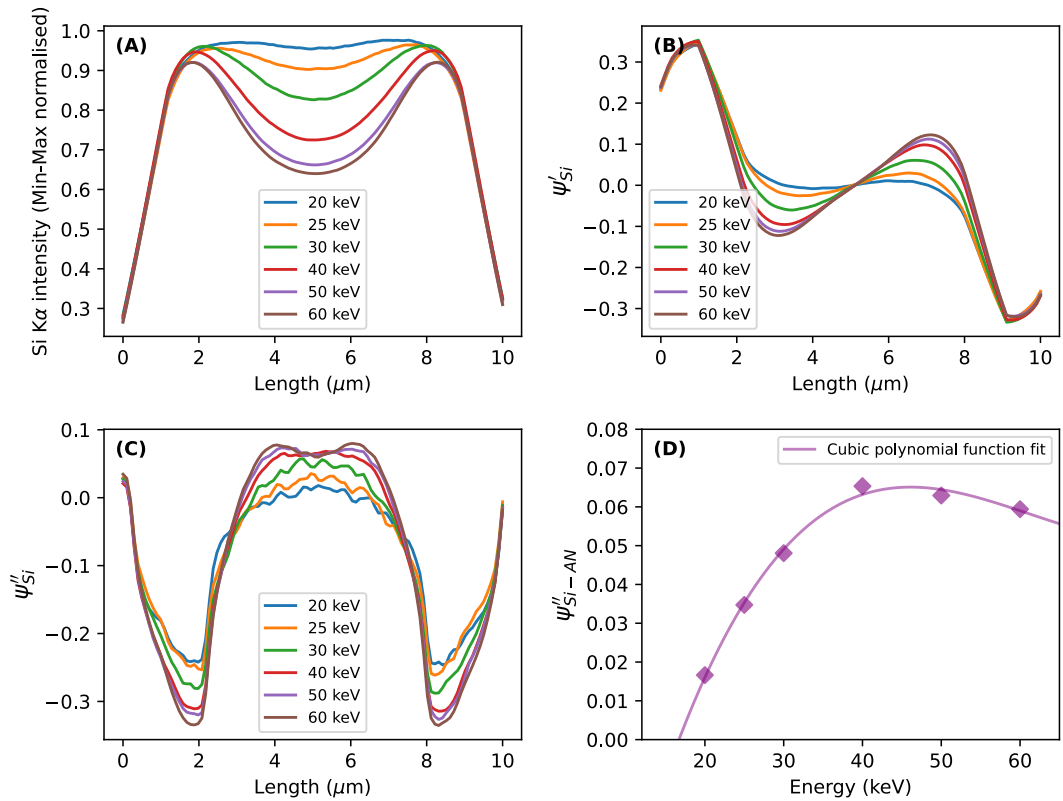
Figure 5.11: *(A) ψ_{Si} from a hollow sphere. (B) ψ'_{Si} for the identification of assessment node (AN). (C) ψ''_{Si} for the acquisition of ψ''_{Si-AN} values. (D) Distribution of ψ''_{Si-AN} with the increasing accelerating voltages.*

Accurately characterising the structures of solid and cenospheres becomes increasingly challenging as the accelerating voltage of the incident beam decreases. This challenge is primarily attributed to the decreasing ionisation depth of the

incident beams with decreasing accelerating voltages. This difficulty ultimately reaches a threshold at which the electrons cannot pass through the cell wall region into the void, resulting in similar ψ_{Si} for both the solid and cenospheres. This observation emphasises the importance of selecting appropriate accelerating voltages during the characterisation process. In addition, the subjective interpretation of ψ_{Si} from person to person further exacerbates these challenges. To address these issues, this section proposes a technique that effectively distinguishes between solid and cenospheres by assessing the second derivative of the Si Kα profiles (ψ_{Si}'').

The ψ_{Si} of the solid spheres and cenospheres exhibit distinct concavity characteristics. The solid spheres display a concave-down profile, indicating a maximum point ($\psi_{Si}'' < 0$) when evaluated using the ψ_{Si}'', as shown in Figure 5.9 F. In contrast, the cenospheres demonstrate a concave-up profile, signifying a minimum point ($\psi_{Si}'' > 0$) at the centre of the identified void, as shown in Figure 5.9 C. As the accelerating voltage decreases, ψ_{Si-AN}'' of the cenosphere profile approaches zero (where AN refers to the assessment node). Eventually, a specific point is reached where ψ_{Si}'' surpasses zero and becomes negative, mirroring the behaviour observed in the solid sphere profile. At this critical juncture, the ψ_{Si} of both solid spheres and cenospheres become indistinguishable. In this study, the accelerating voltage at which $\psi_{Si-AN}'' = 0$ was considered as the minimum accelerating voltage for the cenosphere characterisation. To determine this voltage, the AN for ψ_{Si}'' was identified as the point where ψ_{Si}' becomes zero. This point represents the gradient of the profile at the centre of the identified void. By plotting the corresponding values of ψ_{Si-AN}'' at various accelerating voltages, a theoretical threshold value ($\psi_{Si-AN}'' = 0$) for the cenosphere characterisation could be derived. This approach allows the assessment of changes in concavity and facilitates a numerical comparison across different conditions.

A cenosphere with a diameter of 10 μm and a cell wall thickness of 2 μm was chosen to determine the threshold accelerating voltage. Figure 5.11 A shows the ψ_{Si} of the selected cenosphere with increasing accelerating voltages. Figure 5.11 B and Figure 5.11 C illustrates ψ_{Si}' and ψ_{Si}'', respectively. Figure 5.11 D shows the trend of the ψ_{Si-AN}'' as the accelerating voltage increases. Notably, the cubic polynomial function demonstrates a very strong fit to the data, with the highest correlation of the determination value (0.996) when compared to the quadratic, linear, and logarithmic functions. Using the fitted model, the theoretical threshold value for the characterisation of the chosen cenopshere is calculated as 19.3 keV. Conversely, the maximum depth of penetration for the 19.3 keV beam at the 99% X-ray intensity level reached approximately 3.98 μm, representing an increase of approximately 99% intensity compared to the 2 μm. These findings suggest that the selected incident beam has the capacity to marginally characterise cenospheres with a cell wall thickness of approximately half of its penetration depth at a 99% X-ray intensity

level. Nevertheless, it is important to note that this theoretical threshold value may vary depending on the inherent properties of the cenosphere such as the density and porosity of the cell wall. However, a fair approximation of the probing acceleration voltage could be estimated.

5.7 Determination of cell wall thickness through X-ray microanalysis
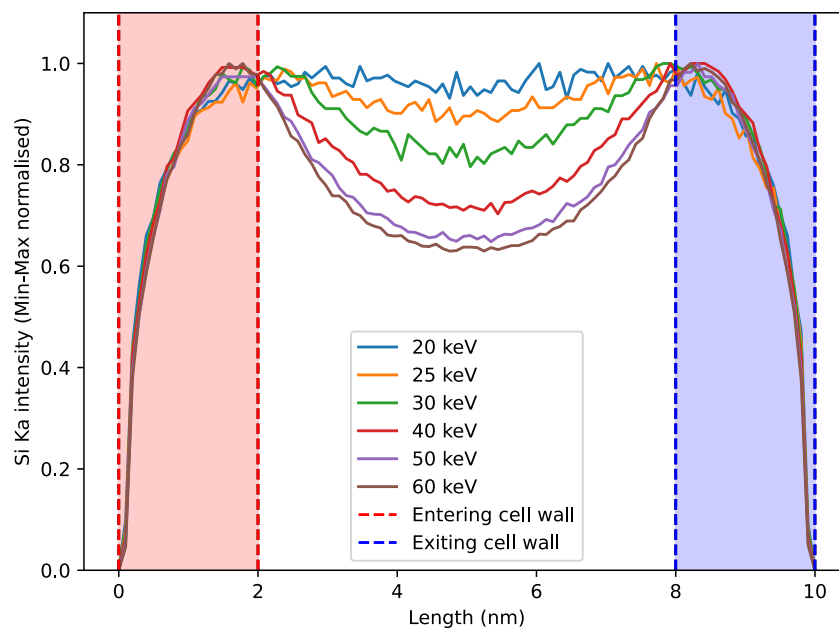
Figure 5.12: ψ_{Si} *of cenospheres at varying accelerating voltages (20-60 keV).*

Measuring the thickness of cell walls in cenospheres remains a significant challenge because of the absence of nondestructive techniques. While prior investigations have utilised approaches such as the observation of broken cenospheres through SEM or approximation equations, these methods suffer from drawbacks, including experimental invasiveness or insufficient accuracy owing to the heterogeneous properties of the particles involved (Anshits et al., 2010; Fomenko et al., 2015). In this study, a novel, non-invasive technique was introduced which is capable of quantitatively determining the cell wall thickness of individual cenospheres. This approach leverages EDS analysis (previously discussed in Section 5.4), which classifies spheres as either solid or hollow while simultaneously providing insight into the cell wall thickness of the cenospheres.

In the cenosphere, the optimal condition for maximum Si Kα emission (i.e., peaks at ψ_{Si}) occurs during the stages of interactions with higher ionisation volumes between the incident electrons and the cell wall. However, for cases where a significant portion
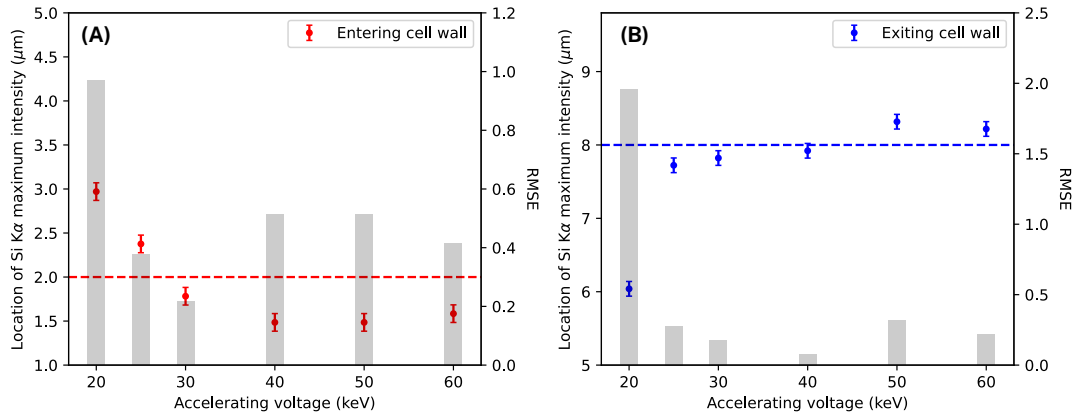
Figure 5.13: *(A) Location of maximum Si Kα emission at the entering cell wall (ENC). (B) Location of maximum Si Kα emissions at the exiting cell wall (EXC).*

of the electron beam permeates through the cenosphere (i.e., at a higher accelerating voltage), the peak intensity may be observed at longer path lengths of electrons within the cell wall, particularly towards the inner edge. Under these circumstances, for situations involving lower incident energies, the uncertainty associated with determining the cell wall thickness is approximately half the resolution of the ionisation volume. Conversely, for situations involving higher incident energies, the accuracy remains relatively high because the interaction volume resembles a ribbon structure rather than a droplet structure.
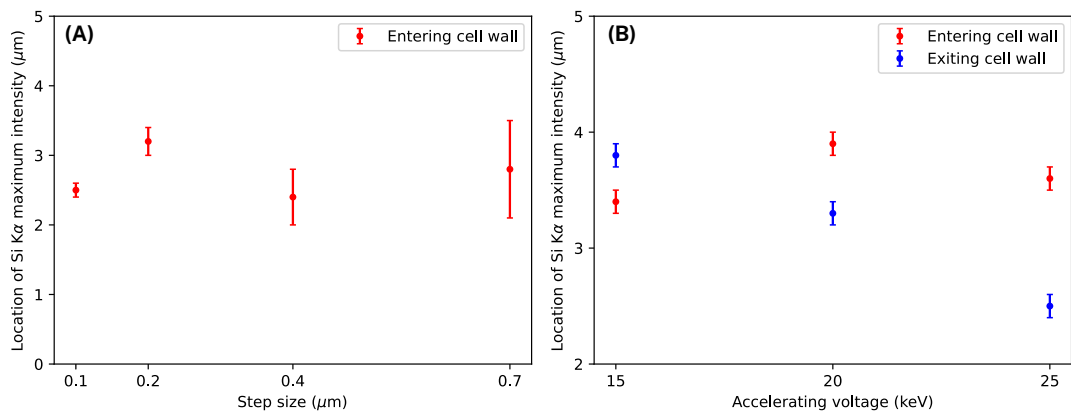
Figure 5.14: *(A) Location of the maximum Si Kα intensity for different step sizes. (B) Calculated cell wall thickness of the ENC and EXC of the cenosphere shown in Figure 5.9 A.*

Figure 5.12 presents the simulation of ψ_{Si} of cenospheres with 10 μm diameter and 2 μm cell wall thickness at varying accelerating voltages (20-60 keV). Figure 5.13 A and B shows the location of maximum Si Kα emissions at both ENC and EXC. At 20 keV, although the incident beam was able to penetrate a 2 μm cell wall, its Root

Mean Square Error (RMSE) was relatively high (0.98) compared to the average RMSE across different energies, i.e., 25-60 keV, (0.41) (RMSE was calculated by comparing it to the true cell wall thickness of 2 μm). Similarly, the RMSE for 20 keV was again relatively higher at the EXC when compared to the average RMSE across different energies (RMSE$_{(20)}$=1.96 vs Average RMSE$_{(25-60)}$=0.21). Adjustment to the position of the maximum intensity of the 20 keV beam by half of its radial resolution (i.e., 1.73 μm for 99% X-ray intensity) reduces the RMSE values for the ENC and EXC to 0.76 and 0.23, respectively. Nonetheless, the use of higher energies provided a more accurate measurement of cell wall thickness, resulting in lower RMSE values averaged across various energies, i.e., from 25-60 keV (Average RMSE$_{(25-60)}$=0.41 and 0.21 for ENC and EXC, respectively).
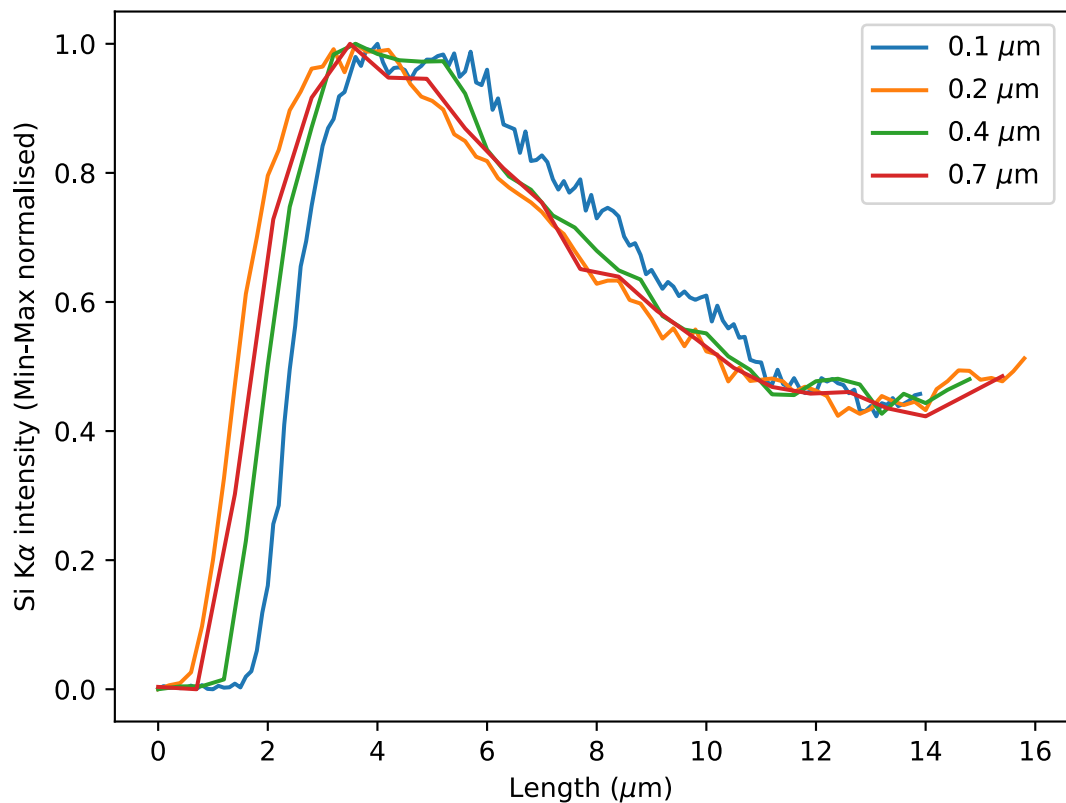
Figure 5.15: ψ_{Si} at the cenosphere ENC with varying step sizes.

The cell wall thickness of the probed cenosphere (i.e., Figure 5.9 A) of both ENC and EXC at three different incident energies (15, 20, and 25 keV) is illustrated in the Figure 5.14 B. The cell wall thickness determined by the all three incident energies are within a narrow range of 3.4-3.9 μm $\pm$ 0.1 μm for the ENC, with less variance than the EXC, whose thickness varies from 2.5-3.8 μm $\pm$ 0.1 μm. In addition, the simulated plots in Figure 5.13 B demonstrate a similar trend in the EXC and suggest the need for a half radial resolution adjustment for low voltage interactions. Applying this adjustment to the value obtained at 15 kV, i.e., 3.8 μm $\pm$ 0.1 μm, suggests a tighter possible range

of cell wall thickness of 2.5-3.3 μm $\pm$ 0.1 μm. In summary, these findings underscore the importance of analysing cell structures at multiple energy levels, whether at high accelerating voltages or a combination of low and high accelerating voltages, with corrections for the lower voltage, to precisely determine their characteristics.

In addition, the influence of the resolution of ψ_{Si} (i.e., step size) was investigated to improve the efficiency of the characterisation and quantification of cell wall thickness. A cenosphere with a diameter of 30 μm was selected for this purpose, and ψ_{Si} were obtained at step sizes of 0.1, 0.2, 0.4, and 0.7 μm on the ENC (refer Figure **??** D). The observed shift in the Si Kα emission was attributed to the different step sizes and movement of scanning particles inside the equipment, which was beyond the control of the operator. Figure 5.15 shows the location of the maximum Si Kα intensity (i.e., cell wall thickness) with the different step sizes and the error values were determined by the size of the respective step. As the characterisation is distinct at the employed incident beam energy (i.e., 25 keV), it can be assumed that the beam permeates through the scanned sphere; thus, there is no need for a half-radial resolution adjustment. Consequently, the 0.1 μm step size produced the closest estimate, with a cell wall thickness of 2.5 ($\pm$0.1) μm. The RMSE for the 0.2, 0.4, and 0.7 μm step sizes were 0.7, 0.1, and 0.3, respectively. Almost all the line scans, except for the 0.2 μm step size, fell within the 2.5 ($\pm$0.1) μm range when considering their respective uncertainty values (i.e., error terms).

These results highlight the significance of considering varying energy levels and using finer resolutions to obtain reliable and detailed insights into the cenosphere structures.

5.8 Synthesis of zeolites from bottom coal fly ash

Zeolites can be directly synthesised from oven-dried bottom CFA. However, employing secondary pre-processing techniques, such as grinding, acid leaching, and sieving, can significantly enhance the purity of zeolites by eliminating additional materials from the bottom CFA. Moreover, biometallurgy offers environmentally benign methods, such as bioleaching and biosorption, to extract trace elements and further enhance zeolite purity (Kanesalingam et al., 2023; Dev et al., 2020). In Figure 5.16 B and C, the SEM-SE image showcases the synthesised zeolite obtained from oven-dried CFA bottom samples from the washing cycles. This particular zeolite synthesis employed a two-step alkaline fusion process (Cardoso et al., 2015).

The present method, i.e., two-step alkaline fusion process, yielded a mixture of various zeolites, including zeolite L, ITQ-49, and zeolite (K, Ba)-G and L, each exhibiting unique shapes. Figure 5.17 B illustrates the XRD curves obtained for the synthesised zeolite samples, confirming the presence of multiple zeolites. Zeolite L
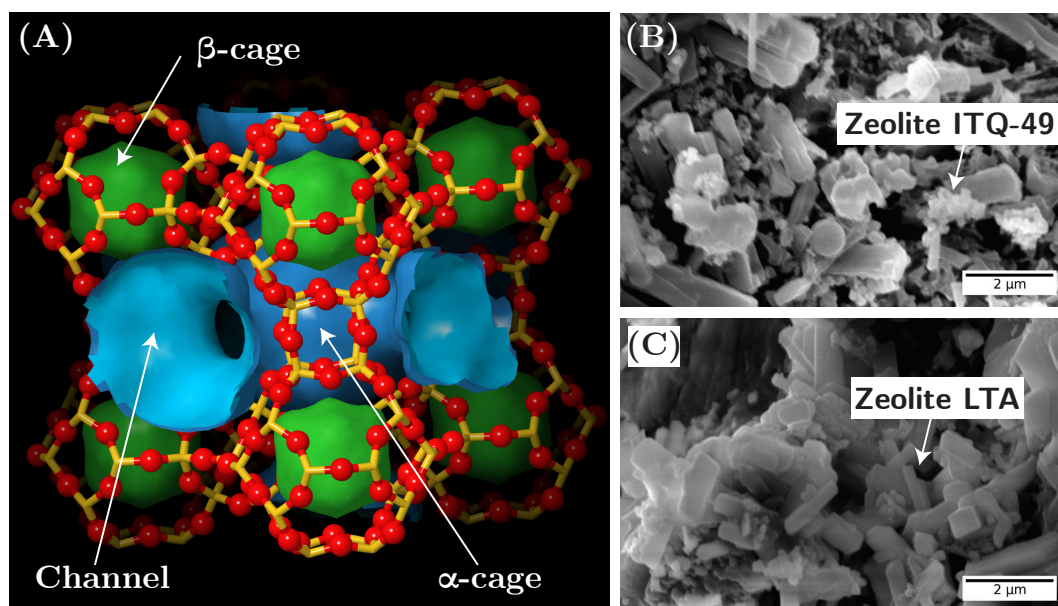
Figure 5.16: *(A) Structure of the synthesised Zeolite-LTA. (B) and (C) SEM-SE image of synthesised zeolites.*

acts as a molecular sieve, enabling the separation of molecules based on their size and shape (Figure 5.16 A). Moreover, zeolite L can be synthesised with varying pore sizes, providing submicron and nanoscale sieving capabilities (Ruiz et al., 2005). Zeolites (K, Ba)-G, L, and L share similar structures (Newsam et al., 1985), whereas zeolite ITQ-49, a germanosilicate zeolite, features small pores and large non-spherical cavities accessible through a one-directional system (Li et al., 2015). Different zeolite types can be produced by adjusting initial synthesis parameters (Blissett and Rowson, 2012).

Furthermore, an intriguing observation is that the bottom sample after seven washing cycles contained a noticeable amount of zeolites, as identified by the increased crystallinity in the XRD plot shown in Figure 5.17 A. This suggests that the washing cycle employed also exhibits similarities to existing zeolite synthesis methods, involving the dissolution of specific amounts of Si and Al from CFA. The additional formation of zeolites after washing cycles effectively sequesters trace metals, particularly hazardous metals, by encapsulating them within newly generated zeolite materials, rather than allowing them to remain on the surface (Belviso et al., 2015). This process ensures safer opportunities for the use of the bottom layer for refilling purposes.

Zeolites serve as cost-effective and sustainable adsorbents for wastewater treatment, particularly for the removal of heavy metals and ionic species such as ammonium, chloride, fluoride, nitrate, phosphate, and sulphate from industrial wastewater, due
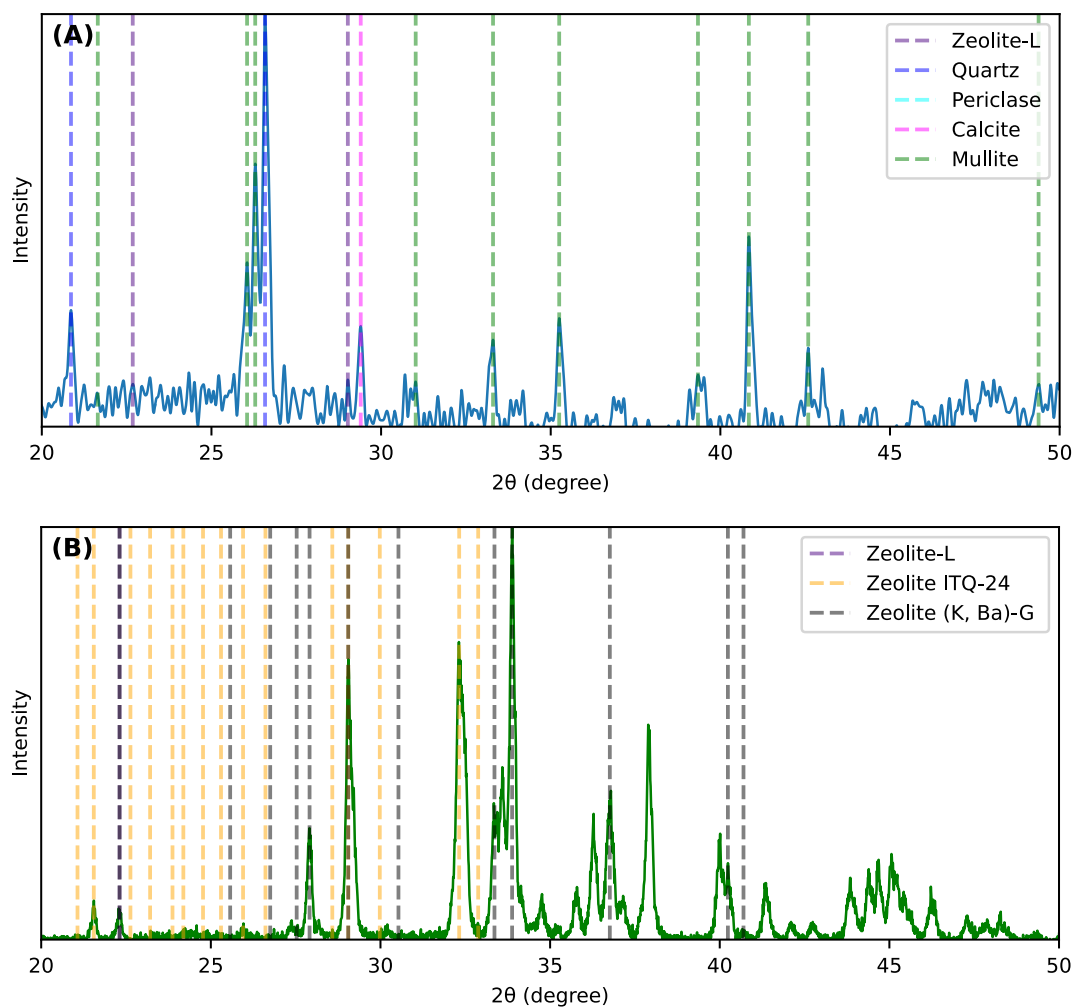
Figure 5.17: *XRD plot of the (A) bottom sample and (B) synthesised zeolites.*

to their remarkable cation-exchange capacity resulting from their abundant negative charges and large pores (Wang and Wu, 2006; Chen et al., 2022b; Abdellaoui et al., 2021). Additionally, the surface modification of synthesised zeolites offers further advantages in achieving the specific adsorption and mobility requirements of elements (Neupane and Donahoe, 2012; Karakasi and Moutsatsou, 2010).

5.9 Extraction of elements from bottom coal fly ash

Figure 5.18 A displays the EDS spectrum of the oven-dried bottom sample, revealing the presence of various elements, including major elements such as Si, Al, Fe, and Ti, as well as trace elements such as V, Ga, Ge, Mo, and Se. To investigate the spatial distribution of these elements, Figure 5.18 B - M illustrate the distribution maps of the selected elements. Si and Al were the prominent elements, dominating the majority of
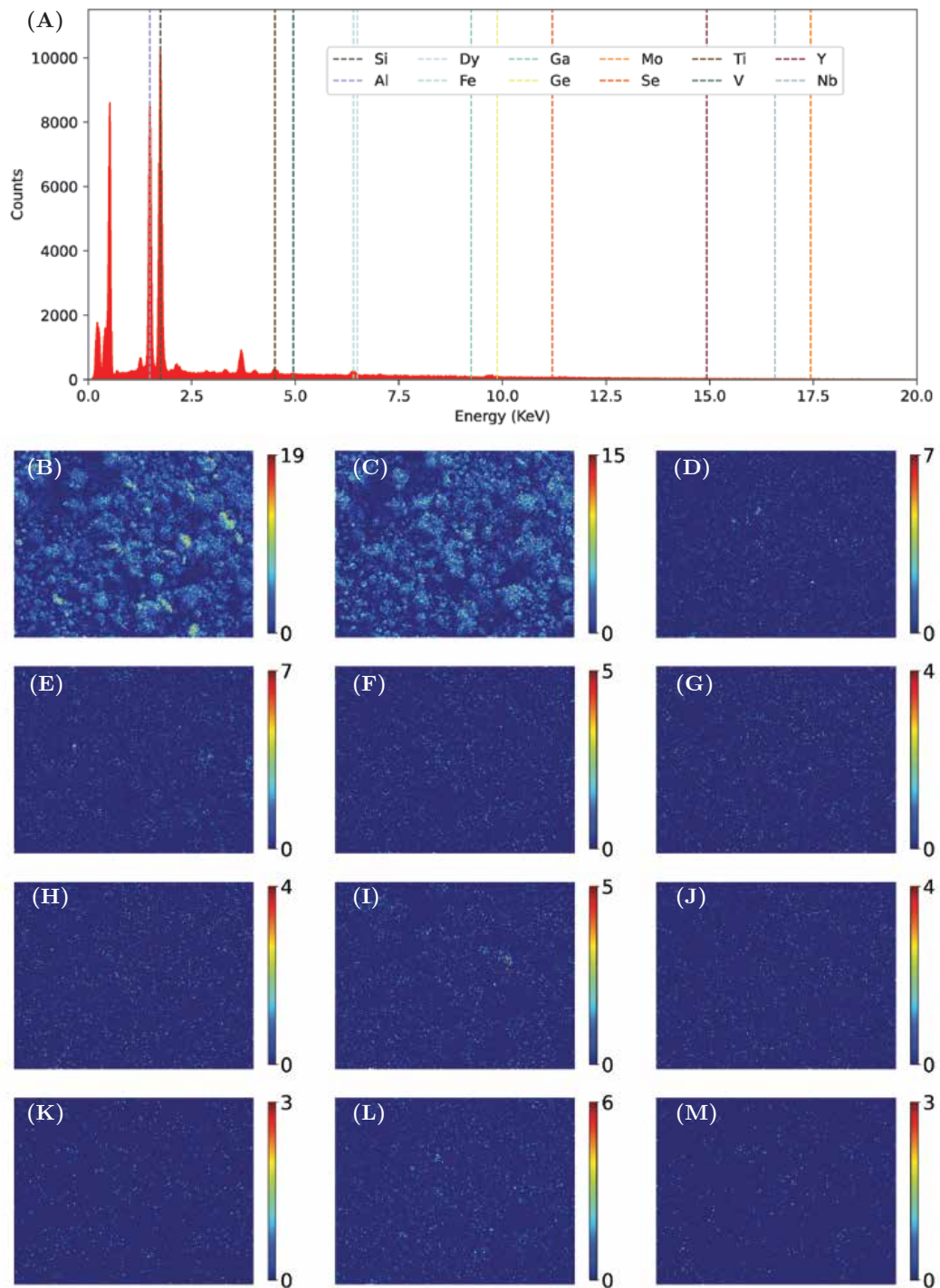
Figure 5.18: *(A) EDS of the CFA sample and intensity maps for (B) Silicon (Si), (C) Aluminium (Al), (D) Iron (Fe), (E) Titanium (Ti), (F) Vanadium (V), (G) Gallium (Ga), (H) Germanium (Ge), (I) Molybdenum (Mo), (J) Selenium (Se), (K) Yttrium (Y), (L) Dysprosium (Dy), and (M) Niobium (Nb)*

CFA particles.

To explore the relationship between particle shape in CFA and elemental distribution,
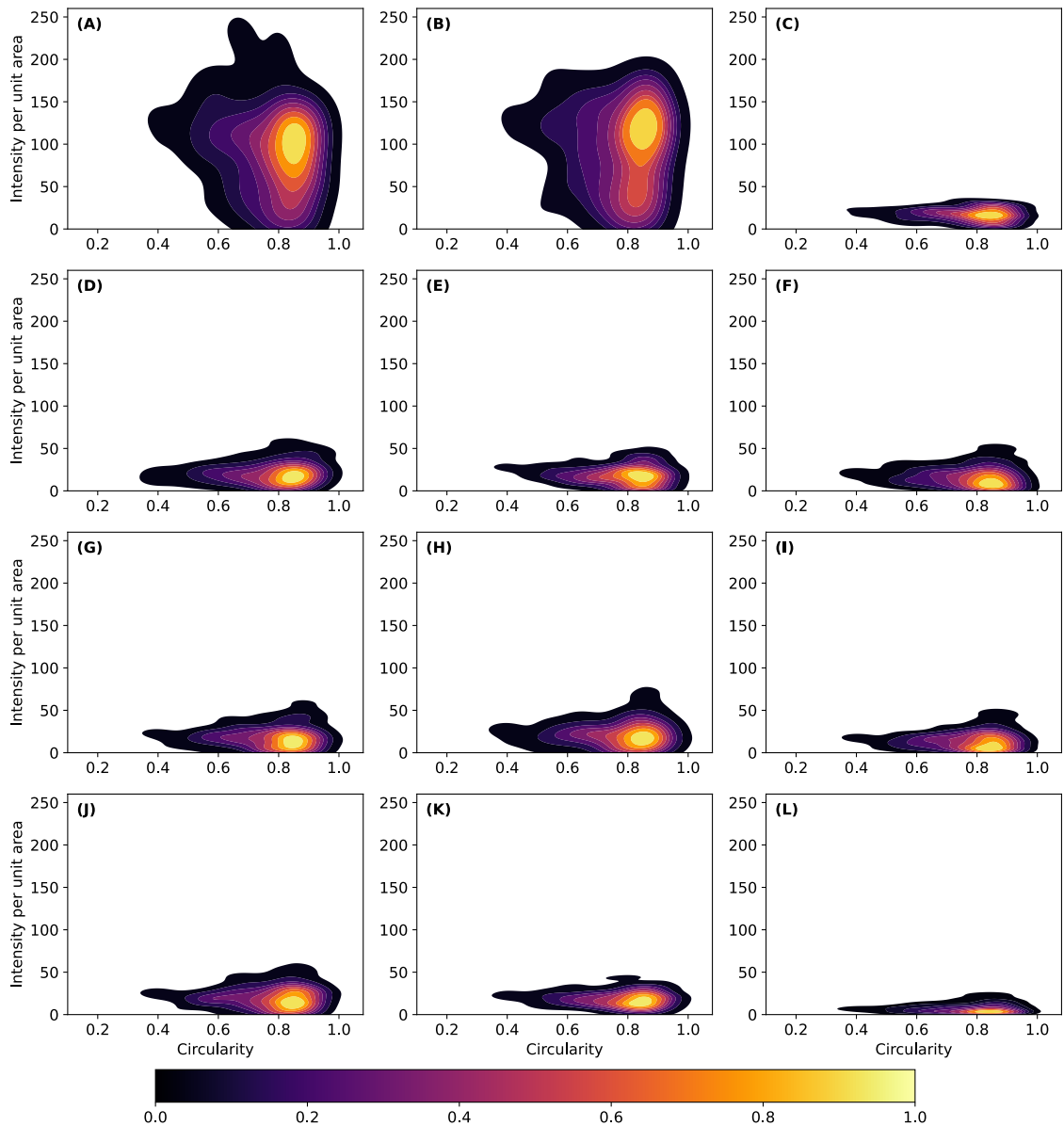
Figure 5.19: *Maps of intensity of segmented particle elements per unit area. Elements shown: (A) Silicon (Si), (B) Aluminium (Al), (C) Iron (Fe), (D) Titanium (Ti), (E) Vanadium (V), (F) Gallium (Ga), (G) Germanium (Ge), (H) Molybdenum (Mo), (I) Selenium (Se), (J) Yttrium (Y), (K) Dysprosium (Dy), and (L) Niobium (Nb).*

the analysis focused on measuring the intensity per unit area of elements across various particle shapes, which were represented by circularity values. This involved masking the EDS element distribution maps of individual elements using initial segments obtained from applying SAM to SEM-SE images. Following this, the intensity per unit area for each element was computed. Figure 5.19 A and B depict the distributions, showing that both Si and Al exhibit higher intensity in particles with circularity ranging from 0.8 to 0.9. This observation indicates that Si and Al tend to

55

concentrate on spherical particles rather than irregularly shaped particles. Additionally, the Si distribution shows the existence of irregular particles (with low circularity values, e.g., 0.65) that have a high intensity of Si per unit area. Moreover, the distribution of Al was more pronounced in spherical particles than that of Si. Furthermore, spherical particles showed a wide range of intensity per unit area, with Si ranging up to 250 and Al up to 175, suggesting the presence of cenospheres in lower quantities among CFA particles.

Fe and Ti showed similar distributions across various particle shapes (refer to Figure 5.19 C and D). The elemental distribution maps further emphasise the co-existence of both elements in the CFA particles, with no significant variation based on the particle shape. Furthermore, the bottom layer of the CFA shows potential as a secondary source of REEs. Figure 5.18 K and L demonstrate the significant distribution of Y and Dy elements within the oven-dried bottom sample. Notably, critical REEs, such as Y, Nd, Eu, Tb, and Dy, were found to be more abundant in CFA than in conventional sources, such as beach sand and rocks (Deng et al., 2022). The distribution of REEs across different particle shapes indicates their close association with Si and Al, consistent with previous studies suggesting that REEs primarily bind to the aluminosilicate matrix of CFA (Franus et al., 2015). These critical elements hold substantial value for the development of advanced products. Employing environmentally friendly techniques such as biometallurgy for their extraction can enable sustainable metal recovery from CFA (Kanesalingam et al., 2023; Fan et al., 2019).

CHAPTER 6

SIMULATION, MODELLING, AND AUTOMATION

6.1 X-ray microanalysis through Monte Carlo simulation

International Organization for Standardization (2013) defines Electron probe X-ray microanalysis (EPMA) as a contemporary method for both qualitatively assessing and quantitatively measuring the elemental composition of solid materials. This technique is applicable to various substances, including metal alloys, ceramics, glasses, minerals, polymers, and powders, offering spatial resolution on the order of approximately one micrometer laterally and in depth. EPMA relies on electron-stimulated X-ray emission and X-ray spectrometry mechanisms. The quantitative analysis involves directing an electron beam onto a specific point of the sample and then comparing the intensity of characteristic X-ray lines emitted by elements in the sample with those from standards of known composition. Corrections for matrix effects, which can either amplify or diminish X-ray production and emission intensity, are necessary. Utilising a beam voltage of 15 - 20 kV extends the interaction volume within the material to approximately one to a few microns. EPMA is best suited for examining samples that exhibit homogeneity at the micron scale. It combines spot quantitative analytical capabilities with electron microscope imaging, facilitating detailed X-ray mapping for compositional contrast (Llovet et al., 2021). However, applying EPMA to irregular surfaces or particles proves challenging due to assumptions such as a homogeneous sample volume, a flat polished surface, and the surface being normal to the incident beam.

Given these challenges, the Monte Carlo method emerges as a valuable tool for comprehending the limitations of EPMA, establishing optimal instrumental parameters for measurements, and laying the groundwork for quantitative procedures. This method involves numerically simulating electron trajectories within the sample, comprising sequential free flights of defined lengths that end in scattering events. As electrons change direction and lose energy, they may generate secondary electrons or protons. Trajectories conclude when electrons either stop within the material or escape from it (Pinard et al., 2012; Donovan et al., 2019). The number of characteristic X-rays is averaged over numerous simulated trajectories. The reliability of the Monte Carlo code hinges on the selected scattering model and simulation algorithm. However, the primary drawback lies in its stochastic nature and the presence of statistical uncertainties (Llovet et al., 2021). To mitigate these drawbacks, increasing the number of simulations and simulation time can be employed.
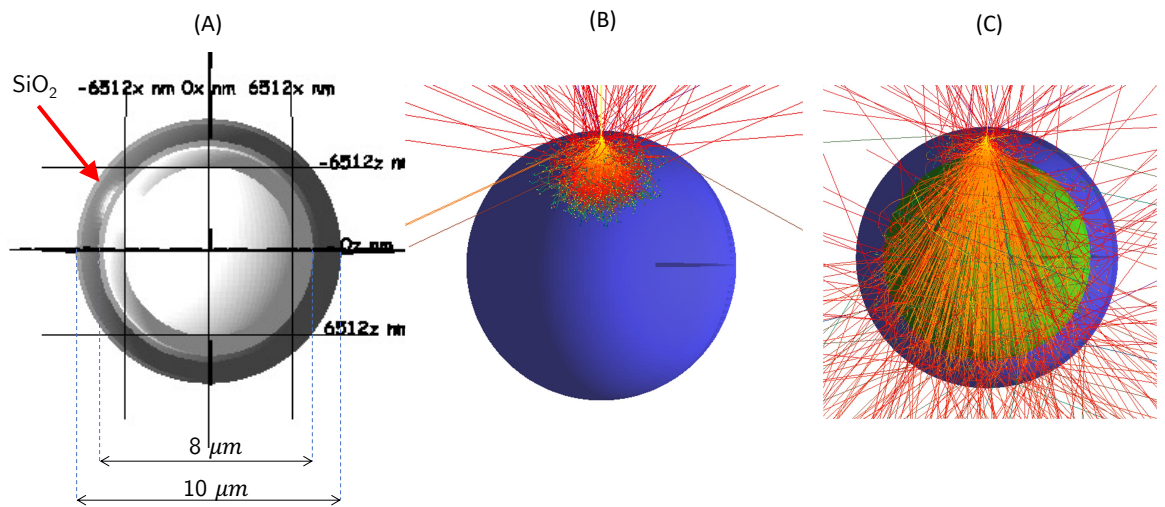
Figure 6.1: *(A) Modeled cenosphere for Monte Carlo simulation. Electron interaction within (B) a solid and (C) a cenosphere.*

Modelling cenospheres involves dealing with constraints like particle geometry, oblique surfaces, heterogeneous nature, and microstructures. This complexity necessitates employing the Monte Carlo approach to simulate electron interactions for analysis. In Figure 5.10, the cenosphere and solid sphere are modelled using various physical models:

- Atom model:
    - Energy loss: Bethe
    - Mean ionisation potential: Joy & Luo
    - Screening (cross-section & collision): Henoc & Maurice
    - Cross-section: Mott & Browning
    - Collision: Browning
    - Electron range: Kanaya & Okayama
    - Mass absorption coefficients: Chantler (2005)
- X-ray model:
    - Characteristics: Bote (2009)
    - Bremsstrahlung: Kirkpatrick & Wiedman
- Sample model:
    - Energy loss: Bethe, Joy, & Luo

A 20 keV beam is directed at these modelled cenospheres and solidspheres to

generate an energy loss profile used in the assessment outlined in Section 5.5. Figure 6.1 A displays the modelled cenosphere, while Figure 6.1 B and C illustrate electron interactions via the Monte Carlo method for a solid sphere and cenosphere, respectively.

6.2 pyDeepP2SA: a comprehensive python package for the analysis of particle properties

To ensure accurate, efficient, and rapid assessment of the SEM images of the CFA, a Python package called *pyDeepP2SA* was developed using a versatile deep learning model (refer Appendix A for documentation). This package simplifies the intensive coding processes for researchers, even those without extensive programming knowledge, to assess the shape and size distribution of particles of interest. Written in Python, this package takes advantage of its versatile software library and offers easy accessibility to researchers at various levels of programming proficiency (Rueden et al., 2022). The deployed package performs the same tasks as those extensively explored during the PSD analysis of the floating layer (refer to Section 5.1), utilising a state-of-the-art instant segmentation model (i.e. SAM). The model takes several general inputs for analysis, including the image to be analysed (even with annotations, bottom information bar, and scale bars), scale, thresholds (diameter and circularity), and the SAM checkpoint (i.e., model weights). The deployed model offers zero-shot generalisation, eliminating the need for prior training or pre-processing of the input image. Furthermore, the package can be executed on either a central processing unit (CPU) or a graphics processing unit (GPU) , with GPU processing (with CUDA compatibility) highly recommended for obtaining instant results. The PSD, circularity distribution, area, and perimeter of the individual particles can be easily derived from the package with statistical descriptions and plots. Additionally, this package allows the optimisation of SAM parameters, such as points per side, threshold for the prediction intersection over union (IOU) , and stability score, for the researcher requirements and computational limitations. The open-source code for this package is available at GitHub (Kanesalingam, 2023), which enables additional development and adaptability for researchers with specific requirements.

The performance of the developed package was analysed by applying it to a SEM-SE image of the floating layer shown in Figure 6.2 A without any pre-processing (with a bottom information bar). A threshold of 20 μm for the diameter and 0.85 for circularity was used, while the other model parameters were kept at their default values. To assess the performance, the particles were measured by experts using the manual measuring tool in ImageJ Fiji (Schindelin et al., 2012), with a measurement error of 1 μm. Of the 138 segments analysed (refer to Figure 6.2 B for identified
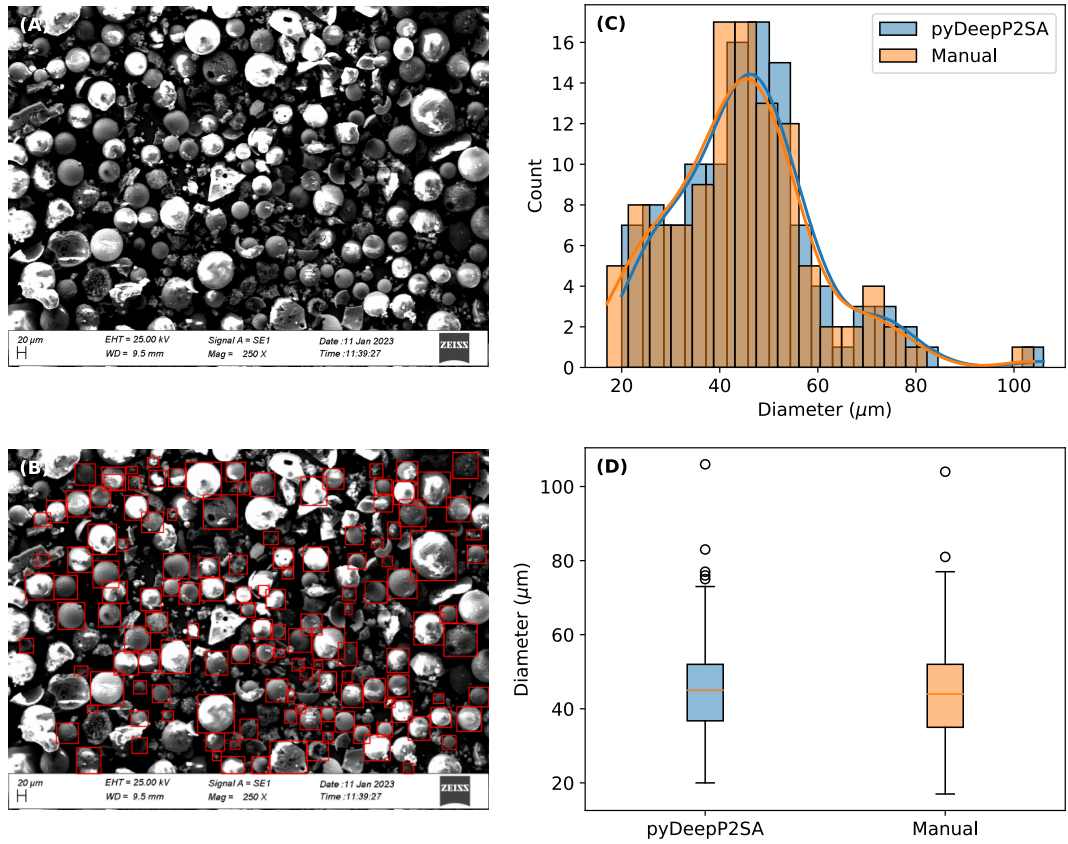
Figure 6.2: *(A) Input SEM-SE image (B) Segmented spheres indicated by the bounding boxes. (C) PSD obtained using the developed pyDeepP2SA package compared with manual measurements using ImageJ Fiji. (D) Box plots for the measured diameter distribution.*

segments), 112 were identified as individual spheres, whereas 26 segments were composites of smaller and larger spheres, irregular CFA particles, or segments containing more than two spheres. It should be noted that 81.16% of the segmentation results were deemed valid, with the potential for improvement through fine-tuning the default model parameters. Figure 6.2 C illustrates the PSD obtained from both package and manual measurements. Furthermore, Figure 6.2 D shows the statistical distribution of the particle diameters captured by both methods. Statistical analysis of the two methods revealed a mean difference of 1.4 μm between the two measurement methods, which is relatively small considering the pixel size of the input image, that is, 1 μm. Furthermore, the statistical measures, including the MAE of 1.54 μm, root mean square error (RMSE) of 2.03 μm, and coefficient of determination (R-squared) of 0.99, indicate a high level of accuracy and strong correlation. The non-parametric Mann–Whitney U test was employed to compare the distributions of *pyDeepP2SA* and manual measurements. The test results revealed no significant differences in the distributions of the two measurement methods (p-value= 0.45). In conclusion, these

findings suggest that *pyDeepP2SA* effectively approximates the values obtained from manual measurements. Thus, the developed package serves the purpose of rapidly assessing the physical properties related to particle size and shapes of the SEM images.

6.3 pyDeepP2SA package and the "line_scan" function for cenosphere and solid sphere characterisation
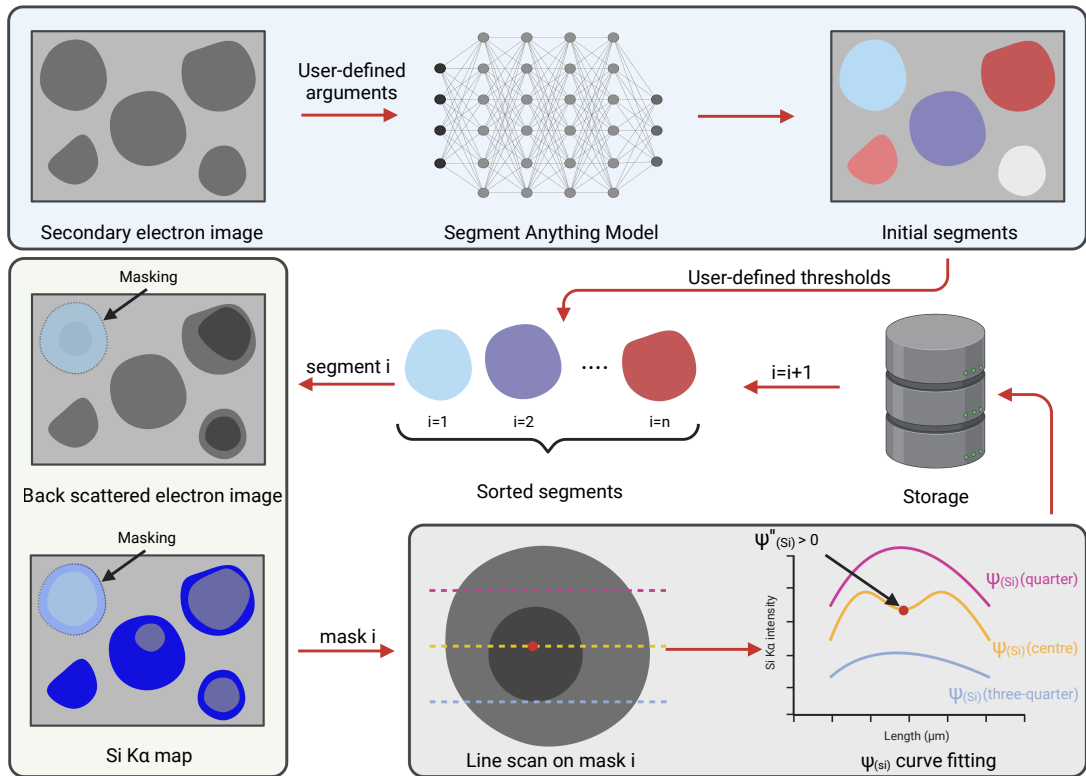
Figure 6.3: *Overview of the classification process utilising the SEM-SE image and SEM-BSE image or Si Kα map and numerical computations.*

Hundreds or even thousands of spherical particles were captured in a single SEM image. Manually assessing each of these particles through line scans is labourious and time-consuming. Therefore, automating the process of line scans through these particles and classifying them based on their $\psi_{Si}^{''}$ profiles is crucial for effective analysis. To address this issue, pyDeepP2SA, a scientific computing Python package was developed specifically designed for assessing particle properties in scientific images, ranging from SEM images to computed tomography (CT) images. pyDeepP2SA is an open-source project available on PyPI as a module (Kanesalingam, 2023). This package leverages the SAM from Meta AI research for zero-generalisation segmentation of spheres (Kirillov et al., 2023). Notably, this state-of-the-art deep learning model eliminates the requirement for training data for

segmentation, which is a significant advantage given the limited availability of cenosphere data. Within pyDeepP2SA, a function called "line_scan" was designed to facilitate the characterisation of cenospheres and solid spheres from unlabelled data. This function takes as input an SEM-SE image, a corresponding SEM-BSE image, or a Si Kα map, along with various arguments such as circularity threshold, minimum area, image scale, and SAM parameters for hyperparameter optimisation.
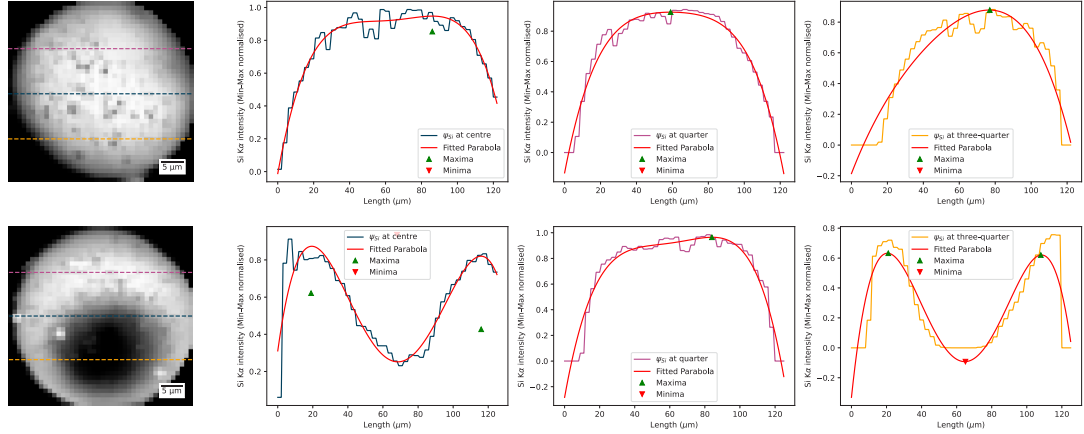
Figure 6.4: *(A) Selected segment representing the cenosphere. (B), (C), and (D) show the ψ_{Si} at the centre, quarter, and three-quarters of the segmented cenosphere. (E) Selected segment representing the solid sphere. (F), (G), and (H) display ψ_{Si} at the centre, quarter, and three-quarters of the segmented solid sphere.*

An overview of the **"line_scan"** function architecture is shown in Figure 6.3. The function analyses segmented spheres that meet the circularity threshold and minimum area criteria. It performs line scans with a user-defined spacing, which influences the accuracy of void detection in the process. The resulting lines are then fitted to a quartic function ($f(x) = a_4x^4 + a_3x^3 + a_2x^2 + a_1x + a_0$). This approach was chosen because solid spheres exhibit a definitive maximum (i.e., $\psi_{Si}^{''} < 0$), whereas cenospheres exhibit at least one minimum (i.e., $\psi_{Si}^{''} > 0$) (as discussed in Section 5.6). Based on the assessment of all scanned quartic functions, pyDeepP2SA classified each segmented sphere as either a cenosphere or a solid sphere. If any of the line scans indicated the presence of a minimum, the corresponding sphere was classified as a cenosphere. The confidence of this classification is expressed through the error value, specifically, the RMSE calculated during curve fitting. After the classification, users can further employ functions, such as **"plot_segment_bounding_boxes"**, **"plot_spheres"**, and **"box_plots_spheres"**, within pyDeepP2SA to conduct individual distribution analysis of the two types of spheres, as well as shape and size analysis of the particles.

To assess the performance of the **"line_scan"** function, an SEM-SE image was used, along with its corresponding SEM-BSE image. The circularity threshold was set to

0.85 and a minimum area of 50 μm. The SAM model parameters were set to their default settings. Figure 6.4 A displays a SEM-BSE image segment obtained after applying the SAM, revealing distinctive features within the spherical CFA particle. The **"line_scan"** function is then employed to traverse the segmented sphere. Figure 6.4 B, C, and D display the ψ_{Si} profiles at the centre (dark blue), quarter (pink), and three-quarter (pale orange) of the segmented sphere, respectively. Each ψ_{Si} profile was fitted to a quartic function (indicated by the red line segments), allowing the assessment of the presence of a minimum. In this segment, both the centre and three-quarters exhibit concave-up profiles, indicating $\psi_{Si}^{''} > 0$ and confirming that the scanned sphere is a cenosphere, with a mean RMSE of 0.23. Conversely, Figure 6.4 E illustrates a distinct sphere devoid of any internal anomalies. The concave-down profiles, where $\psi_{Si}^{''} < 0$, further validate this observation, with a mean RMSE of 0.09. However, it is important to note that the current assessment is constrained by the limitations inherent to SEM-BSE images. By contrast, the classification accuracy can be substantially enhanced by leveraging the Si Kα maps obtained through EDS.

CHAPTER 7

CONCLUSIONS AND RECOMMENDATIONS

7.1 Conclusions

Understanding and characterising CFA stands as a pivotal endeavour in unravelling the vast opportunities hidden within this versatile heterogeneous material. Despite its potential, the extraction of multiple value-added materials often remains overlooked due to limited comprehension of their physical and chemical properties. This study aimed to assess the potential of two CFA derivatives—zeolites and cenospheres through a pre-processing technique known as the washing cycle. Various analytical methods including microscopy, spectroscopy, DIP, and deep learning were employed to comprehensively evaluate these derivatives.

The process of the washing cycle which was initially introduced by Pannilarathne et al. (2021) and expanded by Brinthan et al. (2022), is extensively examined in Chapter 4. The formation of a floating layer during the settling period showcased the accumulation of particles near the solution's surface due to inter-particle forces, particularly van der Waals forces. The presence of valuable cenospheres within this floating layer, primarily composed of oxides of Si and Al, highlighted their potential for recovery through pond skimming or electrostatic separation. However, the challenge lies in their purity due to the presence of Ca crystals. The decrease in solution pH and conductivity with increasing washing cycles unveiled a diminishing dissolution pattern of readily soluble ions in raw CFA. Meanwhile, the evaluation of the bottom layer revealed the settling of washed CFA particles. Stirring facilitated the dissolution of surface ions, enhancing subsequent processing by exposing the CFA core. However, the non-linear behaviour in Sauter mean diameter signifies the potential segregation of CFA particles, complicating downstream processes like zeolite synthesis or critical element extraction. These findings underscore the complex interplay of temperature, particle characteristics, and chemical reactions during washing cycles. They offer crucial insights into strategies for cenosphere recovery, purification challenges, and the impact of washing on CFA properties, contributing significantly to the understanding and potential optimisation of CFA utilisation processes. Yet, compared to other pre-processing techniques, such as flotation, magnetic separation, or grinding, the washing cycle maximises component utilisation within CFA, fostering circular economic approaches to end products.

The novelty of this study lies in the insights gathered from the comprehensive assessment of cenospheres, zeolites, and the substrate for element extraction, which

resulted from post-processing the components segregated during the washing cycle process. Below are the main conclusions drawn from this study.

The PSD of the particles within the floating layer from the washing cycle process was calculated using the different magnification levels of the SEM-SE images, revealing the mean diameter to the combined statistical distribution as 176.66 μm and a SD of 36.65 μm. Notably, this study unveiled the coexistence of solid spheres alongside cenospheres in the floating layer while examining through the BSE imaging technique. Assessment of high magnification SEM-SE and -BSE images through the newly developed *pyDeepP2SA* showed mean diameters of 55.71 μm for solid spheres and 45.40 μm for cenospheres in the floating layer. The Otsu thresholding method demonstrated a high correlation (0.986) with manually assessed threshold values for void identification in BSE images at different accelerating voltages (10, 15, 20, and 25 keV). The minimum accelerating voltage required for SEM to identify voids in CFA particles through BSE imaging was found to be between 12-15 keV for the selected cenosphere. The varying thickness of the cenosphere's cell wall creates interesting research questions in establishing a generalised relationship between diameter and cell wall thickness. Nevertheless, a generalised relationship was derived which applies to cenospheres with diameters greater than 30 μm.

The simple line scan method in EDS (specifically ψ_{Si} profiles) offers a reliable means of classifying CFA particles as either cenospheres or solid spheres compared to the SEM-BSE technique. The characterisation threshold for a given accelerating voltage can be reasonably approximated as half the penetration depth at a 99% X-ray intensity level. The introduced ψ_{Si} profiles provide a non-invasive approach to determining the cell wall thickness of cenospheres. At lower accelerating voltages, a correction of half the radial resolution (at a 99% X-ray intensity level) is necessary to accurately assess the cell wall thickness, while at higher voltages, direct measurements can be made. Thus, it is essential to evaluate the cell wall thickness using multiple accelerating voltages for a comprehensive understanding. This study represents the inaugural comprehensive exploration of employing EDS and X-ray microanalysis for characterising imperceptible microstructures within particles.

Furthermore, the zeolite synthesised using the bottom layer through a two-step alkaline fusion process produced multiple zeolite types that can act as molecular sieves. Additionally, the bottom sample contained major elements such as Si, Al, Fe, and Ti, along with multiple other trace elements and REEs, warranting consideration for further extraction.

Moreover, the development of the *pyDeepP2SA* Python package marks a significant step in automating the analysis of particle properties in SEM images. Leveraging a deep learning model, this package enables rapid assessment of particle shape and size

distributions, simplifying intensive coding processes and facilitating accessibility for researchers with varying levels of programming expertise. *pyDeepP2SA* achieved an accuracy of 81.16% for the segmentation of spheres and effectively approximated particle diameter values when compared with manual measurements, showing a mean difference of 1.4 μm., showcases its potential in rapidly assessing physical properties related to particle size and shapes in SEM images. Furthermore, within the *pyDeepP2SA* package, the "line_scan" function offers a means to automate line scans and classify particles based on their profiles, particularly distinguishing between cenospheres and solid spheres. This function utilises quartic function fitting to discern the nature of particles, providing a way to automate the laborious process of individual particle assessment. This approach not only addresses existing challenges but also paves the way for further improvements in particle analysis methodologies.

7.2 Limitations

This study did not analyse the properties of CFA based on their parent coal properties, which are heavily influenced by geological factors. Furthermore, the properties of CFA can vary significantly based on the combustion conditions at the power plant, which were not assessed in this study. Additionally, the representative samples of CFA collected from the power plant were obtained through convenience sampling, potentially introducing discrepancies in the washing cycle process.

The washing cycle method utilised in this study requires further comprehensive evaluation regarding its susceptibility to external variables such as temperature, atmospheric exposure, and pressure. Despite providing a detailed examination of the washing cycle process, this study falls short in fully investigating the impacts of temperature and atmospheric conditions. Additionally, the separation process was confined to a small-scale open laboratory environment, lacking an assessment of scalability and associated challenges. Thermodynamic considerations during the separation process were overlooked, as were the kinetics of CFA and the thermodynamics of the system.

In the characterisation studies, data beyond 25 keV were simulated to draw generalised conclusions, yet these findings require validation through experimental data. The ionisation effect of electron microscopy and the influence of wavelength in EDS characterisation were not evaluated, highlighting the need for careful consideration of these factors in the further studies.

7.3 Recommendations

Exploring the dissolution behaviour of CFA within the washing cycle warrants attention, specifically through the quantification of the amorphous content in the bottom layer and the assessment of elemental concentrations in the washed solution. This approach holds promise for enhancing our comprehension of the scaling-up process. Moreover, substituting deionised water with saltwater or reservoir water could be investigated to scrutinise the washing cycle's characteristics and performance while eliminating the economic burden associated with acquiring deionised water. Additionally, a hybrid washing cycle method involving centrifugation, stirring, and settling could be considered, enabling the segregation of coarse and fine CFA during centrifugation and the subsequent recovery of other components like cenospheres during the stirring and settling phases.

While multi-modal imaging techniques like SEM-SE, SEM-BSE, and EDS have provided a novel and resource-efficient means of X-ray microanalysis for characterising cenospheres, employing transmission electron microscopy, X-ray micro-computed tomography, and synchrotron-based techniques would serve to validate and enhance the proposed line scan technique. This multi-modal approach would deepen our understanding not only of cenospheres but also of coexisting spheres such as ferrospheres (ferrous-rich particles) and plerospheres (contain several smaller spherical particles within them) within the floating layer. Furthermore, an extensive investigation into the mechanical properties of cenospheres and their responses to diverse environmental conditions is warranted. Exploring matrix modification and functionalisation of cenospheres could potentially yield high-end materials suitable for industrial production.

Another focal point is the exploration of zeolites. Following successful synthesis, delving into their adsorption capabilities in the presence of single and multiple cation solutions is imperative. The functionalisation of zeolites for the selective adsorption of specific heavy metals and dyes warrants exploration. Detailed microscale characterisation of pore structures and their stability is also essential. Additionally, investigating the incorporation of cenospheres during zeolite synthesis to create pores of varying sizes could open up possibilities for specialised adsorption tests.

The standout features of this research lie in its simulation, modelling, and the DIP aspects pertaining to cenospheres. Incorporating the automatic retrieval of cell wall thickness of these cenospheres into the developed *pyDeepP2SA* package marks a significant advancement. Additionally, including pre-processing methods like filtering, noise reduction, and morphological operations to improve unclear input images would greatly enhance the utility of the package. Moreover, refining the segmentation accuracy by training a custom dataset consisting of cenospheres and

solid spheres on the same model architecture with pretrained weights holds promise. An exciting prospect stemming from the EDS line scan lies in the potential for 3D reconstruction of these spheres utilising the EDS line scan data.

The proposed avenues for further research offer promising opportunities for refining processes, enhancing material properties, and utilising innovative techniques for comprehensive analysis. By delving deeper into these areas, future investigations can unlock new horizons for sustainable and efficient practices, paving the way for impactful advancements in both academia and industry.

REFERENCES

Abdellaoui, Y., Abou Oualid, H., Hsini, A., El Ibrahimi, B., Laabd, M., El Ouardi, M., Giacoman-Vallejos, G., and Gamero-Melo, P. (2021). Synthesis of zirconium-modified merlinoite from fly ash for enhanced removal of phosphate in aqueous medium: Experimental studies supported by monte carlo/sa simulations. *Chemical Engineering Journal*, 404:126600.

Ahmaruzzaman, M. (2010). A review on the utilization of fly ash. *Progress in energy and combustion science*, 36(3):327–363.

Alberich, J. P., Pansera, M., and Hartley, S. (2022). Understanding the eu's circular economy policies through futures of circularity. *Journal of Cleaner Production*, page 135723.

Amoni, B. C., Freitas, A. D., Bessa, R. A., Oliveira, C. P., Bastos-Neto, M., Azevedo, D. C., Lucena, S. M., Sasaki, J. M., Soares, J. B., Soares, S. A., et al. (2022). Effect of coal fly ash treatments on synthesis of high-quality zeolite a as a potential additive for warm mix asphalt. *Materials Chemistry and Physics*, 275:125197.

Anshits, N., Mikhailova, O., Salanov, A., and Anshits, A. (2010). Chemical composition and structure of the shell of fly ash non-perforated cenospheres produced from the combustion of the kuznetsk coal (russia). *Fuel*, 89(8):1849–1862.

Anshits, N., Vereshchagina, T., Fomenko, E., Anshits, A., Kruchek, D., Paretskov, E., Bajukov, O., Kyrenskii, L., and Zykova, I. (2005). Coal fly ash cenospheres and their application for immobilization of liquid radioactive waste. In *Proceedings-10th International Conference on Environmental Remediation and Radioactive Waste Management, ICEM'05*, pages 1124–1131.

Asokan, P., Saxena, M., and Asolekar, S. R. (2005). Coal combustion residues—environmental implications and recycling potentials. *Resources, Conservation and recycling*, 43(3):239–262.

Babla, M., Katwal, U., Yong, M.-T., Jahandari, S., Rahme, M., Chen, Z.-H., and Tao, Z. (2022). Value-added products as soil conditioners for sustainable agriculture. *Resources, Conservation and Recycling*, 178:106079.

Basu, M., Pande, M., Bhadoria, P., and Mahapatra, S. (2009). Potential fly-ash utilization in agriculture: a global review. *Progress in natural science*, 19(10):1173–1186.

Belviso, C., Cavalcante, F., Di Gennaro, S., Palma, A., Ragone, P., and Fiore, S. (2015). Mobility of trace elements in fly ash and in zeolitised coal fly ash. *Fuel*, 144:369–379.

Blissett, R. and Rowson, N. (2012). A review of the multi-component utilisation of coal fly ash. *Fuel*, 97:1–23.

Brinthan, K., Shivadhahini, S., Senadheera, U., Fernando, W., Jayawardena, C., Jayasundara, D., and Wickrama, M. (2022). Experimental investigation and performance optimisation of washing cycles for pre-processing of coal fly ash.

Brooks, A. L., Shen, Z., and Zhou, H. (2020). Development of a high-temperature inorganic synthetic foam with recycled fly-ash cenospheres for thermal insulation brick manufacturing. *Journal of cleaner production*, 246:118748.

Calzolai, L., Gilliland, D., and Rossi, F. (2012). Measuring nanoparticles size distribution in food and consumer products: a review. *Food Additives & Contaminants: Part A*, 29(8):1183–1193.

Cao, M., Zhao, L., Xu, D., Parsley, D., Ciora, R., Liu, P. K., Manousiouthakis, V. I., and Tsotsis, T. T. (2021). A reactive separation process for pre-combustion co2 capture employing oxygen-blown coal gasifier off-gas. *Chemical Engineering Journal*, 420:127694.

Cardoso, A. M., Horn, M. B., Ferret, L. S., Azevedo, C. M., and Pires, M. (2015). Integrated synthesis of zeolites 4a and na–p1 using coal fly ash for application in the formulation of detergents and swine wastewater treatment. *Journal of Hazardous Materials*, 287:69–77.

Chai, W. S., Cheun, J. Y., Kumar, P. S., Mubashir, M., Majeed, Z., Banat, F., Ho, S.-H., and Show, P. L. (2021). A review on conventional and novel materials towards heavy metal adsorption in wastewater treatment application. *Journal of Cleaner Production*, page 126589.

Chen, H., Zhang, L., Pan, J., Long, X., He, X., and Zhou, C. (2022a). Study on modes of occurrence and enhanced leaching of critical metals (lithium, niobium, and rare earth elements) in coal gangue. *Journal of Environmental Chemical Engineering*, 10(6):108818.

Chen, J., Yang, R., Zhang, Z., and Wu, D. (2022b). Removal of fluoride from water using aluminum hydroxide-loaded zeolite synthesized from coal fly ash. *Journal of Hazardous Materials*, 421:126817.

Chen, Q., Chen, L., Li, J., Guo, Y., Wang, Y., Wei, W., Liu, C., Wu, J., Tou, F., Wang, X., et al. (2022c). Increasing mercury risk of fly ash generated from coal-fired power plants in china. *Journal of Hazardous Materials*, 429:128296.

Cui, R. Y., Hultman, N., Edwards, M. R., He, L., Sen, A., Surana, K., McJeon, H., Iyer, G., Patel, P., Yu, S., et al. (2019). Quantifying operational lifetimes for coal power plants under the paris goals. *Nature communications*, 10(1):1–9.

Curpen, S., Teutsch, N., Kovler, K., and Spatari, S. (2022). Evaluating life cycle environmental impacts of coal fly ash utilization in embankment versus sand and landfilling. *Journal of Cleaner Production*, page 135402.

Czarna-Juszkiewicz, D., Cader, J., and Wdowin, M. (2020). From coal ashes to solid sorbents for hydrogen storage. *Journal of Cleaner Production*, 270:122355.

Danish, A. and Mosaberpanah, M. A. (2020). Formation mechanism and applications of cenospheres: a review. *Journal of Materials Science*, 55(11):4539–4557.

Demers, H., Poirier-Demers, N., Couture, A. R., Joly, D., Guilmain, M., de Jonge, N., and Drouin, D. (2011). Three-dimensional electron microscopy simulation with the casino monte carlo software. *Scanning*, 33(3):135–146.

Deng, B., Wang, X., Luong, D. X., Carter, R. A., Wang, Z., Tomson, M. B., and Tour, J. M. (2022). Rare earth elements from waste. *Science Advances*, 8(6):eabm3132.

Dev, S., Sachan, A., Dehghani, F., Ghosh, T., Briggs, B. R., and Aggarwal, S. (2020). Mechanisms of biological recovery of rare-earth elements from industrial and electronic wastes: A review. *Chemical Engineering Journal*, 397:124596.

Donovan, J., Pinard, P., and Demers, H. (2019). High speed matrix corrections for quantitative x-ray microanalysis based on monte carlo simulated k-ratio intensities. *Microscopy and Microanalysis*, 25(3):735–742.

Dos Santos, L. C. T., Giannetti, B. F., Agostinho, F., Liu, G., and Almeida, C. M. (2023). A multi-criteria approach to assess interconnections among the environmental, economic, and social dimensions of circular economy. *Journal of Environmental Management*, 342:118317.

Drouin, D., Couture, A. R., Joly, D., Tastet, X., Aimez, V., and Gauvin, R. (2007). Casino v2. 42—a fast and easy-to-use modeling tool for scanning electron microscopy and microanalysis users. *Scanning: The Journal of Scanning Microscopies*, 29(3):92–101.

Du, J., Liu, Z., Christodoulatos, C., Conway, M., Bao, Y., and Meng, W. (2022). Utilization of off-specification fly ash in preparing ultra-high-performance concrete (uhpc): Mixture design, characterization, and life-cycle assessment. *Resources, Conservation and Recycling*, 180:106136.

Eze, C. P., Nyale, S. M., Akinyeye, R. O., Gitari, W. M., Akinyemi, S. A., Fatoba, O. O., and Petrik, L. F. (2013). Chemical, mineralogical and morphological changes in weathered coal fly ash: A case study of a brine impacted wet ash dump. *Journal of environmental management*, 129:479–492.

Fan, X.-l., Lv, S.-q., Xia, J.-l., Nie, Z.-y., Zhang, D.-r., Pan, X., Liu, L.-z., Wen, W., Zheng, L., and Zhao, Y.-d. (2019). Extraction of al and ce from coal fly ash by biogenic fe3+ and h2so4. *Chemical Engineering Journal*, 370:1407–1424.

Fan, Y., Huang, R., Liu, Q., Cao, Q., and Guo, R. (2023). Synthesis of zeolite a from fly ash and its application in the slow release of urea. *Waste Management*, 158:47–55.

Fomenko, E., Anshits, N., Vasil'Eva, N., Rogovenko, E., Mikhaylova, O., Mazurova, E., Solovyev, L., and Anshits, A. (2016). Composition and structure of the shells of aluminosilicate microspheres in fly ash formed on the combustion of ekibastuz coal. *Solid Fuel Chemistry*, 50:238–247.

Fomenko, E. V., Anshits, N. N., Solovyov, L. A., Mikhaylova, O. A., and Anshits, A. G. (2013). Composition and morphology of fly ash cenospheres produced from the combustion of kuznetsk coal. *Energy & fuels*, 27(9):5440–5448.

Fomenko, E. V., Anshits, N. N., Vasilieva, N. G., Mikhaylova, O. A., Rogovenko, E. S., Zhizhaev, A. M., and Anshits, A. G. (2015). Characterization of fly ash cenospheres produced from the combustion of ekibastuz coal. *Energy & Fuels*, 29(8):5390–5403.

Fournelle, J., Cathey, H., Pinard, P. T., and Richter, S. (2016). Low voltage epma: experiments on a new frontier in microanalysis-analytical lateral resolution. In *IOP Conference Series: Materials Science and Engineering*, volume 109, page 012003. IOP Publishing.

Franus, W., Wiatros-Motyka, M. M., and Wdowin, M. (2015). Coal fly ash as a resource for rare earth elements. *Environmental Science and Pollution Research*, 22(12):9464–9474.

Gadore, V. and Ahmaruzzaman, M. (2021). Tailored fly ash materials: A recent progress of their properties and applications for remediation of organic and inorganic contaminants from water. *Journal of Water Process Engineering*, 41:101910.

Gao, S., Peng, H., Song, B., Zhang, J., Wu, W., Vaughan, J., Zardo, P., Vogrin, J., Tulloch, S., and Zhu, Z. (2022). Synthesis of zeolite from low-cost feeds and its sustainable environmental applications. *Journal of Environmental Chemical Engineering*, page 108995.

Gaustad, G., Williams, E., and Leader, A. (2021). Rare earth metals from secondary sources: Review of potential supply from waste and byproducts. *Resources, Conservation and Recycling*, 167:105213.

Gauvin, R. and Michaud, P. (2009). Mc x-ray, a new monte carlo program for quantitative x-ray microanalysis of real materials. *Microscopy and Microanalysis*, 15(S2):488–489.

Ge, J. C., Yoon, S. K., and Choi, N. J. (2018). Application of fly ash as an adsorbent for removal of air and water pollutants. *Applied Sciences*, 8(7):1116.

Geisendorf, S. and Pietrulla, F. (2018). The circular economy and circular economic concepts—a literature analysis and redefinition. *Thunderbird International Business Review*, 60(5):771–782.

Ghosh, S. K. and Kumar, V. (2020). *Circular economy and fly ash management*. Springer.

Gimhan, P., Nasvi, M., and Disanayaka, J. (2018). Geotechnical engineering properties of fly ash and bottom ash: use as civil engineering construction material.

Grela, A., Kuc, J., and Bajda, T. (2021). A review on the application of zeolites and mesoporous silica materials in the removal of non-steroidal anti-inflammatory drugs and antibiotics from water. *Materials*, 14(17):4994.

Hagemeyer, A. N., Sears, C. G., and Zierold, K. M. (2019). Respiratory health in adults residing near a coal-burning power plant with coal ash storage facilities: a cross-sectional epidemiological study. *International Journal of Environmental Research and Public Health*, 16(19):3642.

He, S., Bao, R., Li, J., Grant, P. E., and Ou, Y. (2023). Accuracy of segment-anything model (sam) in medical image segmentation tasks. *arXiv preprint arXiv:2304.09324*.

He, X., Xu, W., Sun, W., and Ni, J. (2013). Phosphate removal using compounds prepared from paper sludge and fly ash. *Environmental earth sciences*, 70:615–623.

Hidayat, A. E., Moersidik, S. S., and Adityosulindro, S. (2021). Adsorption and desorption of zinc and copper in acid mine drainage onto synthesized zeolite from

coal fly ash. In *Journal of Physics: Conference Series*, volume 1811, page 012045. IOP Publishing.

Ho, H.-J., Iizuka, A., Shibata, E., and Ojumu, T. (2022). Circular indirect carbonation of coal fly ash for carbon dioxide capture and utilization. *Journal of Environmental Chemical Engineering*, 10(5):108269.

Höller, H., Wirsching, U., and Fakhuri, M. (1974). Experimente zur zeolithbildung durch hydrothermale umwandlung. *Contributions to Mineralogy and Petrology*, 46(1):49–60.

Hong, J. L. X., Maneerung, T., Koh, S. N., Kawi, S., and Wang, C.-H. (2017). Conversion of coal fly ash into zeolite materials: synthesis and characterizations, process design, and its cost-benefit analysis. *Industrial & Engineering Chemistry Research*, 56(40):11565–11574.

Hoskins, B. D., Adam, G. C., Strelcov, E., Zhitenev, N., Kolmakov, A., Strukov, D. B., and McClelland, J. J. (2017). Stateful characterization of resistive switching tio2 with electron beam induced currents. *Nature communications*, 8(1):1972.

Hua, Y., Zhao, X., and Sun, W. (2023). Estimation of anthropogenic co2 emissions at different scales for assessing sdg indicators: Method and application. *Journal of Cleaner Production*, page 137547.

IEA (2022). Global coal consumption, 2020-2023.

International Organization for Standardization (2013). Microbeam analysis — electron probe microanalysis (epma) — vocabulary. ISO 23833:2013(en).

Iqbal, A., Sattar, H., Haider, R., and Munir, S. (2019). Synthesis and characterization of pure phase zeolite 4a from coal fly ash. *Journal of Cleaner Production*, 219:258–267.

Itskos, G., Itskos, S., and Koukouzas, N. (2010a). Size fraction characterization of highly-calcareous fly ash. *Fuel Processing Technology*, 91(11):1558–1563.

Itskos, G., Koukouzas, N., Vasilatos, C., Megremi, I., and Moutsatsou, A. (2010b). Comparative uptake study of toxic elements from aqueous media by the different particle-size-fractions of fly ash. *Journal of hazardous materials*, 183(1-3):787–792.

Iyer, R. (2002). The surface chemistry of leaching coal fly ash. *Journal of hazardous materials*, 93(3):321–329.

Jala, S. and Goyal, D. (2006). Fly ash as a soil ameliorant for improving crop production—a review. *Bioresource technology*, 97(9):1136–1147.

Ji, W., Li, J., Bi, Q., Li, W., and Cheng, L. (2023). Segment anything is not always perfect: An investigation of sam on different real-world applications. *arXiv preprint arXiv:2304.05750*.

Jiang, T., Wang, P., Zhang, T., Zhu, D., and Liu, Z. (2022). A novel solvent extraction system to recover germanium from h2so4 leaching liquor of secondary zinc oxide: Extraction behavior and mechanism. *Journal of Cleaner Production*, page 135399.

Joseph, I. V., Tosheva, L., and Doyle, A. M. (2020). Simultaneous removal of cd (ii), co (ii), cu (ii), pb (ii), and zn (ii) ions from aqueous solutions via adsorption on fau-type zeolites prepared from coal fly ash. *Journal of Environmental Chemical Engineering*, 8(4):103895.

Joy, D. and Luo, S. (1989). An empirical stopping power relationship for low-energy electrons. *Scanning*, 11(4):176–180.

Ju, T., Han, S., Meng, Y., and Jiang, J. (2021). High-end reclamation of coal fly ash focusing on elemental extraction and synthesis of porous materials. *ACS Sustainable Chemistry & Engineering*, 9(20):6894–6911.

Kaboli, S., Noel, P., Clément, D., Demers, H., Paolella, A., Bouchard, P., Trudeau, M. L., Goodenough, J. B., and Zaghib, K. (2020). On high-temperature evolution of passivation layer in li–10 wt% mg alloy via in situ sem-ebsd. *Science Advances*, 6(50):eabd5708.

Kanesalingam, B. (2023). pydeepp2sa. https://github.com/BrinthanK/pyDeepP2SA. Accessed on 2023-08-29.

Kanesalingam, B., Fernando, W. A. M., Panda, S., Jayawardena, C., Attygalle, D., and Amarasinghe, D. (2023). Harnessing the capabilities of microorganisms for the valorisation of coal fly ash waste through biometallurgy. *Minerals*, 13(6):724.

Kanniche, M., Le Moullec, Y., Authier, O., Hagi, H., Bontemps, D., Neveux, T., and Louis-Louisy, M. (2017). Up-to-date co2 capture in thermal power plants. *Energy Procedia*, 114:95–103.

Karakasi, O. and Moutsatsou, A. (2010). Surface modification of high calcium fly ash for its application in oil spill clean up. *Fuel*, 89(12):3966–3970.

Khan, S., Naushad, M., Govarthanan, M., Iqbal, J., and Alfadul, S. M. (2022). Emerging contaminants of high concern for the environment: Current trends and future research. *Environmental Research*, 207:112609.

Kim, A. G., Kazonich, G., and Dahlberg, M. (2003). Relative solubility of cations in class f fly ash. *Environmental Science & Technology*, 37(19):4507–4511.

Kim, J.-H., Pudasainee, D., Yoon, Y.-S., Son, S.-U., and Seo, Y.-C. (2010). Studies on speciation changes and mass distribution of mercury in a bituminous coal-fired power plant by combining field data and chemical equilibrium calculation. *Industrial & Engineering Chemistry Research*, 49(11):5197–5203.

Kirchherr, J., Reike, D., and Hekkert, M. (2017). Conceptualizing the circular economy: An analysis of 114 definitions. *Resources, conservation and recycling*, 127:221–232.

Kirillov, A., Mintun, E., Ravi, N., Mao, H., Rolland, C., Gustafson, L., Xiao, T., Whitehead, S., Berg, A. C., Lo, W.-Y., et al. (2023). Segment anything. *arXiv preprint arXiv:2304.02643*.

Koshy, N. and Singh, D. (2016). Fly ash zeolites for water treatment applications. *Journal of Environmental Chemical Engineering*, 4(2):1460–1472.

Kowalczuk, P. B. and Drzymala, J. (2016). Physical meaning of the sauter mean diameter of spherical particulate matter. *Particulate Science and Technology*, 34(6):645–647.

Król, M. (2020). Natural vs. synthetic zeolites. *Crystals*, 10(7):622.

Kubota, Y., Sohn, J., Hatada, S., Schurr, M., Straehle, J., Gour, A., Neujahr, R., Miki, T., Mikula, S., and Kawaguchi, Y. (2018). A carbon nanotube tape for serial-section electron microscopy of brain ultrastructure. *Nature Communications*, 9(1):437.

Kula, I., Olgun, A., Sevinc, V., and Erdogan, Y. (2002). An investigation on the use of tincal ore waste, fly ash, and coal bottom ash as portland cement replacement materials. *Cement and Concrete Research*, 32(2):227–232.

Leslie, S. A. and Mitchell, J. C. (2007). Removing gold coating from sem samples. *palaeontology*, 50(6):1459–1461.

Li, J., Corma, A., and Yu, J. (2015). Synthesis of new zeolite structures. *Chemical Society Reviews*, 44(20):7112–7127.

Li, X., Bai, C., Qiao, Y., Wang, X., Yang, K., and Colombo, P. (2022). Preparation, properties and applications of fly ash-based porous geopolymers: A review. *Journal of Cleaner Production*, page 132043.

Lin, L., Meng, Y., Ju, T., Han, S., Meng, F., Li, J., Du, Y., Song, M., Lan, T., and Jiang, J. (2023). Characteristics, application and modeling of solid amine adsorbents for co2 capture: A review. *Journal of Environmental Management*, 325:116438.

Liu, Y., Chen, H., Mo, Q., Yang, X., Wang, J., Lin, X., Shang, D., Li, Y., and Zhang, Y. (2021). Removal of cadmium and tetracycline by lignin hydrogels loaded with nano-fes: Nanoparticle size control and content calculation. *Journal of Hazardous Materials*, 416:126262.

Llovet, X., Moy, A., Pinard, P. T., and Fournelle, J. H. (2021). Reprint of: Electron probe microanalysis: A review of recent developments and applications in materials science and engineering. *Progress in Materials Science*, 120:100818.

Lu, X., Liu, B., Zhang, Q., Wen, Q., Wang, S., Xiao, K., and Zhang, S. (2023). Recycling of coal fly ash in building materials: A review. *Minerals*, 13(1):25.

Lu, Z., Zhou, W., Huo, P., Luo, Y., He, M., Pan, J., Li, C., and Yan, Y. (2013). Performance of a novel tio2 photocatalyst based on the magnetic floating fly-ash cenospheres for the purpose of treating waste by waste. *Chemical Engineering Journal*, 225:34–42.

Ma, G. and Yue, X. (2022). An improved whale optimization algorithm based on multilevel threshold image segmentation using the otsu method. *Engineering Applications of Artificial Intelligence*, 113:104960.

Ma, J. and Wang, B. (2023). Segment anything in medical images. *arXiv preprint arXiv:2304.12306*.

Marinina, O., Nevskaya, M., Jonek-Kowalska, I., Wolniak, R., and Marinin, M. (2021). Recycling of coal fly ash as an example of an efficient circular economy: a stakeholder approach. *Energies*, 14(12):3597.

Markandeya, Shukla, S., and Dhiman, N. (2017). Characterization and adsorption of disperse dyes from wastewater onto cenospheres activated carbon composites. *Environmental Earth Sciences*, 76:1–12.

Markandeya, Shukla, S. P., and Srivastav, A. L. (2021). Removal of disperse orange and disperse blue dyes present in textile mill effluent using zeolite synthesized from cenospheres. *Water Science and Technology*, 84(2):445–457.

Martins, V. F., Miguel, C. V., Gonçalves, J. C., Rodrigues, A. E., and Madeira, L. M. (2022). Modeling of a cyclic sorption–desorption unit for continuous high temperature co2 capture from flue gas. *Chemical Engineering Journal*, 434:134704.

Mazzella, A., Errico, M., and Spiga, D. (2016). Co2 uptake capacity of coal fly ash: Influence of pressure and temperature on direct gas-solid carbonation. *Journal of Environmental Chemical Engineering*, 4(4):4120–4128.

Meer, I. and Nazir, R. (2018). Removal techniques for heavy metals from fly ash. *Journal of Material Cycles and Waste Management*, 20(2):703–722.

Menéndez, E., Álvaro, A., Hernández, M., and Parra, J. (2014). New methodology for assessing the environmental burden of cement mortars with partial replacement of coal bottom ash and fly ash. *Journal of environmental management*, 133:275–283.

Meng, Y., Zhang, Z., Yin, H., and Ma, T. (2018). Automatic detection of particle size distribution by image analysis based on local adaptive canny edge detection and modified circular hough transform. *Micron*, 106:34–41.

Mishra, M., Sahu, S. K., Mangaraj, P., and Beig, G. (2023). Assessment of hazardous radionuclide emission due to fly ash from fossil fuel combustion in industrial activities in india and its impact on public. *Journal of Environmental Management*, 328:116908.

Mohanty, J. K., Guru, S. R., Dash, P., and Pradhan, P. K. (2021). Fly ash management and condition monitoring of ash pond. *Earth Systems and Environment*, 5:445–457.

Mushtaq, F., Zahid, M., Bhatti, I. A., Nasir, S., and Hussain, T. (2019). Possible applications of coal fly ash in wastewater treatment. *Journal of environmental management*, 240:27–46.

Nagao, Y., Yoshii, K., Yoshida, Y., and Hashimoto, Y. (2023). Characterization of trace elements in coal fly ash by extraction, micro-pixe, tof-sims, and xafs. *Waste Management*, 157:18–24.

Neupane, G. and Donahoe, R. J. (2012). Attenuation of trace elements in coal fly ash leachates by surfactant-modified zeolite. *Journal of hazardous Materials*, 229:201–208.

Newsam, J., Jarman, R., and Jacobson, A. (1985). Structural characterisation of synthetic gallium mazzite. *Materials Research Bulletin*, 20(2):125–136.

Ngu, L.-n., Wu, H., and Zhang, D.-k. (2007). Characterization of ash cenospheres in fly ash from australian power stations. *Energy & Fuels*, 21(6):3437–3445.

Nihalani, S., Mishra, Y., and Meeruty, A. (2020). Handling and utilisation of fly ash from thermal power plants. In *Circular Economy and Fly Ash Management*, pages 1–11. Springer.

Pan, J., Zhang, L., Wen, Z., Nie, T., Zhang, N., and Zhou, C. (2023). The mechanism study on the integrated process of naoh treatment and citric acid leaching for rare earth elements recovery from coal fly ash. *Journal of Environmental Chemical Engineering*, 11(3):109921.

Pannilarathne, I., Sandaruwan, M., Mathissan, P., Jayawardena, C., and Fernando, W. (2021). Characterisation of coal fly ash for potential wastewater treatment opportunities.

Park, H., Wang, L., and Yun, J.-H. (2021). Coal beneficiation technology to reduce hazardous heavy metals in fly ash. *Journal of Hazardous Materials*, 416:125853.

Peng, X., Tu, Q., Zhang, Y., Jun, K., Shen, F., Ogunfunmi, T., Sun, Y., Tucker, M. C., Ceder, G., and Scott, M. C. (2023). Unraveling li growth kinetics in solid electrolytes due to electron beam charging. *Science Advances*, 9(17):eabq3285.

Petrus, H. T. B. M., Olvianas, M., Shafiyurrahman, M. F., Pratama, I. G. A. A. N., Jenie, S. N. A., Astuti, W., Nurpratama, M. I., Ekaputri, J. J., and Anggara, F. (2022). Circular economy of coal fly ash and silica geothermal for green geopolymer: Characteristic and kinetic study. *Gels*, 8(4):233.

Petrus, H. T. B. M., Olvianas, M., Suprapta, W., Setiawan, F. A., Prasetya, A., Anggara, F., et al. (2020). Cenospheres characterization from indonesian coal-fired power plant fly ash and their potential utilization. *Journal of Environmental Chemical Engineering*, 8(5):104116.

Pinard, P. T., Richter, S., Demers, H., and Gauvin, R. (2012). evaluation of monte carlo codes with experimental k-ratio of binary specimen for quantitative microanalysis. *Microsc Microanal*, 18:994–995.

Pradhan, R. (2021). Life cycle assessment and circular economy concepts for green materials. In *Applications of Advanced Green Materials*, pages 723–732. Elsevier.

Qin, L., Gao, X., and Li, Q. (2019). Influences of coal fly ash containing ammonium salts on properties of cement paste. *Journal of environmental management*, 249:109374.

Querol, X., Moreno, N., Umaña, J. t., Alastuey, A., Hernández, E., Lopez-Soler, A., and Plana, F. (2002). Synthesis of zeolites from coal fly ash: an overview. *International Journal of coal geology*, 50(1-4):413–423.

Rahmah, W., Kadja, G., Mahyuddin, M., Saputro, A., Dipojono, H., and Wenten, I. (2022). Small-pore zeolite and zeotype membranes for co2 capture and sequestration–a review. *Journal of Environmental Chemical Engineering*, page 108707.

Ram, L. C. and Masto, R. E. (2010). An appraisal of the potential use of fly ash for reclaiming coal mine spoil. *Journal of Environmental Management*, 91(3):603–617.

Ranjbar, N. and Kuenzel, C. (2017). Cenospheres: A review. *Fuel*, 207:1–12.

Rasheed, R., Javed, H., Rizwan, A., Sharif, F., Yasar, A., Tabinda, A. B., Ahmad, S. R., Wang, Y., and Su, Y. (2021). Life cycle assessment of a cleaner supercritical coal-fired power plant. *Journal of Cleaner Production*, 279:123869.

Romero-Hernández, O. and Romero, S. (2018). Maximizing the value of waste: From waste management to the circular economy. *Thunderbird International Business Review*, 60(5):757–764.

Roy, W. R., Thiery, R. G., Schuller, R. M., and Suloway, J. J. (1981). Coal fly ash: a review of the literature and proposed classification system with emphasis on environmental impacts. *Environmental geology no. 096*.

Rueden, C. T., Hiner, M. C., Evans III, E. L., Pinkert, M. A., Lucas, A. M., Carpenter, A. E., Cimini, B. A., and Eliceiri, K. W. (2022). Pyimagej: A library for integrating imagej and python. *Nature Methods*, 19(11):1326–1327.

Ruiz, A. Z., Brühwiler, D., Ban, T., and Calzaferri, G. (2005). Synthesis of zeolite l. tuning size and morphology. *Monatshefte für Chemie/Chemical Monthly*, 136:77–89.

Saghiri, M. A., Asgar, K., Lotfi, M., Karamifar, K., Saghiri, A. M., Neelakantan, P., Gutmann, J. L., and Sheibaninia, A. (2012). Back-scattered and secondary electron images of scanning electron microscopy in dentistry: a new method for surface analysis. *Acta Odontologica Scandinavica*, 70(6):603–609.

Sahoo, P. K., Soltani, S., and Wong, A. K. (1988). A survey of thresholding techniques. *Computer vision, graphics, and image processing*, 41(2):233–260.

Salvat, F. and Llovet, X. (2018). Monte carlo simulation and fundamental quantities. In *IOP Conference Series: Materials Science and Engineering*, volume 304, page 012014. IOP Publishing.

Schindelin, J., Arganda-Carreras, I., Frise, E., Kaynig, V., Longair, M., Pietzsch, T., Preibisch, S., Rueden, C., Saalfeld, S., Schmid, B., et al. (2012). Fiji: an open-source platform for biological-image analysis. *Nature methods*, 9(7):676–682.

Schöggl, J.-P., Stumpf, L., and Baumgartner, R. J. (2020). The narrative of sustainability and circular economy-a longitudinal review of two decades of research. *Resources, Conservation and Recycling*, 163:105073.

Shanthi, C., Porpatham, R. K., and Pappa, N. (2014). Image analysis for particle size distribution. *International Journal of Engineering and Technology*, 6(3):1340–1345.

Shende, D. Z., Wasewar, K. L., and Wadatkar, S. S. (2021). Target-specific applications of fly ash cenosphere as smart material. *Handbook of Nanomaterials and Nanocomposites for Energy and Environmental Applications*, pages 3349–3369.

Singh, A., Kar, A. K., Singh, D., Verma, R., Shraogi, N., Zehra, A., Gautam, K., Anbumani, S., Ghosh, D., and Patnaik, S. (2022a). ph-responsive eco-friendly chitosan modified cenosphere/alginate composite hydrogel beads as carrier for controlled release of imidacloprid towards sustainable pest control. *Chemical Engineering Journal*, 427:131215.

Singh, N., Agarwal, A., De, A., and Singh, P. (2022b). Coal fly ash: An emerging material for water remediation. *International Journal of Coal Science & Technology*, 9(1):1–32.

Sivalingam, S. and Sen, S. (2019). Valorization of coal fly ash into nanozeolite by sonication-assisted hydrothermal method. *Journal of environmental management*, 235:145–151.

Skjervold, V. T., Mondino, G., Riboldi, L., and Nord, L. O. (2023). Investigation of control strategies for adsorption-based co2 capture from a thermal power plant under variable load operation. *Energy*, 268:126728.

Smith, M. R. and Myers, S. S. (2018). Impact of anthropogenic co2 emissions on global human nutrition. *Nature Climate Change*, 8(9):834–839.

Song, J., Wang, X., Bu, Y., Wang, X., Zhang, J., Huang, J., Ma, R., and Zhao, J. (2017). Photocatalytic enhancement of floating photocatalyst: Layer-by-layer hybrid carbonized chitosan and fe-n-codoped tio2 on fly ash cenospheres. *Applied Surface Science*, 391:236–250.

Su, H., Lin, J., Chen, H., and Wang, Q. (2021). Production of a novel slow-release coal fly ash microbial fertilizer for restoration of mine vegetation. *Waste Management*, 124:185–194.

Sultana, S., Ahsan, S., Tanvir, S., Haque, N., Alam, F., and Yellishetty, M. (2021). Coal fly ash utilisation and environmental impact. In *Clean Coal Technologies*, pages 381–402. Springer.

Sun, J., Li, R., Wang, X., Zhao, C., Song, Q., Liu, F., Wang, Z., Liu, C., and Zhang, X. (2023). Marine oil spill remediation by candelilla wax modified coal fly ash cenospheres. *Chemosphere*, 330:138619.

Szerement, J., Szatanik-Kloc, A., Jarosz, R., Bajda, T., and Mierzwa-Hersztek, M. (2021). Contemporary applications of natural and synthetic zeolites from fly

ash in agriculture and environmental protection. *Journal of Cleaner Production*, 311:127461.

Tauanov, Z., Tsakiridis, P., Mikhalovsky, S., and Inglezakis, V. (2018). Synthetic coal fly ash-derived zeolites doped with silver nanoparticles for mercury (ii) removal from water. *Journal of environmental management*, 224:164–171.

Teixeira, E. R., Camões, A., Branco, F., Aguiar, J., and Fangueiro, R. (2019). Recycling of biomass and coal fly ash as cement replacement material and its effect on hydration and carbonation of concrete. *Waste Management*, 94:39–48.

Teng, L., Jin, X., Bu, Y., Ma, J., Liu, Q., Yang, J., Liu, W., and Yao, L. (2022). Facile and fast synthesis of cancrinite-type zeolite from coal fly ash by a novel hot stuffy route. *Journal of Environmental Chemical Engineering*, 10(5):108369.

Tiwari, M., Shukla, S., Mohan, D., Bhargava, D., and Kisku, G. (2015). Modified cenospheres as an adsorbent for the removal of disperse dyes. *Advances in Environmental Chemistry*, 2015.

Ugurlu, A. (2004). Leaching characteristics of fly ash. *Environmental geology*, 46(6):890–895.

Valeev, D., Kunilova, I., Alpatov, A., Varnavskaya, A., and Ju, D. (2019). Magnetite and carbon extraction from coal fly ash using magnetic separation and flotation methods. *Minerals*, 9(5):320.

Vassilev, S. V. and Vassileva, C. G. (2007). A new approach for the classification of coal fly ashes based on their origin, composition, properties, and behaviour. *Fuel*, 86(10-11):1490–1512.

Vereshchagina, T. A., Vereshchagin, S. N., Shishkina, N. N., Mikhaylova, O. A., Solovyov, L. A., and Anshits, A. G. (2013a). One-step fabrication of hollow aluminosilicate microspheres with a composite zeolite/glass crystalline shell. *Microporous and mesoporous materials*, 169:207–211.

Vereshchagina, T. A., Vereshchagin, S. N., Shishkina, N. N., Vasilieva, N. G., Solovyov, L. A., and Anshits, A. G. (2013b). Microsphere zeolite materials derived from coal fly ash cenospheres as precursors to mineral-like aluminosilicate hosts for 135,137 cs and 90sr. *Journal of Nuclear Materials*, 437(1-3):11–18.

Vilakazi, A. Q., Ndlovu, S., Chipise, L., and Shemi, A. (2022). The recycling of coal fly ash: A review on sustainable developments and economic considerations. *Sustainability*, 14(4):1958.

Visa, M. (2016). Synthesis and characterization of new zeolite materials obtained from fly ash for heavy metals removal in advanced wastewater treatment. *Powder Technology*, 294:338–347.

Visa, M. and Chelaru, A.-M. (2014). Hydrothermally modified fly ash for heavy metals and dyes removal in advanced wastewater treatment. *Applied Surface Science*, 303:14–22.

Wang, B., Song, Z., and Sun, L. (2021a). A review: Comparison of multi-air-pollutant removal by advanced oxidation processes–industrial implementation for catalytic oxidation processes. *Chemical Engineering Journal*, 409:128136.

Wang, C., Xu, G., Gu, X., Gao, Y., and Zhao, P. (2021b). High value-added applications of coal fly ash in the form of porous materials: a review. *Ceramics International*, 47(16):22302–22315.

Wang, N., Sun, X., Zhao, Q., and Wang, P. (2021c). Treatment of polymer-flooding wastewater by a modified coal fly ash-catalysed fenton-like process with microwave pre-enhancement: System parameters, kinetics, and proposed mechanism. *Chemical Engineering Journal*, 406:126734.

Wang, N., Sun, X., Zhao, Q., Yang, Y., and Wang, P. (2020). Leachability and adverse effects of coal fly ash: A review. *Journal of hazardous materials*, 396:122725.

Wang, Q., Yang, J., Wang, Q., and Wu, T. (2009). Effects of water-washing pretreatment on bioleaching of heavy metals from municipal solid waste incinerator fly ash. *Journal of Hazardous materials*, 162(2-3):812–818.

Wang, S. and Wu, H. (2006). Environmental-benign utilisation of fly ash as low-cost adsorbents. *Journal of hazardous materials*, 136(3):482–501.

Wilson, I. and Staffell, I. (2018). Rapid fuel switching from coal to natural gas through effective carbon pricing. *Nature Energy*, 3(5):365–372.

Wrona, J., Żukowski, W., Bradło, D., and Czupryński, P. (2020). Recovery of cenospheres and fine fraction from coal fly ash by a novel dry separation method. *Energies*, 13(14):3576.

Xi, B., Zhou, Y., Yu, K., Hu, B., Huang, X., Sui, L., and Xing, F. (2020). Use of nano-sio2 to develop a high performance green lightweight engineered cementitious composites containing fly ash cenospheres. *Journal of cleaner production*, 262:121274.

Xu, G. and Shi, X. (2018). Characteristics and applications of fly ash as a sustainable construction material: A state-of-the-art review. *Resources, Conservation and Recycling*, 136:95–109.

Xu, X., Li, Q., Cui, H., Pang, J., Sun, L., An, H., and Zhai, J. (2011). Adsorption of fluoride from aqueous solution on magnesia-loaded fly ash cenospheres. *Desalination*, 272(1-3):233–239.

Yadav, V. K., Yadav, K. K., Tirth, V., Jangid, A., Gnanamoorthy, G., Choudhary, N., Islam, S., Gupta, N., Son, C. T., and Jeon, B.-H. (2021). Recent advances in methods for recovery of cenospheres from fly ash and their emerging applications in ceramics, composites, polymers and environmental cleanup. *Crystals*, 11(9):1067.

Yao, Z., Ji, X., Sarker, P., Tang, J., Ge, L., Xia, M., and Xi, Y. (2015). A comprehensive review on the applications of coal fly ash. *Earth-science reviews*, 141:105–121.

Ye, C., Yan, B., Ji, X., Liao, B., Gong, R., Pei, X., and Liu, G. (2019). Adsorption of fluoride from aqueous solution by fly ash cenospheres modified with paper mill lime mud: Experimental and modeling. *Ecotoxicology and Environmental Safety*, 180:366–373.

Yi, H., Deng, H., Tang, X., Yu, Q., Zhou, X., and Liu, H. (2012). Adsorption equilibrium and kinetics for so2, no, co2 on zeolites fau and lta. *Journal of hazardous materials*, 203:111–117.

Yoriya, S., Intana, T., and Tepsri, P. (2019). Separation of cenospheres from lignite fly ash using acetone–water mixture. *Applied Sciences*, 9(18):3792.

Yoriya, S. and Tepsri, P. (2021). Crystal growth on cenospheres from high-calcium fly ash. *Crystals*, 11(8):919.

Yuan, Q., Zhang, Y., Wang, T., Wang, J., and Romero, C. E. (2021). Mechanochemical stabilization of heavy metals in fly ash from coal-fired power plants via dry milling and wet milling. *Waste Management*, 135:428–436.

Zandi, M. and Russell, N. V. (2007). Design of a leaching test framework for coal fly ash accounting for environmental conditions. *Environmental monitoring and assessment*, 131(1):509–526.

Zarraoa, L., González, M. U., and Paulo, Á. S. (2019). Imaging low-dimensional nanostructures by very low voltage scanning electron microscopy: Ultra-shallow topography and depth-tunable material contrast. *Scientific Reports*, 9(1):16263.

Zeng, L., Sun, H., Peng, T., and Zheng, W. (2020). Preparation of porous glass-ceramics from coal fly ash and asbestos tailings by high-temperature pore-forming. *Waste Management*, 106:184–192.

Zheng, X., Liu, J., Wei, Y., Li, K., Yu, H., Wang, X., Ji, L., and Yan, S. (2022). Glycine-mediated leaching-mineralization cycle for co2 sequestration and caco3 production from coal fly ash: Dual functions of glycine as a proton donor and receptor. *Chemical Engineering Journal*, 440:135900.

Zhou, W., Lu, X., Qi, C., and Yang, M. (2020). Utilisation of ultrasonic treatment to improve the soil amelioration property of coal fly ash. *Journal of Environmental Management*, 276:111311.

Zhu, Y., Inada, H., Nakamura, K., and Wall, J. (2009). Imaging single atoms using secondary electrons with an aberration-corrected electron microscope. *Nature materials*, 8(10):808–812.

Zimmer, A. and Bergmann, C. (2007). Fly ash of mineral coal as ceramic tiles raw material. *Waste management*, 27(1):59–68.

Żyrkowski, M., Neto, R. C., Santos, L. F., and Witkowski, K. (2016). Characterization of fly-ash cenospheres from coal-fired power plant unit. *Fuel*, 174:49–53.

APPENDIX A

PYDEEPP2SA - DOCUMENTATION

pyDeepP2SA is an advanced particle size and shape analysis (P2SA) package that leverages the cutting-edge Segment Anything Model (SAM) developed by Facebook Inc. for highly accurate and robust object segmentation. Unlike traditional approaches that rely on manual training and old-fashioned watershed algorithms, pyDeepP2SA revolutionises the field by offering a zero-generalisation segmentation technique. With minimal manual intervention, this package delivers exceptional results and simplifies the entire analysis workflow.

Prerequisites

To use pyDeepP2SA, you need to fulfill the following prerequisites:

Segment Anything Installation

Install the "Segment Anything" package by running the following command:

```
!pip install git+https://github.com/facebookresearch/segment-
    anything.git
```

SAM Checkpoint

Download one of the three available checkpoints provided by Facebook Inc. These checkpoints contain pre-trained models that are essential for the segmentation process. Save the downloaded checkpoint in a folder of your choice or on Google Drive if you are using the Colab platform. You can download the checkpoints from the Segment Anything Model Checkpoints repository.

Please ensure that you have installed the "Segment Anything" package and obtained the SAM checkpoint before proceeding with pyDeepP2SA.

Installation

Install pyDeepP2SA:

```
!pip install pyDeepP2SA
```

Functions

```
generate_masks(image, sam_checkpoint, points_per_side=32,
pred_iou_thresh=0.95, stability_score_thresh=0.9,
crop_n_layers=1, crop_n_points_downscale_factor=2,
min_mask_region_area=100)
```

This function generates masks for an input image using a SAM checkpoint.

- `image`: The input image for which masks need to be generated.

- `sam_checkpoint`: The path to the SAM checkpoint file.

- `points_per_side`: The number of points per side used for generating the masks (default: 32).

- `pred_iou_thresh`: The predicted IoU (Intersection over Union) threshold used for generating the masks (default: 0.95).

- `stability_score_thresh`: The stability score threshold used for generating the masks (default: 0.9).

- `crop_n_layers`: The number of layers used for cropping during mask generation (default: 1).

- `crop_n_points_downscale_factor`: The downscale factor used for cropping during mask generation (default: 2).

- `min_mask_region_area`: The minimum region area for a mask to be considered valid (default: 100).

Returns:

- `masks`: A list of generated masks.

```
visualise_masks(image, masks)
```

This function visualizes the segmented image with the generated masks.

- `image`: The input image.

- `masks`: The list of masks to visualize.

`save_masks_to_csv(masks, csv_directory, pixel_to_micron)`

This function saves the generated masks to a CSV file along with the calculated region properties.

- `masks`: The list of masks.

- `csv_directory`: The directory to save the CSV file.

- `pixel_to_micron`: The conversion factor from pixels to microns.

`plot_diameters(image, masks, diameter_threshold, circularity_threshold, pixel_to_micron)`

This function plots the original image with bounding boxes around the masks that have a diameter and circularity above the specified thresholds.

- `image`: The original input image.

- `masks`: The list of masks.

- `diameter_threshold`: The diameter threshold for filtering masks.

- `circularity_threshold`: The circularity threshold for filtering masks.

- `pixel_to_micron`: The conversion factor from pixels to microns, where "micron" is used as a unit name without any specific conversion factor associated with its general meaning.

`ind_mask(masks, diameter_threshold, circularity_threshold, pixel_to_micron, image)`

This function filters the masks based on diameter and circularity thresholds and plots the filtered masks along with their region properties.

- `masks`: The list of masks.

- `diameter_threshold`: The diameter threshold for filtering masks.

- `circularity_threshold`: The circularity threshold for filtering masks.

- `pixel_to_micron`: The conversion factor from pixels to microns.

- `image`: The original input image.

stat_sum(diameter_threshold, circularity_threshold, csv_directory)

This function reads the CSV file with region properties and returns a summary of the properties for the masks that meet the diameter and circularity thresholds.

- `diameter_threshold`: The diameter threshold for filtering masks.
- `circularity_threshold`: The circularity threshold for filtering masks.
- `csv_directory`: The directory where the CSV file is located.

Returns:

- `summary`: A summary of the filtered mask region properties.

plot_boxplots(diameter_threshold, circularity_threshold, csv_directory)

This function reads the CSV file and plots boxplots for the area, perimeter, diameter, and circularity of the masks that meet the diameter and circularity thresholds.

- `diameter_threshold`: The diameter threshold for filtering masks.
- `circularity_threshold`: The circularity threshold for filtering masks.
- `csv_directory`: The directory where the CSV file is located.

plot_psd(diameter_threshold, circularity_threshold, csv_directory)

This function reads the CSV file and plots the particle size distribution (PSD) using a histogram and cumulative frequency curve.

- `diameter_threshold`: The diameter threshold for filtering masks.
- `circularity_threshold`: The circularity threshold for filtering masks.
- `csv_directory`: The directory where the CSV file is located.

plot_cir(diameter_threshold, circularity_threshold, csv_directory)

This function reads the CSV file and plots the circularity distribution using a histogram.

- `diameter_threshold`: The diameter threshold for filtering masks.
- `circularity_threshold`: The circularity threshold for filtering masks.
- `csv_directory`: The directory where the CSV file is located.

`line_scan(image, image_bse, masks, circularity_threshold, min_area, csv_file, pixel_to_micron, line_distance_man, plot=False)`

Perform line scanning analysis on segmented masks within an image and store the results in a CSV file.

- `image`: The original image in which the masks are segmented.

- `image_bse`: A backscattered electron (BSE) image corresponding to the input image.

- `masks`: A list of dictionaries, where each dictionary represents a segmented mask and its properties. Each dictionary should have the following keys:

    - `segmentation`: A binary mask representing the segmented region.

    - `area`: The area of the segmented region in square pixels.

    - `predicted_iou`: Predicted intersection over union (IOU) value for the mask.

    - `bbox`: Bounding box coordinates [x, y, w, h] of the segmented region.

    - `point_coords`: Coordinates of points within the mask.

    - `stability_score`: A stability score for the mask.

    - `crop_box`: Bounding box coordinates [x, y, w, h] of the cropped mask region.

- `circularity_threshold`: Minimum circularity value for a mask to be considered in the analysis.

- `min_area`: Minimum area of a mask (in square micrometers) to be considered in the analysis.

- `csv_file`: Path to the CSV file where mask details and analysis results will be saved.

- `pixel_to_micron`: Conversion factor to convert pixel measurements to micrometers.

- `line_distance_man`: Manually set line scanning distance in pixels.

- `plot`: If True, generate and display plots during the analysis (default is False).

This function performs line scanning analysis on segmented masks to classify each mask as a 'cenosphere' or a 'solid sphere' based on the presence of line minima within the mask. The results, including circularity, area, perimeter, diameter, and type of each mask, are written to a CSV file.

Circular masks with circularity above the specified threshold and area greater than the specified minimum are considered for line scanning. For each mask, a line scanning analysis is performed along the vertical axis within the bounding box of the mask. The analysis includes fitting a polynomial curve to the pixel values along the line scan and identifying maxima and minima points.

The total number of line minima indices is used to classify the mask as a 'cenosphere' if it is greater than 0, or a 'solid sphere' if it is 0.

Region properties (area, perimeter, diameter) are also calculated and converted from pixels to micrometers using the provided conversion factor. These properties are added to the CSV file, along with the mask details.

`plot_segment_bounding_boxes(csv_file, segment_types, image)`

This function plots bounding boxes on an image based on mask details from a CSV file for specific segment types.

- `csv_file`: The path to the CSV file containing mask details.

- `segment_types`: A list of segment types (e.g., ['cenosphere', 'solid sphere']) for which bounding boxes will be plotted.

- `image`: The original image on which the bounding boxes will be overlaid.

The function reads the CSV file, filters mask details based on the specified segment types, and then creates a plot with bounding boxes. Each bounding box corresponds to a mask in the CSV file and is color-coded based on the segment type. A legend is included to explain the color-coding. The resulting plot is displayed.

`psd_spheres(csv_file)`

This function plots a particle size distribution (PSD) for cenospheres and solid spheres based on diameter information from a CSV file.

- `csv_file`: The path to the CSV file containing mask details, including diameter information.

The function reads the CSV file, separates masks into cenospheres and solid spheres, and then creates a histogram with kernel density estimation (KDE) for each category. The cenospheres are displayed in a color coded as '#FFBE86', and solid spheres are displayed in a color coded as '#8EBAD9'. The x-axis represents the diameter in micrometers, and the y-axis represents the count of particles. A legend is included to distinguish between cenospheres and solid spheres.

```
box_plots_spheres(csv_file)
```

This function creates box plots to compare the diameters of cenospheres and solid spheres based on mask details from a CSV file.

- `csv_file`: The path to the CSV file containing mask details, including diameter information.

The function reads the CSV file, separates masks into cenospheres and solid spheres, and then generates a box plot to compare the diameters of the two categories. The x-axis is labeled with 'Cenospheres' and 'Solid Spheres,' while the y-axis represents the diameter in micrometers. The title of the plot is 'Box Plot - Cenospheres vs Solid Spheres.'

These functions are designed for visualizing and analyzing mask details and particle size distributions based on the information stored in the CSV file. You can use them to gain insights into the characteristics of segmented objects in your images.

Dependencies

The code relies on the following dependencies:

- `numpy`: A library for numerical operations in Python.

- `scikit-image`: A library for image processing in Python.

- `torch` and `torchvision`: Libraries for deep learning and computer vision tasks.

- `opencv`: A library for image and video manipulation.

- `matplotlib`: A library for creating visualizations in Python.

- `pandas`: A library for data manipulation and analysis.

- `seaborn`: A library for statistical data visualization.

Make sure these dependencies are installed in your Python environment before running the code.

Example notebook

Access a comprehensive example notebook guiding you through the entire process by following this link.

APPENDIX B

SCHOLARLY CONTRIBUTIONS

B.1 Publications and manuscripts

Table B.1: *Publications and manuscripts*

Title of the paper/ manuscript	Status
Harnessing the Capabilities of Microorganisms for the Valorisation of Coal Fly Ash Waste through Biometallurgy (Link)	Published
Strategic routes in valorising coal fly ash waste to promote circular economy	In preparation
Leveraging advanced characterisation of the derivatives of pre-processed coal fly ash using deep learning and digital image processing techniques	In preparation
Shedding electrons on cenospheres: Advancing characterisation through X-ray microanalysis	Under review

B.2 Conferences, presentations, and posters

Table B.2: *Conferences, presentations, and posters*

Title of the paper	Type	Conference
Demystifying the Heterogeneity of Coal Fly Ash through Washing Cycles	Poster	International Summer School in Global Just Transition, University of Newcastle, UK
Pre-processing: A new avenue for coal fly ash circular economy	Abstract and oral presentation	World Congress on Undergraduate Research, University of Warwick, UK
Characterising Cenospheres in Coal Fly Ash for Environmental and Advanced Material Applications	Abstract and Presentation	2024 Materials Research Society (MRS) Spring Meeting & Exhibit, Seattle, Washington, USA

B.3 Magazine articles

Table B.3: *Magazine articles*

Title of the article	Magazine
Coal fly ash and circular economy (Link)	*Materials World*, Institute of Materials, Minerals & Mining (IOM3), UK
Are we going to let coal fly ash to just fly? Transforming pollution into innovation	*Bolgoda Plains*, University of Moratuwa (in preparation)

B.4 Scholarships, grants, and honours received

Table B.4: *Scholarships, grants, and honours*
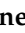
Scholarships, grants, and honours	Organisation
Full scholarship to participate World Congress on Undergraduate Research 2023	The University of Warwick, Coventry, United Kingdom
Full scholarship from to participate in the International Summer School in Global Just Transition: Equity in Net Zero	UK Energy Research Centre (UKERC)
Membership to Royal Microscopical Society (RMS) (X-ray microscopy focused interest group)	RMS, Oxford, England

B.5 Published journal article

Please refer to the next page for the article published in Minerals.

Harnessing the Capabilities of Microorganisms for the Valorisation of Coal Fly Ash Waste through Biometallurgy

Brinthan Kanesalingam [1], W. Ashane M. Fernando [2,*], Sandeep Panda [3,*], Chulantha Jayawardena [1], Dinesh Attygalle [4] and D. A. S. Amarasinghe [4]

1 Department of Earth Resources Engineering, University of Moratuwa, Katubedda 10400, Sri Lanka; kanesalingambrinthan187@gmail.com (B.K.); chulanthaj@uom.lk (C.J.)
2 Department of Nano Science Technology, Wayamba University of Sri Lanka, Kuliyapitiya 60200, Sri Lanka
3 Department of Industrial Biotechnology, Gujarat Biotechnology University, Gandhinagar 382355, India
4 Department of Material Science and Engineering, University of Moratuwa, Katubedda 10400, Sri Lanka; dattyga@uom.lk (D.A.); shantha2u@gmail.com (D.A.S.A.)
* Correspondence: ashanef@wyb.ac.lk (W.A.M.F.); sandeep.panda@gbu.edu.in (S.P.)

Abstract: Coal fly ash (CFA) is a highly versatile raw material that has the potential to yield multiple value-added products, including cenospheres, zeolites, carbon nanotubes, and fertiliser substrates. Despite its versatility, a majority of these components are often overlooked, and CFA is primarily used for construction. Conventional processing methods of CFA are known to pose significant environmental challenges, including the leaching of hazardous materials, emission of toxic gases, and the high energy consumption needed to extract the value-added components. Herein, we explore the potential of biometallurgical approaches as an eco-friendly alternative to conventional processing methods for the comprehensive utilisation of CFA. Our focus is on the application of different microorganisms to CFA, the domestication of microorganisms, preprocessing of CFA to facilitate effective biometallurgical processes, the use of bioreactors, and synthesis of nano silica particles. We also propose a novel method for extracting the value-added components from CFA using a preprocessing technique (i.e., washing cycle), combined with multiple interactions with biometallurgical processes. Adopting this approach, we not only enhance environmental stewardship but also improve the circular economic aspects of multi-component utilisation, while providing valuable insights for the development of sustainable techniques for utilising CFA.

Keywords: coal fly ash; biometallurgy; circular economy; microorganisms; washing cycle; waste valorisation

1. Introduction

Coal remains an attractive source of power, particularly in developing countries and those with high electricity demand, such as India and China, owing to its economic benefits and operational convenience. Despite the environmental and social stresses associated with coal combustion, the ever-increasing demand for energy has led to a 1.2% increase in coal usage for power generation during the global economic and political crisis in 2021, resulting in all-time high coal production in 2022. Furthermore, high gas prices and an increase in nuclear power generation suggest that no downfall in coal demand is imminent [1]. By 2025, renewable energy resources will fulfil only 90% of the future energy demand, which suggests the dominance of coal power in the near future [1]. Coal combustion products (CCPs) (along with the generation of CO_2) are the main concerns of thermal power plants operating by burning coal. CCPs include bottom ash, fly ash, boiler slag, fluidised bed combustion ash, and other solid fine particles.

Among the types of ash generated, coal fly ash (CFA) constitutes 65%–90% of the total ash volume, with an annual generation of over 1 billion metric tonnes [2]. A total of 40% of the CFA produced worldwide is not utilised to end up in landfills, disposal ponds, and

x

elsewhere, leading to environmental, social, and economic concerns [3,4]. The properties of CFA are significantly influenced by the properties of the parent coal and combustion conditions. Typically, CFA is a fine spherical material primarily composed of SiO_2 and Al_2O_3, containing both crystalline and amorphous phases, with over 50% of the total composition being amorphous. The amorphous phase is more reactive to acids and alkaline solutions, whereas the crystalline phase requires high-temperature and high-pressure conditions [5,6]. Table 1 provides a description of the major chemical compositions of CFA worldwide, whereas Figure 1 describes the distribution of trace element concentrations in CFA according to Moreno et al. [7]. The variations in the chemical composition is influenced by the type of parent coal and boiler conditions at the thermal power plant [8]. The pH of CFA varies from 1.2 to 12.5, which is largely attributed to the Ca/S molar ratio of CFA. Additionally, other minor alkaline cations, such as Na, Mg, K, and Mn, also contribute to alkalinity [9–11]. Although the majority of CFA particles are spherical silica and alumina components, irregular silica and alumina particles, Ca crystals, and unburnt carbon are also present. CFA particles generally range from a few nanometres to 500 μm in diameter [12]. A summary of the physicochemical properties of the CFA is presented in Table 2. The diversity in the properties exhibited by CFA renders it a notably challenging material to characterise, as its properties can differ across regions and even within the same region.

Table 1. Distribution of chemical composition of CFA by region. Adapted from Blissett and Rowson [13], Fomenko et al. [14], and du Toit et al. [15]. LOI—Loss on Ignition, USA—United States of America, S. Africa—South Africa, and ng—not given

Component	Range (mass%)						
	Europe	USA	China	India	Australia	Russia	S. Africa
SiO_2	28.5–59.7	37.8–58.5	35.6–57.2	50.2–59.7	48.8–66.0	63.10	54.83
Al_2O_3	12.5–35.6	19.1–28.6	18.8–55.0	14.0–32.4	17.0–27.8	28.06	30.86
Fe_2O_3	2.6–21.2	6.8–25.5	2.3–19.3	2.7–14.4	1.1–13.9	6.45	3.62
CaO	0.5–28.9	1.4–22.4	1.1–7.0	0.6–2.6	2.9–5.3	0.94	4.84
MgO	0.6–3.8	0.7–4.8	0.7–4.8	0.1–2.1	0.3–2.0	0.55	1.17
Na_2O	0.1–1.9	0.3–1.8	0.6–1.3	0.5–1.2	0.2–1.3	0.30	0.16
K_2O	0.4–4	0.9–2.6	0.8–0.9	0.8–4.7	1.1–2.9	0.51	0.63
P_2O_5	0.1–1.7	0.1–0.3	1.1–1.5	0.1–0.6	0.2–3.9	ng	0.63
TiO_2	0.5–2.6	1.1–1.6	0.2–0.7	1.0–2.7	1.3–3.7	ng	1.57
MnO	0.03–0.2	ng	ng	0.5–1.4	ng	ng	ng
SO_3	0.1–12.7	0.1–2.1	1.0–2.9	ng	0.1–0.6	0.09	0.40
LOI	0.8–32.8	0.2–11.0	ng	0.5–5.0	ng	1.45	1.19
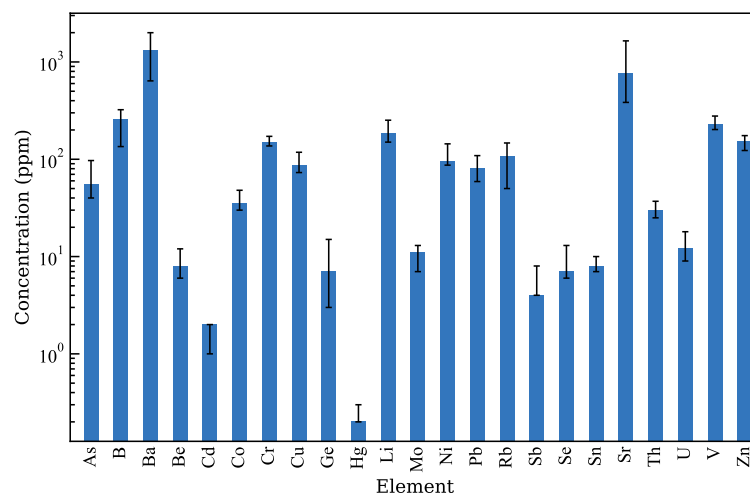
Figure 1. Distribution of trace elements of European CFA samples. Adapted from Moreno et al. [7].

Table 2. A brief summary of the chemical and physical properties of CFA. Adapted from Gollakota et al. [16].

Property	Description
Bulk density (kg/m^3)	900–1300
Specific gravity	1.6–2.6
Plasticity, Clay, Free swell index	Non-plastic, Negligible, Very low
Porosity %	30–65
Surface area (m^2/g)	5
Lime reactivity (MPa)	1–8
pH	6–8
Coefficient of uniformity (%)	3.1–10.7
Extreme particle size (mm)	0.001–0.1
Radioactivity levels in CFA (Bq/kg)	
^{226}Ra	288
^{40}K	180–500
feta	260
^{232}Th	130
^{238}U	192
Absorption (%)	12.25
Density (kg/m^3)	1380
Maximum dry density (kg/m^3)	640–1440
Optimum moisture content (%)	45.50
Los Angeles abrasion (%)	28.35
Shear strength friction angle	34°
California bearing ratio (%)	10
Permeability coefficient (cm/s)	10^{-6}–10^{-4}

The diverse properties of CFA offer numerous potential applications, such as construction materials [17–19], adsorbents [20–22], catalysts [23,24], ceramics [25–27], geopolymers [28–30], zeolites [31–33], aerogels [34,35], carbon nanotubes [36–38], soil stabilisers [39,40], and metal recovery [41,42]. Despite its widespread use in the construction industry, the economic value of CFA waste is not often fully realised.

The multi-component utilisation of CFA often involves high-energy separation processes such as calcination, high-concentration acid treatments, grinding, or milling, which arise from the heterogeneous nature of the CFA, which requires several continuous processes to effectively extract the value-added components, particularly second-generation components such as cenospheres [43–45], zeolites [13,46], carbon nanotubes [47,48], and fertiliser substrates [8,49].

CFA and Biometallurgy

The world is marching towards the concept of net zero for the emission of CO_2, which is presently acknowledged by research and industry. Fossil-fuel combustion, especially coal combustion, is a significant contributor to atmospheric CO_2 emissions. However, achieving a net zero via the unsustainable combustion of fossil fuels is economically and politically unsustainable [50]. On the contrary, up to 17% of unburnt carbon (UC) aggregates into CFA because of the low NO_x burners that control the emissions of oxides of nitrogen [51–53]. As a result, achieving net zero emissions during the valorisation process of CFA is challenging owing to the presence of UC and the potential risk of emitting other greenhouse gases. Nevertheless, it is essential to optimise the valorisation process while adhering to net-zero and sustainable concepts. In light of this, biometallurgical processes, which involve microorganisms, are promising techniques with a higher chance of driving CFA valorisation towards the expected net-zero goal.

Biometallurgy is an eco-friendly process that involves the interaction between microorganisms and metal-bearing ores using biotechnology [54,55]. Biotechnology harnesses the natural weathering capabilities of microorganisms to develop commercially profitable metal extraction flowsheets by growing them alongside the metal-containing ores or wastes

under suitable conditions. Bioleaching and biooxidation are two different mechanisms in biometallurgical processes. Bioleaching refers to the solubilisation of the target metal(s), whereas biooxidation refers to the pretreatment process of solubilising host minerals to recover the target metal(s) for subsequent processes [56]. Both processes use essentially the same principles and consortia of microorganisms for solubility. Biometallurgical studies typically use microorganisms belonging to bacteria, archaea, and fungi, because of their ability to grow under a wide range of environmental conditions.

While the application of microorganisms for processing low-grade sulphide ore has emerged as an alternative to conventional processes, the mainstream adoption of utilising microorganisms for non-sulphide minerals remains limited, although there have been studies on extracting elements from metal oxides such as laterite ores [57–59]. The capabilities of microorganisms under extreme and varying conditions, as discussed in detail by Dopson and Okibe [60], recent advances in synthetic biology, and the identification of various strains of microorganisms have provided researchers with a viable option to explore the possibility of using microorganisms for extensive biometallurgical processes [61,62]. Thus, this process is particularly attractive for the treatment of low-grade complex ores, such as CFA [55].

Biomining and bioremediation are two aspects of biometallurgy that are currently being highlighted by researchers, particularly in the treatment of CFA, which comprises hazardous materials in trace amounts. Biomining refers to the extraction of metals from metal sources, whereas bioremediation involves the removal or immobilisation of hazardous contaminants such as heavy metals and radioactive elements from sources [63].

Biomining of CFA involves the extraction of approximately 316 individual minerals and 188 mineral groups through bioleaching or biooxidation processes [64]. Bioleaching of CFA can be performed using one-step, two-step, or spent medium-step methods, depending on the specific requirements of the process [65]. The one-step process involves the simultaneous addition of both microorganisms and ore during the leaching process. In contrast, in the two-step process, microorganisms are added to the ore when biometabolite production begins [66]. The spent medium-step uses the leachants produced by the microorganisms in the absence of microorganisms for the bioleaching process. The one-step and two-step processes involve the direct bioleaching of microorganisms, whereas the spent medium step does not involve direct interaction and is therefore referred to as indirect bioleaching [65]. On the other hand, bioremediation of CFA is an essential component of its utilisation. CFA contains significant quantities of potentially toxic elements, such as Cd, Pb, Ni, Se, and Hg which can enter the food chain when contaminated with soil or groundwater [8]. Additionally, the presence of As in CFA and the formation of different chemical forms owing to their different oxidation states (i.e., -3, 0, $+3$, and $+5$) can be a significant threat to aquatic, terrestrial, and human life [67]. The advantage of bioremediation is that it solubilises hazardous arsenic components and retains them in solution, unlike pyrometallurgical processes which produce various flue gases (for example, As_2O_3 and As_4O_6), which are harmful to livelihoods [68,69].

Biometallurgical processes have advantages, such as operation at low temperatures and atmospheric pressure (in general), low energy consumption, and a small carbon footprint compared to other metallurgical processes. On the other hand, prolonged operational times (in the order of months to years) to obtain economically valuable target products and to maintain the longevity and robustness of biological systems are among the primary concerns of biometallurgical processes [56]. Table 3 provides a detailed account of the major differences between the pyrometallurgy, conventional hydrometallurgy, and biometallurgical processes.

Table 3. Advantages and challenges in major metallurgical processes compared to biometallurgy. After Mossali et al. [70].

Type of Process	Pyrometallurgy	Conventional Hydrometallurgy	Biometallurgy
Advantages	Moderate energy consumption	Low capital investment	Low capital investment
	Fast reaction kinetics	High level of separation	No hazardous gas emission
	Low production cost	High recovery efficiency	Controlled generation of wastewater
	Easy procedure	High-quality output	Low energy consumption
	No passivation steps	Good technology readiness	
	Optimal technology readiness	No hazardous gas emission	
	Fast reaction kinetics		
Challenges	High capital investment	High energy consumption	Reduced sensitivity of the process
	Low level of separation	Moderate reaction kinetics	Slow reaction kinetics
	Hazardous gas emission	High production cost	Require high process optimisation
	Material loss	Production of wastewater	Selectivity of leaching
	Complexity of the procedure		
	Need for pre-treatment		
	Selectivity of reagents		

Although biotechnology has made remarkable advances in various fields, including medicine, pharmaceuticals, agriculture, and biofuels, its application to coal [71–73] and coal-derived products has been relatively less explored. CFA waste, in particular, presents significant challenges owing to its heterogeneous chemical and physical nature, which makes it difficult to propose a robust workflow. Unlike electronic wastes such as printed circuit boards [74], which have a relatively more explicit distribution of elements, the natural distribution of elements in CFA is not always evident. This review delves into the historical evolution of biometallurgical methods for extracting elements from CFA, and sheds light on the challenges and possibilities within this field. By exploring the potential expansion of biometallurgy in the CFA domain, this paper presents a promising starting point for biometallurgy-incorporated multi-component utilisation of CFA.

2. Diversity of Microorganisms in CFA Biometallurgical Processes

The microorganisms utilised in biometallurgical processes for CFA can be categorised into two primary groups based on the processes they facilitate. The first group comprises those that aid in bioleaching, whereas the second group comprises those that carry out bioaccumulation or biosorption. Bioleaching is facilitated by chemolithoautotrophic bacteria that can survive in acidic environments with low pH and utilise inorganic materials, such as iron and sulphur, as energy sources, as well as CO_2 as the carbon source. These microorganisms are commonly used to leach sulphidic minerals and ores. In contrast, heterotrophs that use organic carbon as the carbon source are typically employed for non-sulphide minerals, such as CFA [66,75]. However, various microorganisms and experimental parameters have been tested to evaluate the feasibility of using biometallurgical processes to recover value-added components from CFA.

2.1. Fungus

The first study to investigate the bioleaching of CFA used an *Aspergillus niger (A. niger)* strain (ATCC 9142), which produces citric acid as a leaching agent [76]. This strain converts sucrose into equal amounts of citric and oxalic acid to produce the necessary organic acids for leaching [77]. Studies by Singer et al. [76] and Torma and Singh [77] focused on Al extraction, and Jadhav and Hocheng [78] achieved almost complete removal of metals such as Mn, Mg, Cu, Zn, Na, Fe, Ca, B, K, Al, Se, Co, V, Ti, and Cd, except for Cr (93% ± 1.18), Ni

(83% $\pm$ 0.32), As (78% $\pm$ 0.52), and Pb (70% $\pm$ 0.20), within 4 h under optimal conditions using the same fungal strain. However, *A. niger* strains cannot survive high concentrations of CFA, making scaling up for industrial purposes challenging [79]. Therefore, two other fungal strains, *Fusarium oxysporum* and *Penicillium glabrum*, were employed by Tacstan [79] and they were found to perform optimally at pH 5.0 and pH 6.0, respectively. *F. oxysporum* yielded high recoveries for Mo (100%), S (64.36%), Ni (50%), and Cu (33.33%), while *P. glabrum* yielded recoveries for Mo (100%), S (57.43%), Ni (25%), Si (24.66%), V (12.5%), Ti (5%), and Sr (3.2%). In addition to citric and oxalic acids, *Cladosporium cladosporioides*, a heterotrophic fungus, was found to bioleach V and Ni with 65.4% and 74.6% efficiencies, respectively, using malic acid production [80]. The two-step process of heterotrophic fungal bioleaching was found to be more effective than the one-step process because it allows fungal spores to germinate into mycelia and extract elements from CFA [79].

However, major concerns regarding heterotrophic fungal bioleaching are that it is typically performed in a neutral pH range, making contamination by other microorganisms likely. Moreover, bioleaching through fungal mycelia can lead to the adsorption or encapsulation of CFA particles, making subsequent processes such as zeolite synthesis impossible [75].

2.2. Bacteria

Although chemolithoautotrophic bacteria are generally not considered effective for non-sulphidic ores, they have been the subject of many studies investigating CFA bioleaching. These microorganisms perform bioleaching through both contact and non-contact mechanisms, whereby they oxidise ferrous (Fe^{2+}) to ferric (Fe^{3+}) and reduce sulphur (S_8, $S_2O_3^{2-}$ and H_2S or polysulphides) to sulphuric acid (H_2SO_4) [66]. Unlike heterotrophic fungi, a source of energy, such as pyrite, is essential to support the growth of chemolithoautotrophic bacteria. For instance, meso-acidophilic *A. ferrooxidans* produces H^+ ions through pyrite hydrolysis/oxidation, which are then consumed by CFA to further contribute during dissolution. In contrast, chemolithotrophic heterotrophs, such as *Typha latifolia*, which use organic carbon as a carbon source, require additional carbon during the bioleaching process, which is supplemented to the bacterial strain during inoculation [81]. However, in one-step or spend medium-step processes, the additional carbon requirement is fulfilled by the presence of UC in the CFA.

The patent for the bioleaching method for CFA was acquired by Fass et al. [82] in 1994 using *Thiobacillus thiooxidans* strains adapted to a seawater-based culture medium containing 50% CFA to extract Al, Ti, and Co. The use of chemolithoautotrophic bacteria in CFA bioleaching is heavily affected by the alkaline nature of CFA particles, which inhibits the growth of microorganisms. However, the domestication process can enhance their growth; a detailed account of the domestication process can be found in Section 3. In the one-step process, the bacteria produce multiple acids and extracellular polysaccharides during the multiplication and bioleaching phases, which are adsorbed onto the surface of the CFA particles, especially for microorganisms with flagella, such as *Bacillus amyloliquefaciens* [83]. The bacteria then secrete acidic products such as citric, lactic, succinic, and acetic acids, which dissolve the surface of the CFA particles and break down the bonds of the amorphous components.

The bioleaching process using *Thiobacillus thiooxidans* occurs indirectly through the production of sulphuric acid, which is the primary cellular metabolite, with other metabolites having relatively insignificant effects on bioleaching. In a comparative study, stock sulphuric acid and *T. thiooxidans* resulted in similar extraction rates and levels of major metal components (i.e., Al and Fe) from CFA particles under the same leaching conditions ($0.8 \leq pH \leq 5$ and the same rate of pH decrease) [84]. However, after notable preprocessing procedures, such as acid treatment and washing with deionised water, *Acidithiobacillus ferrooxidans*, a bacterium that generates $Fe_2(SO_3)_3$, performed 5–22 times higher in leaching experiments than the control suspension [85]. Unlike the use of sulphuric acid in a two-step process, this study used a spent medium step which enhanced the efficacy of the process

by incorporating microbial cultures into the leaching environment to sustain the metabolic processes necessary for an effective leaching.

Bioleaching processes using chemolithotrophic bacteria are often performed in a two-step process owing to the alkaline nature of CFA. However, chemolithotrophic bacteria were able to tolerate a higher pulp density of CFA (40% (w/v)), and effective leaching was performed at 20% (w/v) during the study by Kermer et al. [86], showing its ability to perform in the one-step process as well. Furthermore, an increase in temperature led to increased bioleaching kinetics; however, the final yields of the elements were the same except for Fe. Reductive bioleaching under anaerobic conditions increased the recovery of Fe, Mg, Zn, Al, Ca, Si, and several REEs compared with aerobic conditions. The extraction of most of the considered elements reached values between 30 and 60%, with Cr, Mg, Mn, and Zn reaching 60%–70%. Bioleaching using gluconic acid-producing *Acidomonas methanolica* increased the mobilisation of several mineral ions, such as Al, Ca, Fe, and Mg, compared with stock HCl experiments. The extraction of element ions ranged from 30 to 60% for Ce, Sr, Ti, V, and Zr, and 50%–80% extraction for Ca.

The potential use of CFA in nutrient restoration, along with nitrogen-fixing blue-green algae, for agricultural purposes in an eco-friendly manner, was enabled by using *cyanobacterial* strains, including *Nostoc muscorum*, *Anabaena variabilis*, *Tolypothrix tenuis*, and *Aulosira fertilissimia*, which are commonly used as biofertilisers [87]. Under the optimal conditions, *Nostoc muscorum* accumulated 3.65 mg/g of Cr and 2.12 mg/g of Pb, while *Anabaena variabilis* yielded 0.313 mg/g of Cu, 2.01 mg/g of Pb, 1.21 mg/g of Cr, and 0.697 mg/g of Zn.

Assuming that CFA shrinks uniformly over time, researchers used a shrinking core model to evaluate the rate control factor of bioleaching [88]. The findings indicated that for all the metals considered in this study, the rate-controlling mechanism was diffusion through the ash layer. This observation may be due to the interference of biofilms formed by *Pseudomonas* species and organic complexing agents during bioleaching. As biofilm formation increases over time, the extraction of trace metals from the CFA surface diminishes and the penetration of organic acids produced by the bacteria decreases. A subsequent study by Rezaei et al. [89] reinforced that the rate-limiting step is the diffusion of reagents to the surface of the particles.

In addition to the bioleaching process, a bio-accumulation process was also investigated to recover the Ti-rich fraction from the leachate produced by the acid treatment of CFA using a specifically cultivated bacterium, *Rhodococcus* GIN-1, on magnetite particles to form a magnetite biosorbent, as described by Shabtai and Mukmenev [90].

The resulting leachate was subjected to stepwise precipitation (similar to Fass et al. [82]) using pH changes, and the precipitates at a pH of 2.05 were coupled to the bacterium strain. Three cycles of biomagnetic separation were performed, resulting in 70-fold enrichment of Ti from the initial precipitate. The aggregation of TiO_2 around the bacterial cells during precipitation suggests a possible nucleation effect on the bacteria. The other suspensions were collected by adjusting the pH of the NH_4OH solution. This study effectively employed bacterial translocation from magnetite to Ti-containing materials, and almost 99% of the magnetite was recovered after operation and could be reused. This study offers a new perspective on the biometallurgical application of the bioaccumulation process for extracting industrially valuable Ti, which provides high-purity Ti in an environmentally friendly manner.

2.3. Yeast

The potential for utilising a single strain of *Y. lipolytica* for both bioleaching and bioaccumulation was investigated by Banker et al. [91]. This study revealed that *Y. lipolytica* can accumulate heavy metals through its cell wall, membrane, and cytoplasm, as well as perform bioleaching through the secretion of citric acid and two extracellular proteins. Notably, this approach achieved a Cu extraction rate of 59.41%, which was higher than that obtained using synthetic citric acid.

In another study, Park and Liang [92] explored the use of three microbial strains, namely, *Candida bombicola*, *Phanerochaete chrysosporium*, and *Cryptococcus curvatus*, for leaching REEs. Only *C. bombicola* was selected, owing to its superior mineral leaching efficiency. *C. bombicola* has the ability to thrive in low pH conditions and demonstrated the best performance among all the strains tested.

2.4. Using Mixed Culture of Microorganisms for the Bioleaching

The use of mixed culture of microorganisms in biotechnological processes has become an effective means to encounter dynamic changes in the process environments due to the interaction between microorganisms and non-sulphidic ores [93]. It is crucial to understand the role of each microorganism under bioleaching conditions to enhance the efficiency of the bioleaching process [94]. While considering the alkaline nature of CFA, it can hinder the performance of sulphur-oxidising bacteria, which are one of the commonly used microorganisms in bioleaching processes. As such, this may lead to a decreased production of sulphuric acid, which subsequently can affect the performance of the bioleaching process. To overcome this, pre-processing techniques can be used to reduce the alkaline nature of CFA, as discussed in Section 4. Alternatively, biosurfactant-producing microorganisms (i.e., microorganisms that produce surface-active biomolecules) such as *Pseudomonas*, *Bacillus*, *Candida*, *Rhodococcus*, and *Corynebacterium* can be used to facilitate the bioleaching process at higher pH levels owing to their better environmental compatibility and specific activity under extreme conditions [95,96]. This behaviour enables continuous bioleaching over a wide range of pH values and yields higher metal recovery during the process [97].

Another effective combination of microorganisms for bioleaching, as suggested by Mahmoud et al. [93], includes chemoautotrophic bacteria and heterotrophic microorganisms. Chemoautotrophs have the ability to decrease the pH of the medium or solution by oxidising sulphide minerals. The resulting biogenic acid, specifically H_2SO_4, can then interact with the CFA to counterbalance its alkalinity. Consequently, the CFA sample becomes more conducive to the activity of heterotrophic bacteria, which also produce acidity through the generation of organic acids. This synergistic effect can enhance the efficiency of the leaching process.

3. Domestication Process of Microorganisms

A key element in the domestication of microorganisms for industrial processes is the purposeful selection and breeding of microorganisms from diverse sources such as waste dumps, soil, plants, and waterways [98]. The collected microorganisms are then grown in the presence of increasing concentrations of materials to be leached; this process is known as domestication [66]. Despite the time-consuming nature of the domestication process, which can take several months to years, it has been widely adopted in most biometallurgical applications. A successful transition to industrial processes demands prompt adaptation of microorganisms, as it is a crucial parameter that governs the rate and feasibility of bioprocesses. Previous studies on sulphide mineral bioleaching have demonstrated that a gradual increase in the concentration of metal ions during the domestication process enhances the tolerance of microorganisms, leading to an increase in the rate and degree of bioleaching [99]. In addition to the metal ion concentration, domestication also improves the adaptability of microorganisms to pH variations, temperature fluctuations, and tolerance to toxic materials. The goal of domestication is to reduce or eliminate the lag phase during the bioleaching process, resulting in a pronounced performance of adapted microorganisms compared to their unadapted counterparts [100].

The process of domesticating microorganisms for use in biometallurgy of CFA is significantly affected by the characteristics of CFA. The high-pH environment created by CFA during the bioleaching process results in an alkaline solution that can hinder the growth of acidophilic bacteria. Additionally, easily dissolvable ions such as Ca, Mg, and K, which are found on the surface of CFA particles, dissolve into the solution and further increase its pH. Furthermore, the presence in the CFA of toxic elements such as As, Cd, Cr, Cu,

Hg, Pb, V, and Zn, inhibits the proliferation of microorganisms. Therefore, the adaptability of microorganisms prior to their use in CFA biometallurgical processes is essential for achieving notable outcomes.

Domestication has been shown to enhance the production of microbial secondary metabolites in both one-step and two-step processes. In particular, the domestication of microorganisms plays a crucial role in the one-step process of bioleaching because they directly interact with CFA. However, it is necessary to adapt the microorganisms in the bioaccumulation or biosorption processes, as they will also directly interact with CFA. Seidel and Zimmels [101] reported the inhibition of *Thiobacillus thiooxidans* growth due to an increase in pH, which resulted in a lag phase of approximately 5 to 6 days in the bioleaching process. Similar results were observed recently by Su et al. [100]. The study found that *Acidithiobacillus thiooxidans* required acclimatisation, particularly in alkaline-treated CFA, because of the pH increase in the first five days. The acclimatisation process delayed the stabilisation of *Acidithiobacillus thiooxidans* by three days in the alkali-treated CFA. The results of domestication on the adaptability of the microorganisms are evident by their ability to perform bioleaching at a relatively high concentration of 20% CFA slurry medium.

Figure 2A illustrates the protein levels of *Acidithiobacillus thiooxidans* under various conditions, including pure, alkali-treated, and acid-treated CFA, as well as a medium without CFA. The initial growth of microorganisms is impeded in the presence of CFA. However, after a 5-day acclimation period, bacterial growth increased and surpassed that of the solution without CFA. At the plateau stage, the amounts of bacterial protein reached 0.615, 0.445, and 0.608 mg/mL, respectively, which were greater than that of the solution without CFA. This behaviour can be largely attributed to the presence of S in CFA, which serves as an energy source for the growth of microorganisms [100].
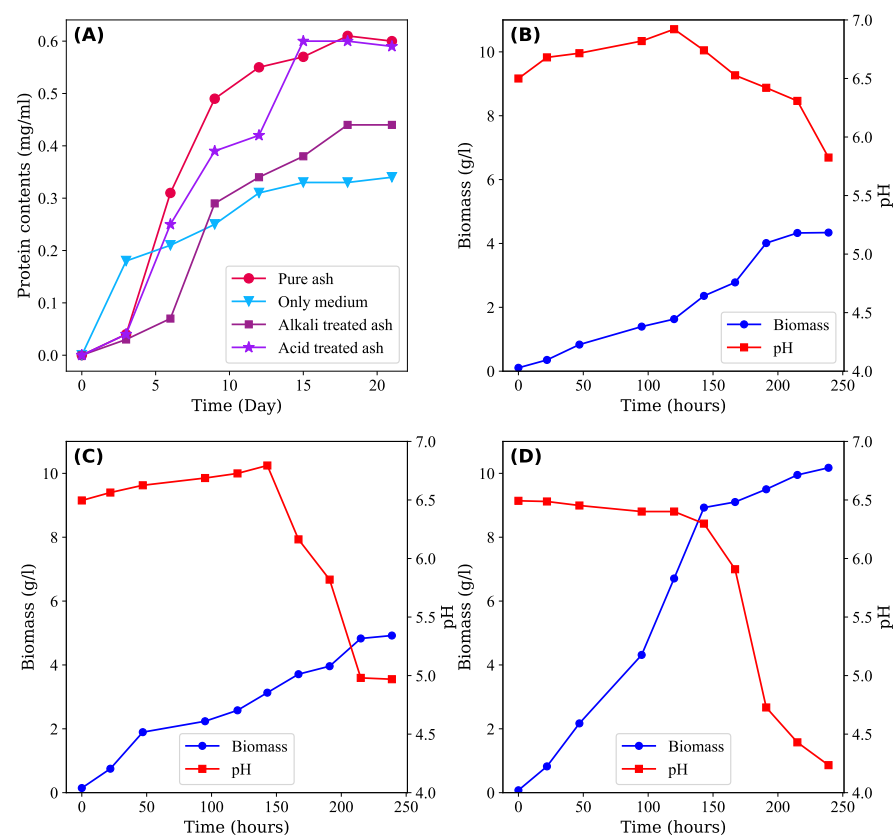

Figure 2. (**A**) Protein content of *Acidithiobacillus thiooxidans* in various conditions: pure ash, alkali-treated ash, acid-treated ash, and culture medium after the domestication process [100]. (**B**) Changes in pH and biomass concentration during the growth of *Bacillus barbaricus* during the absence of CFA, (**C**) presence of CFA, and (**D**) presence of water washed CFA [102].

4. Preprocessing of CFA for the Biometallurgical Processes

The primary purpose of preprocessing is to facilitate successful interactions between CFA particles and microorganisms, enhance the growth of microorganisms, and increase the kinetics of the biometallurgical processes. Various pre-processing methods have been reported in the literature, including size reduction/separation, thermal treatment, alkaline/acid treatment, and washing with water, which can be used alone or in combination to achieve optimal results.

The effect of preprocessing on the biometallurgical process can be divided into two parts: leaching of the surface rim and grooving of the CFA core. The surface rim encompasses easily leachable alkaline components that impede the initial growth of microorganisms (see Section 3) [100,101]. These alkaline oxides dissolve in the medium during the bioleaching process and increase the pH of the system, subsequently controlling the growth of the microorganisms. Furthermore, dissolving the surface rim of CFA can enhance the leaching process by increasing the surface area of CFA particles and subsequently the interaction between microorganisms and CFA particles, facilitating the direct involvement of microorganisms with the core of the CFA [103].

4.1. Washing with Water

Washing with deionised water is an effective technique for removing easily dissolvable ions from the CFA surface rim. Studies have shown that washing with water can remove a significant amount of alkaline ions from the CFA surfaces. Jadhav and Hocheng [78] used 100 mL of distilled water and 1 g of CFA sample at 30 °C for 24 h to remove 100% Na, 47% ($\pm$0.45) B, 38.07% ($\pm$0.12) Ca, 29.89% ($\pm$0.78) Mg, and 11.8% ($\pm$0.05) K through bioleaching.

The removal of alkaline components enhanced the production of acids by *Bacillus barbaricus* during the bioleaching process performed by Sen et al. [102]. Under optimal conditions (i.e., pH 6, temperature 37 °C, 1% CFA, 240 mesh particle size, and 40% inoculum concentration), citric, oxalic, and silicic acid production for untreated CFA were 22.57%, 11.29%, and 9.56%, respectively, and those treated with water (CFA) were 28.54%, 16.89%, and 13.21%, respectively. These results show that washed CFA yielded better outcomes than unwashed CFA, allowing for higher acid production than untreated CFA. The alumina concentration in the washed CFA increased from 25.45% to 34.72% after 60 days, and the residual silica content was reduced from 62.14% to 40.71%. This result demonstrates the efficiency of washing CFA with water before bioleaching. The biometallurgical approach for extracting silica from CFA has limitations compared to the volumetric method, which involves acid treatment followed by alkali digestion under pressure. The volumetric method requires only 4 h to leach out 37.09% of silica, whereas the biometallurgical approach requires 60 days to leach out only 21.43% of silica [104]. Additionally, the results of bioleaching time reported by Jadhav and Hocheng [78] and Sen et al. [102] differed, which may be due to the quantity of CFA samples used for the study, as Jadhav and Hocheng [78] used 1 g, whereas Sen et al. [102] used 10 g. In addition to the initial CFA mass, factors such as pH, temperature, additional energy sources, and other parameters may also have contributed to the differences in these observations.

Figure 2 depicts the pH and biomass (total weight of microorganisms per unit volume of solution) trends under three distinct conditions: (B) the absence of CFA, (C) untreated CFA, and (D) CFA treated with water. Notably, at the end of the 250th hour, there was an observable trend in the amount of biomass (g/L of solution), where the highest amount of biomass was found in the water-treated CFA, followed by untreated CFA and the absence of CFA. This outcome is surprising given that the presence of CFA creates harsh conditions for microorganism growth due to the confinement and release of toxic materials, which contests the common hypothesis. One plausible explanation for the observed enhancement is the presence of sulphur in the form of SO_3, which may serve as a direct energy source for microbial growth. Furthermore, trace elements enriched in CFA may provide additional growth factors, as suggested by Su et al. [100]. Moreover, Sen et al. [102] found that the

kinetics of treated CFA became faster than that of untreated CFA, as evidenced by the sigmoidal behaviour of the biomass in washed CFA compared with untreated CFA.
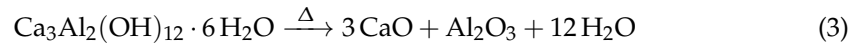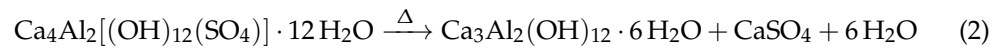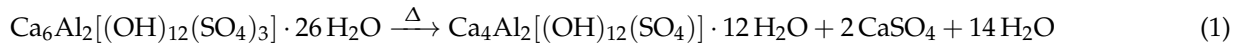
4.2. Grinding and Sieving

The exposed surface area of the particles heavily influences the probable interactions between microorganisms and CFA particles. This phenomenon is determined by the particle size and shape. Smaller particles have a higher specific surface area than larger particles, and are therefore more likely to interact with microorganisms and increase the efficiency of the bioprocess. The particle size distribution of CFA varies widely, ranging from a few nanometres to hundreds of micrometres [13]. The experimental results from Jekic et al. [85] showed that even with acid treatment, the extraction of elements from the CFA was not significant. This observation was mainly due to the larger particle size of the CFA in the experiment, with over 46% measuring 100 μm or more. Therefore, most elements are encapsulated inside the core of the CFA. In light of this, using smaller particles in biometallurgical processes related to CFA is desirable [85,105].

To this end, grinding is often a go-to-process employed to obtain suitable particle sizes to effectively process the CFA particles. In some studies, researchers have collected a particular fraction of CFA for further analysis, which can be isolated through sieving. Different sizes of CFA have been preferred for biometallurgical processes by various researchers. For instance, Torma and Singh [77] ground their particles to a size of less than 45 μm, whereas Park and Liang [92] used particles that passed through a 200 sieve (i.e., 74 μm) to extract REEs. The selection of finer particles for REEs extraction is important because REEs commonly aggregate as fine particles in the CFA matrix. In another study, Sen et al. [102] found that the optimal particle size for the leaching process was a 240 sieve, that is, less than 53 μm. Grinding before sieving has little effect on REE extraction but is explicitly beneficial for major elements such as Si and Al.

4.3. Thermal Treatment

Thermal treatment is a widely recognised technique for facilitating particle–microorganism interactions. Three types of thermal treatments associated with CFA preprocessing have been identified before biometallurgical processes: heating CFA particles alone, and heating them with acid or alkali components to intensify the reaction kinetics. In this section, we focus on the effects of heating CFA particles alone, with the other two treatments discussed in subsequent sections.

Thermal treatment of CFA is often performed at very high temperatures because it has already been exposed to temperatures ranging from 1000 °C to 1600 °C during coal combustion in thermal power plants [106–108]. Thermal pretreatment serves two primary purposes before bioprocesses: the recrystallisation of amorphous components of the CFA increases the efficiency of the bioleaching, and the transformation of low soluble components to readily soluble components [86]. Kermer et al. [86] examined CFA samples heated at 900, 1000, and 1057 °C for 1, 4, and 9 h to investigate the mineralogical changes induced by thermal treatment. The results showed a significant decrease in the amorphous fraction of CFA, which was attributed to the partial recrystallisation of major mineral components such as quartz (SiO_2) (melting point of 1650 °C). However, no significant changes were observed in the haematite (Fe_2O_3), periclase (MgO), or rutile (TiO_2) phases. Complex components including gypsum ($CaSO_4 \cdot 2H_2O$) and ettringite ($3CaO \cdot Al_2O_3 \cdot 3CaSO_4 \cdot 32H_2O$) were broken down into simpler components, making their elements available for leaching. A possible mechanism for the dissociation of ettringite is presented in Equations (1)–(3): Notably, the study also observed the formation of gehlenite ($Ca_2Al[AlSiO_7]$) complexes at approximately 800 °C, which, upon interaction with SiO_2, resulted in the formation of anorthite ($CaAl_2Si_2O_8$) and wollastonite ($CaSiO_3$), as shown in Equations (4) and (5).

xx

$$Ca_6Al_2[(OH)_{12}(SO_4)_3] \cdot 26\,H_2O \xrightarrow{\Delta} Ca_4Al_2[(OH)_{12}(SO_4)] \cdot 12\,H_2O + 2\,CaSO_4 + 14\,H_2O \qquad (1)$$

$$Ca_4Al_2[(OH)_{12}(SO_4)] \cdot 12\,H_2O \xrightarrow{\Delta} Ca_3Al_2(OH)_{12} \cdot 6\,H_2O + CaSO_4 + 6\,H_2O \qquad (2)$$

$$Ca_3Al_2(OH)_{12} \cdot 6\,H_2O \xrightarrow{\Delta} 3\,CaO + Al_2O_3 + 12\,H_2O \qquad (3)$$

$$2\,CaO + Al_2O_3 + SiO_2 \xrightarrow{\Delta} Ca_2Al[AlSiO_7] \qquad (4)$$

$$Ca_2Al[AlSiO_7] + 2\,SiO_2 \xrightarrow{\Delta} Ca_2Al_2Si_2O_8 + CaSiO_3 \qquad (5)$$

However, it is essential to acknowledge that thermal treatment at high temperatures for extended periods of time requires substantial energy and poses significant sustainability concerns. Despite the shown promise for subsequent bioleaching of heat-treated CFA operating at higher temperatures, it must be carefully monitored to mitigate adverse environmental impacts such as the generation of flue gases and high energy utilisation.

4.4. Acid Treatment

The primary objective of treating CFA with acid is to modify the crystal lattice and make the components present in the core of the CFA available for biometallurgical processes. Further, in the place of water washing processes, acid treatment can be used to remove the alkali components. However, prior to treatment with sulphuric acid, a comprehensive assessment of the presence of calcium is necessary, as it can lead to the formation of calcium sulphate on the cells of microorganisms and energy sources, such as sulphur particles. This precipitation can hamper cell growth, resulting in self-inhibition and hindrances to mass transfer [84]. Therefore, it is recommended to use nitric acid or hydrochloric acid for acid treatment of unwashed CFA. Seidel et al. [84] found that the growth of microorganisms in acid-treated CFA (with HCl) is faster than that in untreated CFA. However, the effectiveness of acid treatment may decrease with a larger particle size, thereby lowering the expected metal extraction.

According to Kermer et al. [86], treating digested CFA with $HCl_{(aq)}$ (31%, 100 °C, for 4 h) improved the leaching efficiency of Ca, Fe, Al, and Mg. The residue left after the HCl treatment comprised amorphous materials, quartz, and smaller amounts of diopside ($CaMgSi_2O_6$), mullite ($Al_6Si_2O_{13}$), and rutile. Additionally, supercritical-CO_2 digestion, by redirecting the emitted CO_2 from smokestacks to CFA, can cause anion exchange on the CFA surface. The strong diffusion and permeability properties of supercritical-CO_2 can cause near-surface conversion of the crystal lattice of CFA, resulting in tension within the structure and encouraging proton attack. This process may play a role in achieving net-zero CO_2 emissions using emitted CO_2 for CFA treatment [109]. Further, the addition of acid enhances the process, as shown in Figure 3. However, acid treatment results in carbonification of CFA particles, which is not conducive to the extraction of REEs [100]. Preprocessing CFA with high-concentration acids for preliminary leaching is not recommended, as it is intended only to prepare CFA for subsequent bioleaching processes.
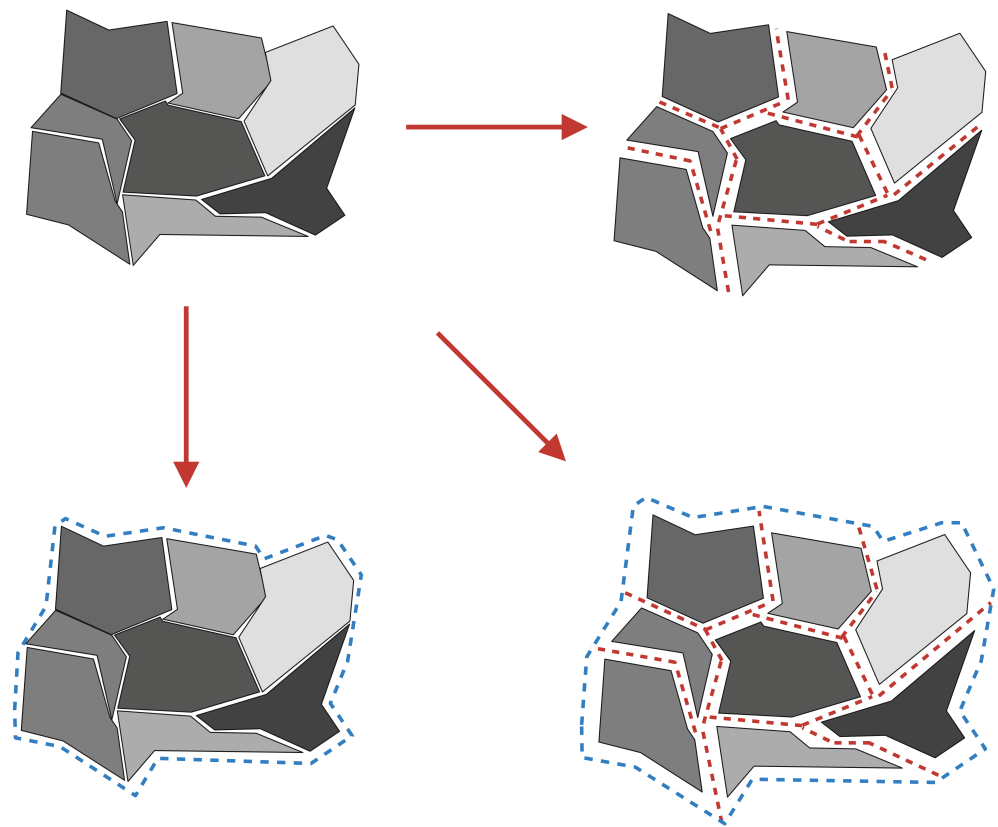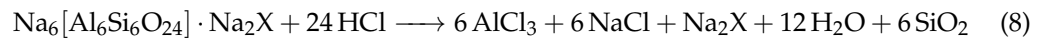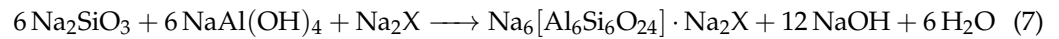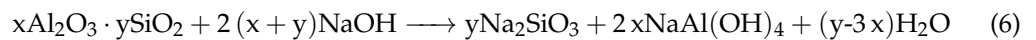
Figure 3. Schematic diagram of individual effects of super critical-CO$_2$ (**A,B**) and HCl (**A–C**), as well as their combined effect (**A–D**) on the mineral components of CFA [86].

4.5. Alkaline Treatment

The alkaline treatment of CFA has a notable effect on the structure of the particles. The core of the CFA, which contains Al, Si, and critical elements, is enclosed by strong and chemically stable Si-O-Si and Si-O-Al bonds. However, the addition of alkaline components, such as -OH bonds, to the CFA matrix causes a decrease in the degree of polymerisation of these stable bonds and subsequently increases the number of broken and unsaturated bonds [110]. This change in the surface charge distribution of CFA particles leads to the deterioration of the stable structure of the CFA core, enabling microorganisms to interact with CFA.
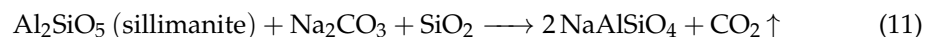
Additionally, alkaline treatment reduces the Si and Al contents in the CFA matrix (due to the desilication and dissolution of mullite), resulting in a highly porous structure, which is an excellent opportunity for the diffusion of other elements through bioleaching [100,111]. This effect is further demonstrated by the observed decrease in the particle size (d_{50}) of pure, acid-treated, and alkali-treated CFA particles, which were found to be 36.21, 24.62, and 16.76 μm, respectively [100]. The reduction in particle size and the increase in irregular particles due to the grooves created by the alkaline treatment enhanced the adsorption kinetics and diffusion mechanism of CFA. Comparative experiments presented in Su et al. [100] revealed that hydrothermal alkaline treatment yielded higher concentrations of critical elements than hydrothermal acid treatment. Furthermore, the experiments related to treating the CFA with a NaOH solution clearly demonstrate the process of core deterioration in the CFA, thereby revealing its inner components for additional leaching [111]. However, there is a possibility of precipitation of desilication products, specifically Na$_6$[Al$_6$Si$_6$O$_{24}$]·Na$_2$X, where X represents different inorganic anions. This precipitation could potentially impact the continuous leaching process. To overcome this challenge, it is recommended to employ a high concentration of alkaline solution or follow it with subsequent acid leaching [111,112]. This process can be described by

Equations (6)–(8). A commonly observed trend in the application of alkaline treatments is their use for extracting trace elements during bioleaching processes.

$$x Al_2O_3 \cdot y SiO_2 + 2(x+y)NaOH \longrightarrow y Na_2SiO_3 + 2 x NaAl(OH)_4 + (y\text{-}3 x)H_2O \quad (6)$$

$$6 Na_2SiO_3 + 6 NaAl(OH)_4 + Na_2X \longrightarrow Na_6[Al_6Si_6O_{24}] \cdot Na_2X + 12 NaOH + 6 H_2O \quad (7)$$

$$Na_6[Al_6Si_6O_{24}] \cdot Na_2X + 24 HCl \longrightarrow 6 AlCl_3 + 6 NaCl + Na_2X + 12 H_2O + 6 SiO_2 \quad (8)$$

Seddiek et al. [80] conducted a stepwise roasting process of CFA to concentrate V and increase its accessibility for the bioleaching process by fungi called *Cladosporium cladosporioides* in a two-step process. The CFA was preheated to 500 °C for 3 h and 90% wt. Na_2CO_3 at 850 °C and 20% wt. Na_2CO_3 was then added at 1000 °C for 2 h. An increase in temperature without Na_2CO_3 inhibits the metal recovery, even though, with the removal of carbon and volatile components, the fungal growth is increased, whereas on the other hand, the dissolving of heavy metals into the solution will be inhibited by the toxic metals. On the other hand, alkaline treatment increases the efficiency of V bioleaching at 850 °C using 90% wt. Na_2CO_3, whereas Ni was extracted from the raw CFA without any treatment. A plausible reason for this increased efficiency in V but not in Ni is that the addition of Na_2CO_3 during heating leads to the formation of water-soluble sodium metavanadate ($NaVO_3$), which subsequently enhances V leaching.

Torma and Singh [77] calcined CFA with a CaO/SiO_2 molar ratio of 2. The as-received CFA was resistant to 1- and 2-step leaching processes, and yielded only 5%–8% of Al. However, calcined CFA produced an extraction yield of 93.5 %. Fan et al. [113] roasted CFA using Na_2CO_3 at 850 °C for 2 h. This process transforms mullite and sillimanite (Al_2SiO_5) into a more extractable nepheline via the reactions presented in Equations (9)–(11). Figure 4 illustrates the morphological conversions of CFA with varying CFA/Na_2CO_3 mass ratios. Increasing the amount of Na_2CO_3 causes the rigid spherical structure of CFA to break down, resulting in irregular shapes. An increase in the amount of Na_2CO_3 destroys the rigid spherical physical body of the CFA particles and makes them irregular. This modification significantly enhances the surface area of the CFA particles. Nevertheless, excessive Na_2CO_3 can cause CFA particles to aggregate once again, resulting in large and ineffective irregular particles. Bioleaching experiments were then performed using meso-acidophilic *Acidithiobacillus ferrooxidans* on activated CFA samples as a one-step process. Pyrite was added as an energy source to provide Fe and sulphur. *A. ferrooxidans* produces H^+ ions through the bioleaching of pyrite, which is consumed by the CFA during dissolution.

$$Al_6Si_2O_{13} \, (\text{mullite}) + 3 Na_2CO_3 + 4 SiO_2 \longrightarrow 6 NaAlSiO_4 + 3 CO_2 \uparrow \quad (9)$$

$$Na_2CO_3 + SiO_2 \longrightarrow Na_2SiO_3 + CO_2 \uparrow \quad (10)$$

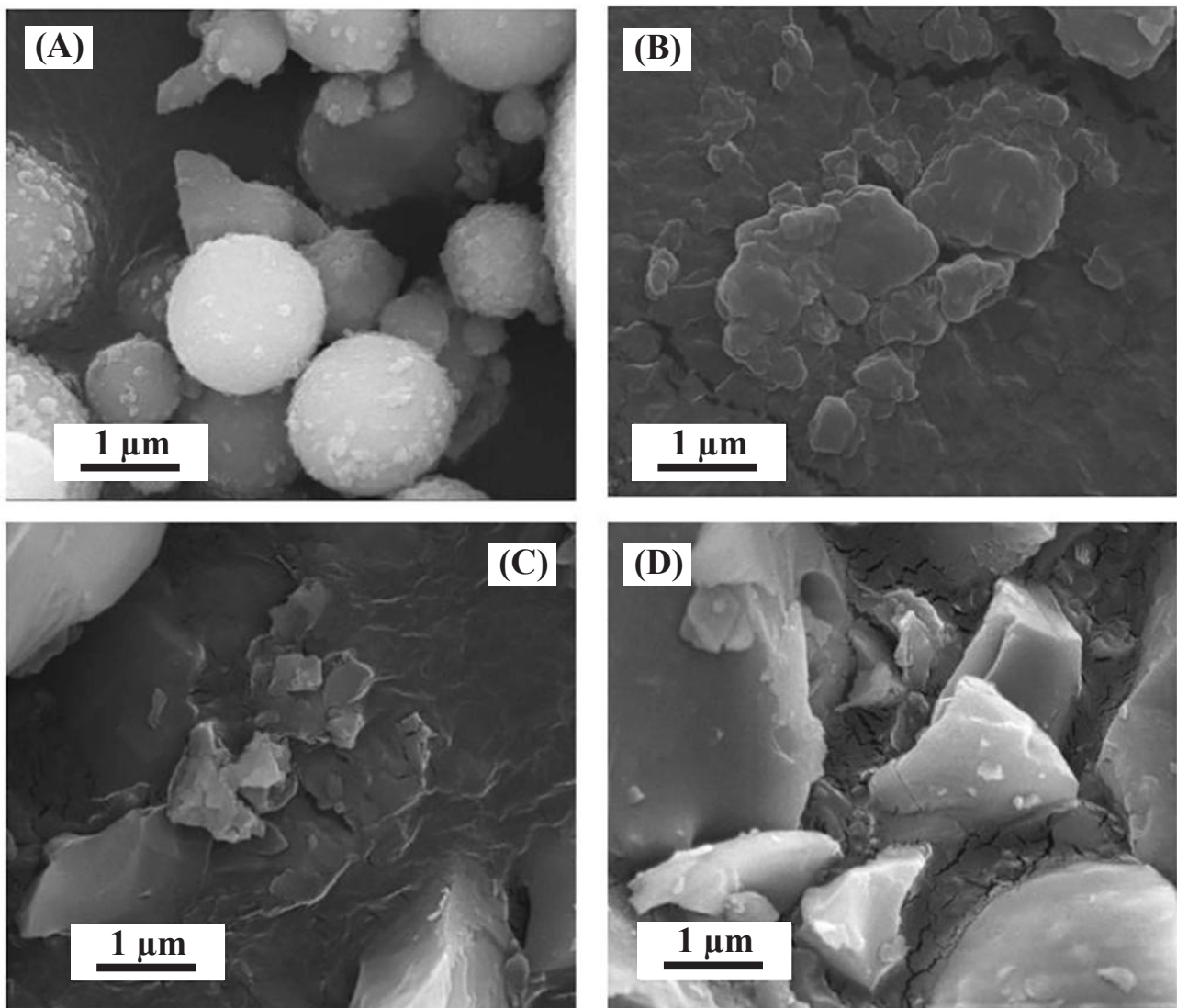$$Al_2SiO_5 \, (\text{sillimanite}) + Na_2CO_3 + SiO_2 \longrightarrow 2 NaAlSiO_4 + CO_2 \uparrow \quad (11)$$
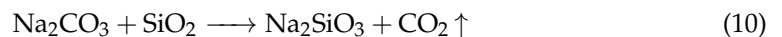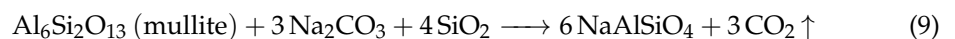
Figure 4. Scanning electron microscopy (SEM) images of (**A**) CFA and CFA particles activated under CFA/Na$_2$CO$_3$ mass ratios (**B**) 1:0.19, (**C**) 1:0.22, and (**D**) 1:0.25 [113].

5. Utilisation of Bioreactors

The use of bioreactors is crucial in the fields of biotechnology and bioengineering because they provide controlled environments for the growth of living cells and organisms. Bioreactors have been used in a variety of biotechnological processes, including the production of vaccines, enzymes, and biofuels. However, potential applications of bioreactors extend beyond the production of biologically derived products. These devices or systems enable the precise control of a range of parameters, including temperature, pH, pulp density, nutrient levels, dissolved oxygen, stirring rate, etc. The ability to control these parameters facilitates the optimisation of cellular growth and metabolic activity, leading to a robust process, thereby increasing the yield and quality of the products. Furthermore, bioreactors establish synergy between mixed cultures of microorganisms, leading to improved biotechnological processes. Interested readers can find more detailed discussions on bioreactor technology from other sources, such as [55]. The use of bioreactors in the field of mineral processing has been industrialised since 1986, with the extraction of Au from sulphide sources in the Fairview mine in South Africa [93]. This success paved the way for further industrial and laboratory applications of bioreactors, particularly in the recovery of elements from low-grade mineral ores and secondary resources, such as electronic circuit boards and combustion residuals.

The use of bioreactors in the biometallurgical process of CFA has not been well established and rarely experimented. To ensure consistent output in the face of the heterogeneous nature of CFA, it is crucial to establish a robust working environment. The dynamic changes caused by mineral leaching at different stages and their pH-dependent precipitation ability pose a concern that must be closely monitored and managed. It is also important to create a favourable environment for microorganisms to carry out bioleaching and regulate the supply of energy sources, particularly during one-step or spent medium-step processes. Given these complexities, tight control over these parameters is necessary, and the use of bioreactors may be a viable option to achieve this control. Muravyov et al. [114] conducted batch processing of bioleaching in laboratory reactors with a capacity of 2.5 L, using acidophilic chemolithotrophic microbial communities to produce sulphuric acid. The parameters employed were a stirring rate of 500 rpm, aeration rate of 4 L/min, and an operating temperature of 28 ($\pm$1) or 45 ($\pm$1) °C. Optimal conditions for bioleaching were found to be a pulp density of 10%, an initial pH of 2.0, and a 10:1 ratio of acid-soluble waste to elemental sulphur. The yields of Sc, Y, and La recovered after 10 days of bioleaching at 45 °C were 52.0%, 52.6%, and 59.5%, respectively.

Zhang et al. [115] performed a two-step bioleaching process using a custom-made automatic bioreactor setup, which accommodated the *Acidithiobacillus ferrooxidans*. A schematic of the designed bioreactor is presented in Figure 5A, and the bioreactor is capable of providing a daily input of pure pyrite of 15 g, resident time up to 5 days, with an effluent concentration of $Fe_2(SO_4)_3$ of 10 g/L, and a pH of approximately 1.3. The resulting solution was then used for leaching for almost 72 h, yielding approximately 4 ppm or 13%–14% yield of the total REEs. Longer-duration tests yielded approximately 40%–60% of the individual REEs. Precipitation was designed using Visual Minteq calculations and modelling, resulting in a final REEs precipitation product containing 36.7% REEs. Figure 5B shows the precipitates of REEs as small flakes of solids about 10 to 15 μm in size. Most REEs are associated with the aluminosilicate phase of CFA, making them inaccessible through conventional bioleaching processes [116]. Therefore, the use of bioreactors in the recovery of REEs is a promising step towards achieving a high yield, as the critical parameters can be changed and adjusted for optimal performance of microorganisms.

The appropriate bioreactor configuration for acidophiles is the stirring tank reactor model, as highlighted by Deive and Sanroman [117]. Additionally, the pozzolanic properties of CFA and its sedimentation characteristics must be carefully assessed, as these factors are detrimental to bioreactor performance. Stirring through a shaft and impeller in the stir tank configuration can help ensure a homogeneous solution throughout the process, which could potentially eliminate CFA cementation. The efficiency of bioreactor operations can be further enhanced by developing a series of in-line bioreactors, each with different operating conditions, for extracting multiple elements at each stage. This continuous flow of CFA through multiple reactors enables the stepwise dissolution of specific elements and their extraction and retrieval, significantly improving the extraction efficiency and proper utilisation of CFA resources. However, sedimentation of CFA particles in conveying tubes can be a practical issue in creating a series of in-line bioreactor processes that requires additional precautions in CFA-associated bioreactor processes.
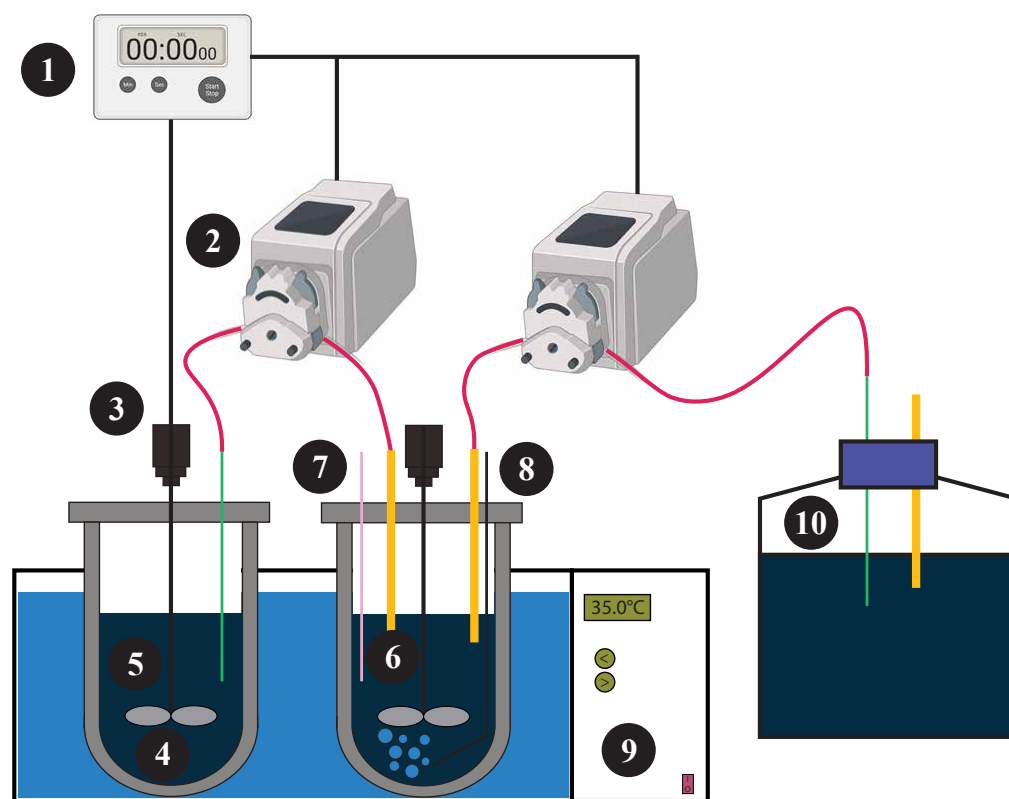
(A)
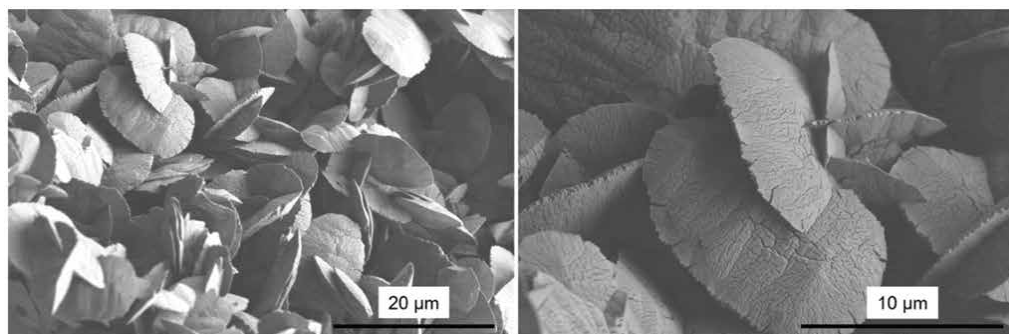
(B)

Figure 5. (**A**) Schematic diagram of a custom-made automatic bioreactor from the study of Zhang et al. [115]. Here 1—timer, 2—pumps, 3—motors, 4—shaft and impeller, 5—feeding vessel, 6—bioleaching vessel, 7—pH/Eh portal, 8—glass gas sparger, 9—water bath, and 10—leachate reservoir. Adapted from Zhang et al. [115] (**B**) Scanning electron microscopy (SEM) images of the REE precipitate [115].

6. Synthesis of Silica Nanoparticles

The synthesis of silica nanoparticles within the CFA domain has been overlooked, despite the vast abundance of silica in CFA. The economic significance of silica nanoparticles, due to their small size and high surface area, has garnered immense attention in various industries as catalysts and catalyst supports, in biomedical applications, ceramics, resins, molecular sieves, pigments, electronic substrates, precursors in photonic and solar cells for solar devices, thin-film substrates, electrical and thermal insulators, drug delivery in medicine, filters for exhaust gases, and adsorbents [118,119]. Currently, the production of silica nanoparticles from sodium silicate involves acidification, which is presently

carried out through using acids or ion exchange [120]. However, efficient extraction of silica nanoparticles from CFA may require different processing conditions because of the amorphous and crystalline forms of silica-bearing minerals [119].

Khan et al. [121] discovered that the mesophilic fungus, *Fusarium oxysporum*, could produce highly crystalline, protein-capped, and water-soluble silica nanoparticles with quasi-surface morphology extracellularly within 24 h under ambient conditions. The fungus secretes proteins and enzymes during CFA leaching, and natural protein capping caused by fungal metabolism and metabolic energy involvement during the reaction may be responsible for the leaching of nanosized silica. Furthermore, they discovered photoluminescence at room temperature, which could be useful for biomedical applications. The synthesis of porous or hollow silica is possible by changing the reaction conditions, which is useful because of its high drug-loading capacity. Khan et al. [121] found that only 40% of the yield was silica nanoparticles, and the other 50% was carbon, which could be removed using flotation. The byproducts of this process can be used to synthesise aluminosilicate compounds, such as zeolites.

The only other source in the literature for the synthesis of silica nanoparticles from CFA was found in the review Yadav and Fulekar [122]. Their previous study found that they could synthesise porous silica nanosheets 80–120 nm in size using the *B. circulans* MTCC 6811 supernatant and fly-ash-extracted sodium silicate. The optimum ratio was 4:1 of the supernatant to the extracted sodium silicate by volume. Fulekar and Yadav synthesised spherical aggregated clusters of silica nanosheets, 40–80 nm in size by incubating *Fusarium oxysporum* supernatant and sodium silicate at an optimised ratio of 3:2 in an incubator shaker at 28 °C for 48–72 h. Here, Si was leached from the sillimanite and mullite of CFA by hydrolytic enzymes of *F. oxysporum*. The Si leached from the CFA formed water-soluble silica nanoparticles, which were further dried, and the silica powder was obtained using a rotary evaporator.

7. Washing Cycle and Biometallurgy

Washing with water is a simple and effective technique that laboratories and industries can easily adopt with minimal costs. A scientific approach to washing with deionised water was studied by the authors and named the process the "washing cycle". Here, the raw CFA is continuously stirred for 15 min and then allowed to settle for another 15 min at a constant temperature. The rate of kinetics can be increased by increasing the temperature; however, it is recommended to perform washing cycles at room temperature, considering the energy requirements. This process removes loosely attached alkaline ions and other trace materials from the surface rim of the CFA, which is evinced by an increase in the pH and electrical conductivity of the leachate. These measurements acted as indicators of the dissolution efficiency of easily soluble ions from the surface rim. The number of washing cycles can be optimised to achieve the maximum dissolution of alkaline ions, as indicated by the low conductivity and pH of the solution after multiple washing cycles. This process not only prepares CFA for subsequent processes, such as zeolite synthesis or bioleaching, but also disintegrates components based on their density and ability to dissolve in deionised water. The floating top layer of the washing cycle mostly consists of cenospheres (hollow spheres), whereas the leachate contains easily soluble alkaline ions such as Ca, Mg, Na, and K. The bottom layer, which is mainly composed of Al and Si, is ideal for zeolite synthesis and is an adsorbent for wastewater treatment. This demonstrates the possibility of considering the washing cycle as a pivotal point in constructing a circular economic path for CFA waste that is presently underutilised or dumped in ash ponds.

In this section, we investigate the potential integration of eco-friendly biometallurgical techniques into the previously proposed flowsheet for CFA processing, with the aim of enhancing environmental sustainability and valorisation. The biometallurgical process can be incorporated into the existing flowsheet at three different stages: (1) immediately after the washing cycle to the leachate alkaline solution, (2) as a replacement for acid leaching and the

resultant leachate alkaline solution, and (3) after the synthesis of zeolites to pellet residues. Figure 6 presents a revised flowsheet that includes the possible biometallurgical processes.
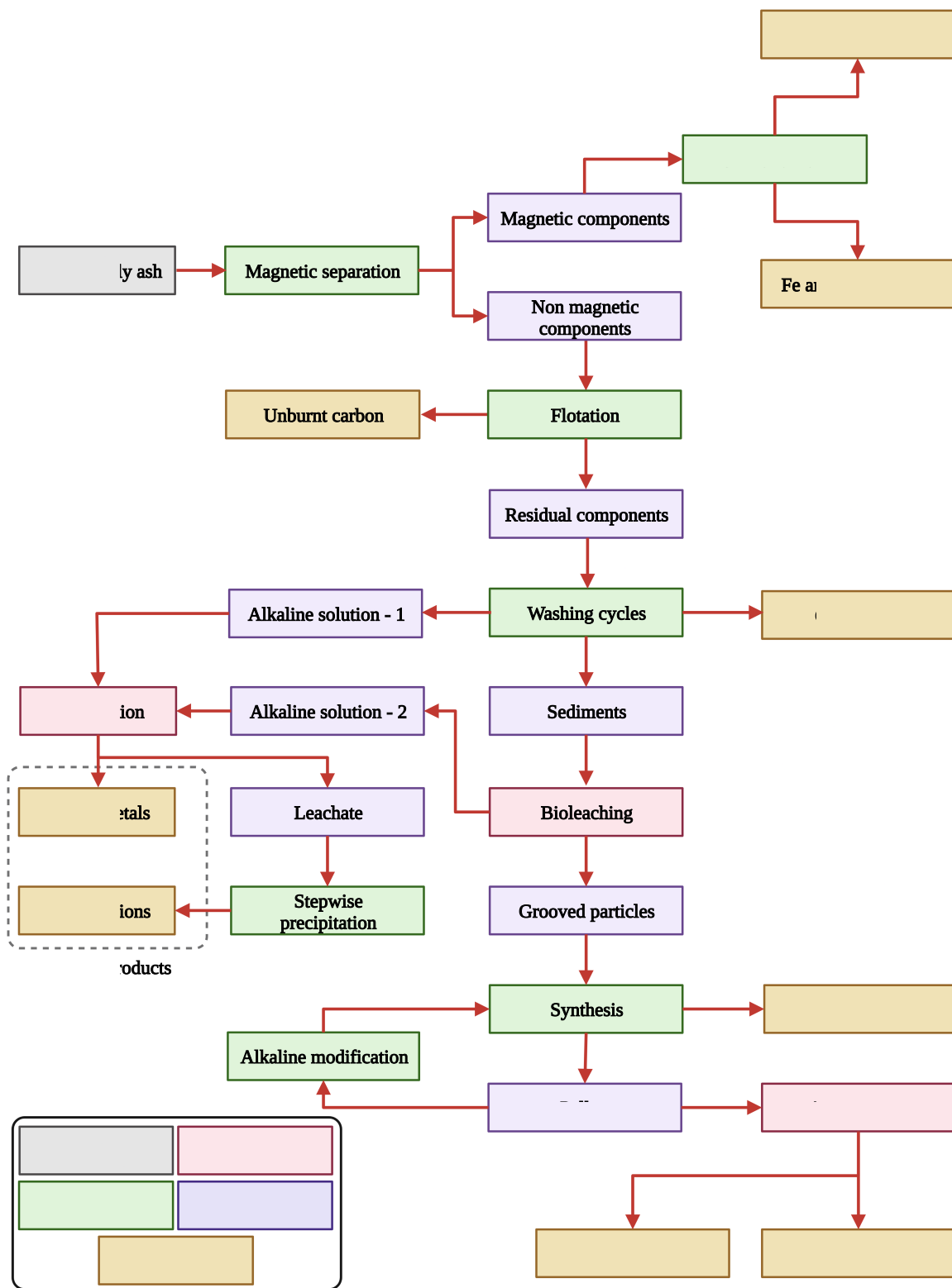

Figure 6. A prospective flowsheet for the multi-component utilisation of the CFA achieved by replacing high-energy combustion methods of processing with the biometallurgical processes.

The alkaline solution obtained from the washing cycle contains both macro and micro nutrients, including P, K, Ca, Mg, S, Fe, Zn, Mn, Cu, Co, B, and Mo, which is a significant number of heavy metals. Banker et al.'s [91] study found that *Yarrowia lipolytica* can bioaccumulate heavy metals in the cell wall, membrane, and cytoplasm, with a Cu extraction of 59.41%. This suggests that it may be possible to bioaccumulate Fe, Zn, Mn, Cu, Co, Mo, and Pb through the addition of appropriate microorganisms into the alkaline solution. Figure 7 shows the morphological changes resulting from heavy-metal biosorption by *Y. lipolytica*. The remaining solution after the biosorption process can be precipitated using a stepwise pH change and the resulting ions can be used as fertiliser products.
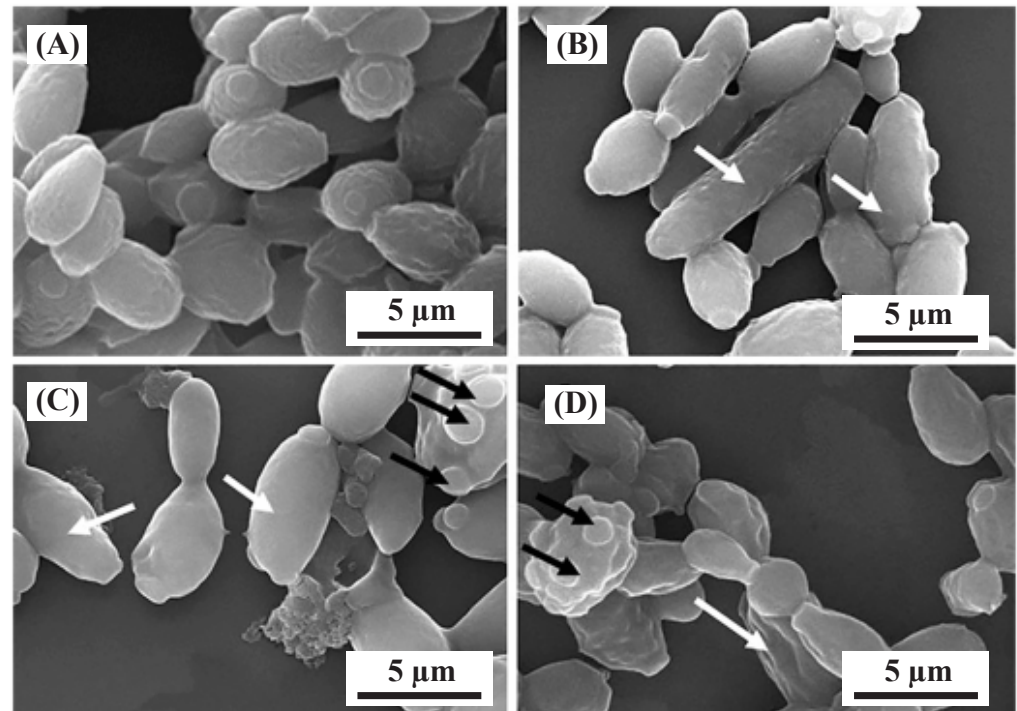

Figure 7. The changes in the morphology of *Y. lipolytica* NCIM 3589 after exposure to various metals. Scanning electron microscopy (SEM) images of cells grown in the presence of (**A**) no metal and different metals at a concentration of 0.5 mM for (**B**) zinc, (**C**) cobalt, and (**D**) nickel. Elongated cells are indicated by white arrows, while cells with multipolar buds are indicated by black arrows [123].

In the revised flowsheet, the grinding process has been intentionally omitted to avoid particle breakdown and to simplify the subsequent processes. Additionally, grinding particles can increase the overall energy consumption of the process. On the other hand, conveyance of CFA during subsequent processes may also introduce micro-cracks due to abrasion; this could have a beneficial effect on the biometallurgical processes. Bioleaching can be used as an alternative to conventional acid treatment for non-selective leaching of sediments from washing cycles, making the process environmentally friendly. The resulting leachate, i.e., alkaline solution-1, will have additional components that cannot leach during the washing cycles. The leachate can be subjected to biosorption and stepwise precipitation processes to recover heavy metals and fertiliser ions, respectively.

The solid residue from the bioleaching process consisted of grooved CFA particles that mainly encompassed Al, Si, and other critical elements. The subsequent alkaline treatment process for these grooved CFA particles extracts Al and Si, which can then be used for zeolite synthesis. Additionally, the extraction process can be intensified with microwave or ultrasonication assistance [124]. After the separation of the Al- and Si-rich solutions, the remaining pellets, enriched with critical elements including REEs, can undergo microbe-mediated surface adsorption or biosorption. This process offers a sustainable and viable approach for selective adsorption of REEs. Microorganisms with high-density

surface-accessible functional groups such as carboxylates and phosphates can facilitate high-capacity REE adsorption during growth [125]. Recent studies have explored biosorption as a potential solution for the selective recovery of REEs from coal leachates and CFA. A study by Park et al. [126] compared the use of the *Escherichia coli* strain (genetically engineered for cell surface display of lanthanide binding tags) and *Arthrobacter nicotianae* (a native bacterium that exhibits a high REE adsorption capacity) on coal leachate and CFA. The results showed that CFA had a lower REE recovery efficiency than coal leachate due to its higher non-REE content, with most of it encapsulated inside the strong core of CFA. Additionally, the low-pH wash step (i.e., acid leaching or even water washing) between adsorption and desorption yielded higher concentrations of REEs among the total metals (80% and 50% for the coal leachate and CFA, respectively). However, the present flowsheet rectified the problem associated with the higher non-REE content by removing the most of the other elements in the previous steps (i.e., washing cycle and bioleaching). In a nutshell, the loosely attached alkaline components on the surface of the rim will be gathered and precipitated through the washing cycle and biosorption process, respectively. The resulting sediment will then undergo bioleaching to improve the availability of the CFA core for subsequent processes. Therefore, a better result along with faster reaction kinetics compared with other similar experiments can be expected in the proposed flowsheet. Nevertheless, it is essential to optimise the proposed biometallurgical methods by considering influential parameters such as temperature, pulp density, stirring rate, dissolved oxygen, and energy sources. In particular, when utilising bioreactors, optimising these influential parameters and implementing process control measures will greatly enhance the overall yield. Conducting a thorough study of these parameters will be instrumental in achieving a higher scalability for this plausible flowsheet.

The updated flowsheet aims to achieve a circular economy by utilising sustainable methods to valorise the CFA. Instead of hazardous acid treatment, biometallurgical approaches have been used to improve the recovery of value-added components. Selective adsorption and precipitation steps were introduced, and possible integration was critically evaluated. However, it is important to address the limitations of these methods. CFA is a material with multiple complexities and uncertainties, making the processing flowsheet subject to change based on specific requirements. For the proposed biometallurgical processes, the use of stirring tank bioreactors is advantageous because of their high level of control over operational parameters. However, the investment costs associated with these processes are higher than those of conventional methods but can offset the recovery of additional valuable components.

8. Conclusions and Future Prospects

In this study, we reviewed and presented the application of biometallurgical processes in the multi-component utilisation of CFA to recover multiple valuable elements in an environmentally benign manner. The challenges associated with the application of these processes to CFA require a thorough understanding of the extent to which the separation process can be enhanced. Thus, in this study, we explored the interplay between biometallurgy and CFA, identifying critical factors such as the selection of microorganisms, domestication processes, preprocessing of CFA, and usage of bioreactors and their influence on the bio metallurgical processes. Furthermore, we investigated the possibility of incorporating biometallurgy into the CFA preprocessing technique, specifically, the washing cycle, and examined the potential for multi-component utilisation of CFA while adhering to the principles of the circular economy and sustainability. Our illuminating takeaways from this study are as follows:

- The addition of biometallurgical processes at different stages of the washing cycle flowsheet has been found to significantly enhance the separation of selective metal and metal groups, thereby enabling the effective recovery of heavy metals and fertiliser ions.

- Bioleaching of sediment particles after the washing cycle can improve zeolite synthesis by introducing grooves on the CFA substrate, which are effective in subsequent synthesis processes, such as alkaline-assisted hydrothermal synthesis, offering a promising avenue for the production of reproducible pure zeolites.
- Pellets generated at the end of the flowsheet have been shown to contain critical elements, including REEs, and can be extracted using biosorption, which could prove to be an alternate source for the production of advanced materials.
- The use of biometallurgical processes in flowsheets significantly improves their environmental benignity, enabling the replacement of energy-intensive processes such as acid leaching and grinding with more sustainable alternatives.

References

1. IEA. *Global Coal Consumption, 2020–2023*; IEA: Paris, France, 2022.
2. Mushtaq, F.; Zahid, M.; Bhatti, I.A.; Nasir, S.; Hussain, T. Possible applications of coal fly ash in wastewater treatment. *J. Environ. Manag.* **2019**, *240*, 27–46. [CrossRef] [PubMed]
3. Valeev, D.; Kunilova, I.; Alpatov, A.; Varnavskaya, A.; Ju, D. Magnetite and carbon extraction from coal fly ash using magnetic separation and flotation methods. *Minerals* **2019**, *9*, 320. [CrossRef]
4. Yao, Z.; Ji, X.; Sarker, P.; Tang, J.; Ge, L.; Xia, M.; Xi, Y. A comprehensive review on the applications of coal fly ash. *Earth-Sci. Rev.* **2015**, *141*, 105–121. [CrossRef]
5. Vilakazi, A.Q.; Ndlovu, S.; Chipise, L.; Shemi, A. The recycling of coal fly ash: A review on sustainable developments and economic considerations. *Sustainability* **2022**, *14*, 1958. [CrossRef]
6. Kelmers, A.; Canon, R.; Egan, B.; Felker, L.; Gilliam, T.; Jones, G.; Owen, G.; Seeley, F.; Watson, J. Chemistry of the direct acid leach, calsinter, and pressure digestion-acid leach methods for the recovery of alumina from fly ash. *Resour. Conserv.* **1982**, *9*, 271–279. [CrossRef]
7. Moreno, N.; Querol, X.; Andrés, J.; Stanton, K.; Towler, M.; Nugteren, H.; Janssen-Jurkovicová, M.; Jones, R. Physico-chemical characteristics of European pulverized coal combustion fly ashes. *Fuel* **2005**, *84*, 1351–1363. [CrossRef]
8. Shaheen, S.M.; Hooda, P.S.; Tsadilas, C.D. Opportunities and challenges in the use of coal fly ash for soil improvements—A review. *J. Environ. Manag.* **2014**, *145*, 249–267. [CrossRef]
9. Izquierdo, M.; Querol, X. Leaching behaviour of elements from coal combustion fly ash: An overview. *Int. J. Coal Geol.* **2012**, *94*, 54–66. [CrossRef]
10. Kolbe, J.L.; Lee, L.S.; Jafvert, C.T.; Murarka, I.P. Use of alkaline coal ash for reclamation of a former strip mine. In Proceedings of the World of Coal Ash (WOCA) Conference, Denver, CO, USA, 9–12 May 2011; pp. 1–15.
11. Ward, C.R.; French, D.; Jankowski, J.; Dubikova, M.; Li, Z.; Riley, K.W. Element mobility from fresh and long-stored acidic fly ashes associated with an Australian power station. *Int. J. Coal Geol.* **2009**, *80*, 224–236. [CrossRef]
12. Wang, N.; Sun, X.; Zhao, Q.; Yang, Y.; Wang, P. Leachability and adverse effects of coal fly ash: A review. *J. Hazard. Mater.* **2020**, *396*, 122725. [CrossRef]
13. Blissett, R.; Rowson, N. A review of the multi-component utilisation of coal fly ash. *Fuel* **2012**, *97*, 1–23. [CrossRef]
14. Fomenko, E.V.; Anshits, N.N.; Kushnerova, O.A.; Akimochkina, G.V.; Kukhtetskiy, S.V.; Anshits, A.G. Separation of nonmagnetic fine narrow fractions of PM10 from coal fly ash and their characteristics and mineral precursors. *Energy Fuels* **2019**, *33*, 3584–3593. [CrossRef]
15. du Toit, G.; van der Merwe, E.M.; Kruger, R.A.; McDonald, J.M.; Kearsley, E.P. Characterisation of the hydration products of a chemically and mechanically activated high coal fly ash hybrid cement. *Minerals* **2022**, *12*, 157. [CrossRef]

16. Gollakota, A.R.; Volli, V.; Shu, C.M. Progressive utilisation prospects of coal fly ash: A review. *Sci. Total Environ.* **2019**, *672*, 951–989. [CrossRef] [PubMed]

17. Lu, X.; Liu, B.; Zhang, Q.; Wen, Q.; Wang, S.; Xiao, K.; Zhang, S. Recycling of Coal Fly Ash in Building Materials: A Review. *Minerals* **2023**, *13*, 25. [CrossRef]

18. Yang, J.; Huang, J.; Su, Y.; He, X.; Tan, H.; Yang, W.; Strnadel, B. Eco-friendly treatment of low-calcium coal fly ash for high pozzolanic reactivity: A step towards waste utilization in sustainable building material. *J. Clean. Prod.* **2019**, *238*, 117962. [CrossRef]

19. Kelechi, S.; Adamu, M.; Uche, O.; Okokpujie, I.; Ibrahim, Y.E.; Obianyo, I. A comprehensive review on coal fly ash and its application in the construction industry. *Cogent Eng.* **2022**, *9*, 2114201. [CrossRef]

20. Ochedi, F.O.; Liu, Y.; Hussain, A. A review on coal fly ash-based adsorbents for mercury and arsenic removal. *J. Clean. Prod.* **2020**, *267*, 122143. [CrossRef]

21. Singh, N.; Agarwal, A.; De, A.; Singh, P. Coal fly ash: An emerging material for water remediation. *Int. J. Coal Sci. Technol.* **2022**, *9*, 1–32. [CrossRef]

22. Visa, M.; Isac, L.; Duta, A. Fly ash adsorbents for multi-cation wastewater treatment. *Appl. Surf. Sci.* **2012**, *258*, 6345–6352. [CrossRef]

23. Asl, S.M.H.; Ghadi, A.; Baei, M.S.; Javadian, H.; Maghsudi, M.; Kazemian, H. Porous catalysts fabricated from coal fly ash as cost-effective alternatives for industrial applications: A review. *Fuel* **2018**, *217*, 320–342.

24. Pavlović, S.M.; Marinković, D.M.; Kostić, M.D.; Janković-Častvan, I.M.; Mojović, L.V.; Stanković, M.V.; Veljković, V.B. A CaO/zeolite-based catalyst obtained from waste chicken eggshell and coal fly ash for biodiesel production. *Fuel* **2020**, *267*, 117171. [CrossRef]

25. Wang, S.; Zhang, C.; Chen, J. Utilization of coal fly ash for the production of glass-ceramics with unique performances: A brief review. *J. Mater. Sci. Technol.* **2014**, *30*, 1208–1212. [CrossRef]

26. Little, M.; Adell, V.; Boccaccini, A.; Cheeseman, C. Production of novel ceramic materials from coal fly ash and metal finishing wastes. *Resour. Conserv. Recycl.* **2008**, *52*, 1329–1335. [CrossRef]

27. Erol, M.; Küçükbayrak, S.; Ersoy-Mericboyu, A. Comparison of the properties of glass, glass–ceramic and ceramic materials produced from coal fly ash. *J. Hazard. Mater.* **2008**, *153*, 418–425. [CrossRef] [PubMed]

28. Andini, S.; Cioffi, R.; Colangelo, F.; Grieco, T.; Montagnaro, F.; Santoro, L. Coal fly ash as raw material for the manufacture of geopolymer-based products. *Waste Manag.* **2008**, *28*, 416–423. [CrossRef] [PubMed]

29. You, S.; Ho, S.W.; Li, T.; Maneerung, T.; Wang, C.H. Techno-economic analysis of geopolymer production from the coal fly ash with high iron oxide and calcium oxide contents. *J. Hazard. Mater.* **2019**, *361*, 237–244. [CrossRef]

30. Nyale, S.M.; Babajide, O.O.; Birch, G.D.; Böke, N.; Petrik, L.F. Synthesis and characterization of coal fly ash-based foamed geopolymer. *Procedia Environ. Sci.* **2013**, *18*, 722–730. [CrossRef]

31. Cardoso, A.M.; Paprocki, A.; Ferret, L.S.; Azevedo, C.M.; Pires, M. Synthesis of zeolite Na-P1 under mild conditions using Brazilian coal fly ash and its application in wastewater treatment. *Fuel* **2015**, *139*, 59–67. [CrossRef]

32. Querol, X.; Moreno, N.; Umaña, J.t.; Alastuey, A.; Hernández, E.; Lopez-Soler, A.; Plana, F. Synthesis of zeolites from coal fly ash: An overview. *Int. J. Coal Geol.* **2002**, *50*, 413–423. [CrossRef]

33. Koshy, N.; Singh, D. Fly ash zeolites for water treatment applications. *J. Environ. Chem. Eng.* **2016**, *4*, 1460–1472. [CrossRef]

34. Wu, X.; Fan, M.; Mclaughlin, J.F.; Shen, X.; Tan, G. A novel low-cost method of silica aerogel fabrication using fly ash and trona ore with ambient pressure drying technique. *Powder Technol.* **2018**, *323*, 310–322. [CrossRef]

35. Kang, A.H.; Shang, K.; Ye, D.D.; Wang, Y.T.; Wang, H.; Zhu, Z.M.; Liao, W.; Xu, S.M.; Wang, Y.Z.; Schiraldi, D.A. Rejuvenated fly ash in poly (vinyl alcohol)-based composite aerogels with high fire safety and smoke suppression. *Chem. Eng. J.* **2017**, *327*, 992–999. [CrossRef]

36. Dunens, O.M.; MacKenzie, K.J.; Harris, A.T. Synthesis of multiwalled carbon nanotubes on fly ash derived catalysts. *Environ. Sci. Technol.* **2009**, *43*, 7889–7894. [CrossRef] [PubMed]

37. Salah, N.; Al-Ghamdi, A.A.; Memic, A.; Habib, S.S.; Khan, Z.H. Formation of carbon nanotubes from carbon-rich fly ash: Growth parameters and mechanism. *Mater. Manuf. Process.* **2016**, *31*, 146–156. [CrossRef]

38. Alam, J.; Yadav, V.K.; Yadav, K.K.; Cabral-Pinto, M.M.; Tavker, N.; Choudhary, N.; Shukla, A.K.; Ali, F.A.A.; Alhoshan, M.; Hamid, A.A. Recent advances in methods for the recovery of carbon nanominerals and polyaromatic hydrocarbons from coal fly ash and their emerging applications. *Crystals* **2021**, *11*, 88. [CrossRef]

39. Rivera, J.F.; Orobio, A.; Cristelo, N.; de Gutierrez, R.M. Fly ash-based geopolymer as A4 type soil stabiliser. *Transp. Geotech.* **2020**, *25*, 100409. [CrossRef]

40. Nalbantoğlu, Z. Effectiveness of class C fly ash as an expansive soil stabilizer. *Constr. Build. Mater.* **2004**, *18*, 377–381. [CrossRef]

41. Wu, M.; Qi, C.; Chen, Q.; Liu, H. Evaluating the metal recovery potential of coal fly ash based on sequential extraction and machine learning. *Environ. Res.* **2023**, *224*, 115546. [CrossRef]

42. Sahoo, P.K.; Kim, K.; Powell, M.; Equeenuddin, S.M. Recovery of metals and other beneficial products from coal fly ash: A sustainable approach for fly ash management. *Int. J. Coal Sci. Technol.* **2016**, *3*, 267–283. [CrossRef]

43. Ranjbar, N.; Kuenzel, C. Cenospheres: A review. *Fuel* **2017**, *207*, 1–12. [CrossRef]

44. Danish, A.; Mosaberpanah, M.A. Formation mechanism and applications of cenospheres: A review. *J. Mater. Sci.* **2020**, *55*, 4539–4557. [CrossRef]

45. Shende, D.Z.; Wasewar, K.L.; Wadatkar, S.S. Target-Specific Applications of Fly Ash Cenosphere as Smart Material. *Handbook of Nanomaterials and Nanocomposites for Energy and Environmental Applications*; Springer: Cham, Switzerland, 2021; pp. 3349–3369.

46. Ahmaruzzaman, M. A review on the utilization of fly ash. *Prog. Energy Combust. Sci.* **2010**, *36*, 327–363. [CrossRef]

47. Singh, R.; Volli, V.; Lohani, L.; Purkait, M.K. Polymeric ultrafiltration membranes modified with fly ash based carbon nanotubes for thermal stability and protein separation. *Case Stud. Chem. Environ. Eng.* **2021**, *4*, 100155. [CrossRef]

48. Wu, L.; Liu, J.; Reddy, B.R.; Zhou, J. Preparation of coal-based carbon nanotubes using catalytical pyrolysis: A brief review. *Fuel Process. Technol.* **2022**, *229*, 107171. [CrossRef]

49. Jala, S.; Goyal, D. Fly ash as a soil ameliorant for improving crop production—A review. *Bioresour. Technol.* **2006**, *97*, 1136–1147. [CrossRef]

50. Fankhauser, S.; Smith, S.M.; Allen, M.; Axelsson, K.; Hale, T.; Hepburn, C.; Kendall, J.M.; Khosla, R.; Lezaun, J.; Mitchell-Larson, E.; et al. The meaning of net zero and how to get it right. *Nat. Clim. Chang.* **2022**, *12*, 15–21. [CrossRef]

51. Jha, V.K.; Nagae, M.; Matsuda, M.; Miyake, M. Zeolite formation from coal fly ash and heavy metal ion removal characteristics of thus-obtained Zeolite X in multi-metal systems. *J. Environ. Manag.* **2009**, *90*, 2507–2514. [CrossRef]

52. Temuujin, J.v.; Van Riessen, A. Effect of fly ash preliminary calcination on the properties of geopolymer. *J. Hazard. Mater.* **2009**, *164*, 634–639. [CrossRef]

53. Miyake, M.; Kimura, Y.; Ohashi, T.; Matsuda, M. Preparation of activated carbon–zeolite composite materials from coal fly ash. *Microporous Mesoporous Mater.* **2008**, *112*, 170–177. [CrossRef]

54. Rawlings, D.E.; Johnson, D.B. *Biomining*; Springer: Berlin/Heidelberg, Germany, 2007.

55. Kaksonen, A.H.; Boxall, N.J.; Gumulya, Y.; Khaleque, H.N.; Morris, C.; Bohu, T.; Cheng, K.Y.; Usher, K.M.; Lakaniemi, A.M. Recent progress in biohydrometallurgy and microbial characterisation. *Hydrometallurgy* **2018**, *180*, 7–25. [CrossRef]

56. Johnson, D.B. Biomining—Biotechnologies for extracting and recovering metals from ores and waste materials. *Curr. Opin. Biotechnol.* **2014**, *30*, 24–31. [CrossRef] [PubMed]

57. Ghassa, S.; Noaparast, M.; Shafaei, S.Z.; Abdollahi, H.; Gharib, F.; Magdouli, S. Optimization of pyrite bio-oxidation to produce ferric reagent for sphalerite leaching. *J. Hazardous Toxic Radioact. Waste* **2022**, *26*, 04021035. [CrossRef]

58. Saleh, D.K.; Abdollahi, H.; Noaparast, M.; Nosratabad, A.F.; Tuovinen, O.H. Dissolution of Al from metakaolin with carboxylic acids produced by Aspergillus niger, Penicillium bilaji, Pseudomonas putida, and Pseudomonas koreensis. *Hydrometallurgy* **2019**, *186*, 235–243. [CrossRef]

59. Schippers, A.; Hedrich, S.; Vasters, J.; Drobe, M.; Sand, W.; Willscher, S. Biomining: Metal recovery from ores with microorganisms. *Geobiotechnol. I Met. Relat. Issues* **2014**, *141*, 1–47.

60. Dopson, M.; Okibe, N. Biomining Microorganisms: Diversity and Modus Operandi. In *Biomining Technologies: Extracting and Recovering Metals from Ores and Wastes*; Springer: Berlin/Heidelberg, Germany, 2022; pp. 89–110.

61. Gumulya, Y.; Boxall, N.J.; Khaleque, H.N.; Santala, V.; Carlson, R.P.; Kaksonen, A.H. In a quest for engineering acidophiles for biomining applications: Challenges and opportunities. *Genes* **2018**, *9*, 116. [CrossRef]

62. Kaksonen, A.H.; Deng, X.; Bohu, T.; Zea, L.; Khaleque, H.N.; Gumulya, Y.; Boxall, N.J.; Morris, C.; Cheng, K.Y. Prospective directions for biohydrometallurgy. *Hydrometallurgy* **2020**, *195*, 105376. [CrossRef]

63. Zhuang, W.Q.; Fitts, J.P.; Ajo-Franklin, C.M.; Maes, S.; Alvarez-Cohen, L.; Hennebel, T. Recovery of critical metals using biometallurgy. *Curr. Opin. Biotechnol.* **2015**, *33*, 327–335. [CrossRef]

64. Vassilev, S.V.; Vassileva, C.G. A new approach for the classification of coal fly ashes based on their origin, composition, properties, and behaviour. *Fuel* **2007**, *86*, 1490–1512. [CrossRef]

65. Asghari, I.; Mousavi, S.; Amiri, F.; Tavassoli, S. Bioleaching of spent refinery catalysts: A review. *J. Ind. Eng. Chem.* **2013**, *19*, 1069–1081. [CrossRef]

66. Srichandan, H.; Mohapatra, R.K.; Parhi, P.K.; Mishra, S. Bioleaching approach for extraction of metal values from secondary solid wastes: A critical review. *Hydrometallurgy* **2019**, *189*, 105122. [CrossRef]

67. Pandey, V.C.; Singh, J.S.; Singh, R.P.; Singh, N.; Yunus, M. Arsenic hazards in coal fly ash and its fate in Indian scenario. *Resour. Conserv. Recycl.* **2011**, *55*, 819–835. [CrossRef]

68. Johnson, D.B.; Roberto, F.F. Evolution and Current Status of Mineral Bioprocessing Technologies. In *Biomining Technologies: Extracting and Recovering Metals from Ores and Wastes*; Springer: Berlin/Heidelberg, Germany, 2022; pp. 1–13.

69. Zhou, H.; Liu, G.; Zhang, L.; Zhou, C. Formation mechanism of arsenic-containing dust in the flue gas cleaning process of flash copper pyrometallurgy: A quantitative identification of arsenic speciation. *Chem. Eng. J.* **2021**, *423*, 130193. [CrossRef]

70. Mossali, E.; Picone, N.; Gentilini, L.; Rodrìguez, O.; Pérez, J.M.; Colledani, M. Lithium-ion batteries towards circular economy: A literature review of opportunities and issues of recycling treatments. *J. Environ. Manag.* **2020**, *264*, 110500. [CrossRef]

71. Mishra, S.; Akcil, A.; Panda, S.; Erust, C. Biodesulphurization of Turkish lignite by Leptospirillum ferriphilum: Effect of ferrous iron, Span-80 and ultrasonication. *Hydrometallurgy* **2018**, *176*, 166–175. [CrossRef]

72. Mishra, S.; Akcil, A.; Panda, S.; Tuncuk, A. Effect of Span-80 and ultrasonication on biodesulphurization of lignite by Rhodococcus erythropolis: Lab to semi-pilot scale tests. *Miner. Eng.* **2018**, *119*, 183–190. [CrossRef]

73. Mishra, S.; Akcil, A.; Panda, S.; Agcasulu, I. Laboratory and semipilot bioreactor feasibility tests for desulphurization of Turkish lignite using Leptospirillum ferriphilum. *Energy Fuels* **2018**, *32*, 2869–2877. [CrossRef]

74. Mishra, S.; Panda, S.; Akcil, A.; Dembele, S.; Agcasulu, I. A Review on Chemical versus Microbial Leaching of Electronic Wastes with Emphasis on Base Metals Dissolution. *Minerals* **2021**, *11*, 1255. [CrossRef]

75. Jain, N.; Sharma, D. Biohydrometallurgy for nonsulfidic minerals—A review. *Geomicrobiol. J.* **2004**, *21*, 135–144. [CrossRef]
76. Singer, A.; Navrot, J.; Shapira, R. Extraction of aluminum from fly-ash by commercial and microbiologically-produced citric acid. *Eur. J. Appl. Microbiol. Biotechnol.* **1982**, *16*, 228–230. [CrossRef]
77. Torma, A.E.; Singh, A.K. Acidolysis of coal fly ash by Aspergillus niger. *Fuel* **1993**, *72*, 1625–1630. [CrossRef]
78. Jadhav, U.U.; Hocheng, H. Analysis of metal bioleaching from thermal power plant fly ash by Aspergillus niger 34770 culture supernatant and reduction of phytotoxicity during the process. *Appl. Biochem. Biotechnol.* **2015**, *175*, 870–881. [CrossRef] [PubMed]
79. Taştan, B.E. Clean up fly ash from coal burning plants by new isolated fungi Fusarium oxysporum and Penicillium glabrum. *J. Environ. Manag.* **2017**, *200*, 46–52. [CrossRef]
80. Seddiek, H.A.; Shetaia, Y.M.; Mahamound, K.F.; El-Aassy, I.E.; Hussien, S.S. Bioleaching of Egyptian Fly Ash Using Cladosporium cladosporioides. *Ann. Biol.* **2021**, *37*, 18–22.
81. Tiwari, S.; Kumari, B.; Singh, S. Microbe-induced changes in metal extractability from fly ash. *Chemosphere* **2008**, *71*, 1284–1294. [CrossRef] [PubMed]
82. Fass, R.; Geva, J.; Shalita, Z.; White, M.; Lezion, R.; Fleming, J. Bioleaching Method for the Extraction of Metals from Coal Fly Ash Using Thiobacillus. US Patent 5,278,069, 1994.
83. Guo, Y.; Teng, Q.; Yang, Z.; Sun, B.; Liu, S. Investigation on bio-desilication process of fly ash based on a self-screened strain of Bacillus amyloliquefaciens and its metabolites. *J. Biotechnol.* **2021**, *341*, 146–154. [CrossRef]
84. Seidel, A.; Zimmels, Y.; Armon, R. Mechanism of bioleaching of coal fly ash by Thiobacillus thiooxidans. *Chem. Eng. J.* **2001**, *83*, 123–130. [CrossRef]
85. Jekić, J.S.; Beškoski, V.P.; Gojgić-Cvijović, G.; Grbavčić, M.; Vrvić, M.M. Bacterially generated Fe2(SO4)3 from pyrite, as a leaching agent for heavy metals from lignite ash. *J. Serbian Chem. Soc.* **2007**, *72*, 615–619. [CrossRef]
86. Kermer, R.; Hedrich, S.; Bellenberg, S.; Brett, B.; Schrader, D.; Schoenherr, P.; Koepcke, M.; Siewert, K.; Guenther, N.; Gehrke, T.; et al. Lignite ash: Waste material or potential resource-Investigation of metal recovery and utilization options. *Hydrometallurgy* **2017**, *168*, 141–152. [CrossRef]
87. Kaur, R.; Goyal, D. Heavy metal accumulation from coal fly ash by cyanobacterial biofertilizers. *Part. Sci. Technol.* **2018**, *36*, 513–516. [CrossRef]
88. Pangayao, D.; Promentilla, M.A.; Gallardo, S.; van Hullebusch, E. Bioleaching kinetics of trace metals from coal ash using *Pseudomonas* spp. In Proceedings of the MATEC Web of Conferences, Makati, Philippines, 21–22 November 2018; EDP Sciences: Les Ulis, France, 2019; Volume 268, p. 01010.
89. Rezaei, H.; Shafaei, S.Z.; Abdollahi, H.; Ghassa, S.; Boroumand, Z.; Nosratabad, A.F. Spent-medium leaching of germanium, vanadium and lithium from coal fly ash with biogenic carboxylic acids and comparison with chemical leaching. *Hydrometallurgy* **2023**, *217*, 106038. [CrossRef]
90. Shabtai, Y.; Mukmenev, I. A combined chemical-biotechnological treatment of coal fly ash (CFA). *J. Biotechnol.* **1996**, *51*, 209–217. [CrossRef]
91. Bankar, A.; Winey, M.; Prakash, D.; Kumar, A.R.; Gosavi, S.; Kapadnis, B.; Zinjarde, S. Bioleaching of fly ash by the tropical marine yeast, Yarrowia lipolytica NCIM 3589. *Appl. Biochem. Biotechnol.* **2012**, *168*, 2205–2217. [CrossRef] [PubMed]
92. Park, S.; Liang, Y. Bioleaching of trace elements and rare earth elements from coal fly ash. *Int. J. Coal Sci. Technol.* **2019**, *6*, 74–83. [CrossRef]
93. Mahmoud, A.; Cézac, P.; Hoadley, A.F.; Contamine, F.; d'Hugues, P. A review of sulfide minerals microbially assisted leaching in stirred tank reactors. *Int. Biodeterior. Biodegrad.* **2017**, *119*, 118–146. [CrossRef]
94. Akcil, A.; Ciftci, H.; Deveci, H. Role and contribution of pure and mixed cultures of mesophiles in bioleaching of a pyritic chalcopyrite concentrate. *Miner. Eng.* **2007**, *20*, 310–318. [CrossRef]
95. Shekhar, S.; Sundaramanickam, A.; Balasubramanian, T. Biosurfactant producing microbes and their potential applications: A review. *Crit. Rev. Environ. Sci. Technol.* **2015**, *45*, 1522–1554. [CrossRef]
96. Eras-Muñoz, E.; Farré, A.; Sánchez, A.; Font, X.; Gea, T. Microbial biosurfactants: A review of recent environmental applications. *Bioengineered* **2022**, *13*, 12365–12391. [CrossRef]
97. Karwowska, E.; Wojtkowska, M.; Andrzejewska, D. The influence of metal speciation in combustion waste on the efficiency of Cu, Pb, Zn, Cd, Ni and Cr bioleaching in a mixed culture of sulfur-oxidizing and biosurfactant-producing bacteria. *J. Hazard. Mater.* **2015**, *299*, 35–41. [CrossRef]
98. Steensels, J.; Gallone, B.; Voordeckers, K.; Verstrepen, K.J. Domestication of industrial microbes. *Curr. Biol.* **2019**, *29*, R381–R393. [CrossRef]
99. Elzeky, M.; Attia, Y. Effect of bacterial adaptation on kinetics and mechanisms of bioleaching ferrous sulfides. *Chem. Eng. J. Biochem. Eng. J.* **1995**, *56*, B115–B124. [CrossRef]
100. Su, H.; Tan, F.; Lin, J. An integrated approach combines hydrothermal chemical and biological treatment to enhance recycle of rare metals from coal fly ash. *Chem. Eng. J.* **2020**, *395*, 124640. [CrossRef]
101. Seidel, A.; Zimmels, Y. Mechanism and kinetics of aluminum and iron leaching from coal fly ash by sulfuric acid. *Chem. Eng. Sci.* **1998**, *53*, 3835–3852. [CrossRef]
102. Sen, S.K.; Das, M.M.; Bandyopadhyay, P.; Dash, R.; Raut, S. Green process using hot spring bacterium to concentrate alumina in coal fly ash. *Ecol. Eng.* **2016**, *88*, 10–19. [CrossRef]
103. Meer, I.; Nazir, R. Removal techniques for heavy metals from fly ash. *J. Mater. Cycles Waste Manag.* **2018**, *20*, 703–722. [CrossRef]

104. Katyal, N.; Sharma, J.; Dhawan, A.; Ali, M.; Mohan, K. Development of rapid method for the estimation of reactive silica in fly ash. *Cem. Concr. Res.* **2008**, *38*, 104–106. [CrossRef]

105. Pangayao, D.; Gallardo, S.; Promentilla, M.A.; Van Hullebusch, E. Bioleaching of trace metals from coal ash using local isolate from coal ash ponds. In Proceedings of the MATEC Web of Conferences, Semarang, Indonesia, 15–16 November 2017; EDP Sciences: Les Ulis, France, 2018; Volume 156, p. 03031.

106. Rompalski, P.; Róg, L. Effect of the temperature of different combustion zones in the boiler grate on changes in physical and chemical parameters of bituminous coal and slags. *J. Sustain. Min.* **2016**, *15*, 73–83. [CrossRef]

107. Wang, H.; Cheng, L.; Pu, J.; Zhao, J. Melting characteristics of coal ash and properties of fly ash to understand the slag formation in the shell gasifier. *ACS Omega* **2021**, *6*, 16066–16075. [CrossRef]

108. Bicer, A. Effect of production temperature on thermal and mechanical properties of polystyrene—Fly ash composites. *Adv. Compos. Lett.* **2020**, *29*, 2633366X20917988. [CrossRef]

109. Yuan, Q.; Zhang, Y.; Wang, T.; Wang, J.; Romero, C.E. Mineralization characteristics of coal fly ash in the transition from non-supercritical CO_2 to supercritical CO_2. *Fuel* **2022**, *318*, 123636. [CrossRef]

110. Iyer, R. The surface chemistry of leaching coal fly ash. *J. Hazard. Mater.* **2002**, *93*, 321–329. [CrossRef] [PubMed]

111. Shoppert, A.; Loginova, I.; Valeev, D. Kinetics study of al extraction from desilicated coal fly ash by NaOH at atmospheric pressure. *Materials* **2021**, *14*, 7700. [CrossRef]

112. Shoppert, A.; Valeev, D.; Loginova, I.; Chaikin, L. Complete extraction of amorphous aluminosilicate from coal fly ash by alkali leaching under atmospheric pressure. *Metals* **2020**, *10*, 1684. [CrossRef]

113. Fan, X.l.; Lv, S.q.; Xia, J.l.; Nie, Z.y.; Zhang, D.r.; Pan, X.; Liu, L.z.; Wen, W.; Zheng, L.; Zhao, Y.d. Extraction of Al and Ce from coal fly ash by biogenic Fe^{3+} and H_2SO_4. *Chem. Eng. J.* **2019**, *370*, 1407–1424. [CrossRef]

114. Muravyov, M.; Bulaev, A.; Melamud, V.; Kondrat'eva, T. Leaching of rare earth elements from coal ashes using acidophilic chemolithotrophic microbial communities. *Microbiology* **2015**, *84*, 194–201. [CrossRef]

115. Zhang, Z.; Allen, L.; Podder, P.; Free, M.L.; Sarswat, P.K. Recovery and enhanced upgrading of rare earth elements from coal-based resources: Bioleaching and precipitation. *Minerals* **2021**, *11*, 484. [CrossRef]

116. Lin, R.; Stuckman, M.; Howard, B.H.; Bank, T.L.; Roth, E.A.; Macala, M.K.; Lopano, C.; Soong, Y.; Granite, E.J. Application of sequential extraction and hydrothermal treatment for characterization and enrichment of rare earth elements from coal fly ash. *Fuel* **2018**, *232*, 124–133. [CrossRef]

117. Deive, F.; Sanromán, M. Bioreactor development for the cultivation of extremophilic microorganisms. In *Current Developments in Biotechnology and Bioengineering*; Elsevier: Amsterdam, The Netherlands, 2017; pp. 403–432.

118. Aphane, M.E.; Doucet, F.J.; Kruger, R.A.; Petrik, L.; van der Merwe, E.M. Preparation of sodium silicate solutions and silica nanoparticles from South African coal fly ash. *Waste Biomass Valorization* **2020**, *11*, 4403–4417. [CrossRef]

119. Yadav, V.K.; Fulekar, M. Green synthesis and characterization of amorphous silica nanoparticles from fly ash. *Mater. Today Proc.* **2019**, *18*, 4351–4359. [CrossRef]

120. Bai, G.; Teng, W.; Wang, X.; Zhang, H.; Xu, P. Processing and kinetics studies on the alumina enrichment of coal fly ash by fractionating silicon dioxide as nano particles. *Fuel Process. Technol.* **2010**, *91*, 175–184. [CrossRef]

121. Khan, S.A.; Uddin, I.; Moeez, S.; Ahmad, A. Fungus-mediated preferential bioleaching of waste material such as fly-ash as a means of producing extracellular, protein capped, fluorescent and water soluble silica nanoparticles. *PLoS ONE* **2014**, *9*, e107597. [CrossRef] [PubMed]

122. Yadav, V.K.; Fulekar, M.H. Advances in methods for recovery of ferrous, alumina, and silica nanoparticles from fly ash waste. *Ceramics* **2020**, *3*, 384–420. [CrossRef]

123. Kolhe, N.; Damle, E.; Pradhan, A.; Zinjarde, S. A comprehensive assessment of Yarrowia lipolytica and its interactions with metals: Current updates and future prospective. *Biotechnol. Adv.* **2022**, *59*, 107967. [CrossRef] [PubMed]

124. Bukhari, S.S.; Behin, J.; Kazemian, H.; Rohani, S. Conversion of coal fly ash to zeolite utilizing microwave and ultrasound energies: A review. *Fuel* **2015**, *140*, 250–266. [CrossRef]

125. Moriwaki, H.; Yamamoto, H. Interactions of microorganisms with rare earth ions and their utilization for separation and environmental technology. *Appl. Microbiol. Biotechnol.* **2013**, *97*, 1–8. [CrossRef]

126. Park, J.; Saratale, G.D.; Cho, S.K.; Bae, S. Synergistic effect of Cu loading on Fe sites of fly ash for enhanced catalytic reduction of nitrophenol. *Sci. Total. Environ.* **2020**, *705*, 134544. [CrossRef]